SIMULATION OF THE ATMOSPHERIC BEHAVIOR FOR THE ENVIRONMENT OF A SMALL-SCALE WIND TURBINE

by

VIET NGUYEN

B.S., Kansas State University, 2002

A THESIS

submitted in partial fulfillment of the requirements for the degree

MASTER OF SCIENCE

Department of Mechanical and Nuclear Engineering
College of Engineering

KANSAS STATE UNIVERSITY
Manhattan, Kansas

2011

Approved by:

Major Professor
Dr. Zhongquan Charlie Zheng

Copyright

Abstract

This study investigates a method using computational fluid dynamics (CFD) to model low-elevation atmospheric conditions. There are three goals in this research: to analyze the wind behavior downwind from buildings and trees, to validate the accuracy of the simulations by comparing wind measurements to the simulation for a specific site, and to find a relationship between the wind speed and the power output of a small-scale wind turbine.

The first goal is to define a proper CFD model for buildings and trees. The trends in the Strouhal number are found to correlate to changes in building height and the wind resistance of a tree as supported in literature, with minor differences with the addition of a tree. The second goal of this study is to model an actual low-elevation environment to compare the energy output predictions for a small-scale wind turbine versus traditional methods. The simulations are compared to on-site wind measurements at a suburban wind turbine, recorded by the rotor and two anemometers installed on the wind turbine tower. The measurements and simulations presented in this study show an improvement in the accuracy in the estimation of the energy output of a wind turbine versus using traditional methods involving high-elevation wind maps. The third goal is to provide a relationship between the wind speed and the power output of a small-scale wind turbine. To accomplish this task, system identification is implemented. The traditional auto-regressive model with exogenous input variables (ARX), its moving average counterpart (ARMAX), and the output error (OE) model are compared in this study. It is found that the transfer function provided by the ARX model most sufficiently estimates the power output of the studied wind turbine, with power output accuracies of 83%. With all three goals addressed, the feasibility of small-scale wind turbines in different low-elevation environments is assessed. In accomplishing these tasks, the siting of a small-scale wind turbine can be optimized qualitatively and quantitatively.

Table of Contents

List of Figures

List of Tables

Acknowledgements

I would like to thank all of the people who made this thesis possible. I thank my advisor, Dr. Zhongquan Charlie Zheng, for his guidance and support throughout my M.S. program.

Also, I would like to thank the members of my committee, Dr. Ruth Douglas Miller and Dr. Bala Natarajan, for their significant contributions.

I also would like to thank the K-State Electrical Power Affiliates for the financial support of this research.

I also thank the research group and the department for their support.

Nomenclature and Abbreviation

A_c	=	sphere cross-sectional area
A_{turb}	=	wind turbine rotor area
ARMAX	=	ARX model with a moving average
ARX	=	auto regression model with exogenous input variables
ASCE	=	American Society of Civil Engineers
C_2	=	inertial resistance factor
C_d	=	drag coefficient
CFD	=	computational fluid dynamics
D_h	=	hydraulic diameter
D_{turb}	=	wind turbine rotor diameter
e(t)	=	white-noise disturbance
F(t)	=	inverse Laplace transfer function
f_{app}	=	highest frequency with applicable spectral data
f_c	=	prominent prevailing frequency
$f_{highest}$	=	highest calculated frequency from FFT
f_{lowest}	=	lowest calculated frequency from FFT
FFT	=	Fast Fourier Transform
g_i	=	gravitational body force
G_k	=	turbulence kinetic energy generation production by mean velocity gradients
h	=	distance between calculation node and wall
H(s)	=	Laplace transfer function
q	=	transfer function root
I	=	turbulence intensity
I(z)	=	power-law profile for the incoming turbulence intensity
I_{ref}	=	reference turbulence intensity at the reference elevation
k	=	turbulent kinetic energy
k-ε	=	k-epsilon turbulence model
$M_{windows}$	=	number of total windows
N	=	number of samples taken
n_a	=	number of dynamic poles
n_b	=	number of zeros
n_c	=	number of poles of the disturbance model
n_f	=	number of poles in the f polynomial of the OE model
n_k	=	number of delays
N_{total}	=	number of total samples taken
N_{window}	=	number of samples taken in a window
NBCC	=	National Building Code of Canada
NRCC	=	National Research Council of

		Canada
OE	=	output error model
P	=	perimeter of sphere
p	=	local air pressure
ppi	=	parts per inch
PISO	=	Pressure-Implicit with Splitting of Operators
PSD	=	Power Spectral Density
R_i	=	inertial resistance of a porous medium
R_v	=	viscous resistance of a porous medium
Re	=	Reynolds number
RNG	=	renormalization-group turbulence model
rpm	=	revolutions per minute
s	=	transfer function pole in a discrete time domain
S_i	=	Darcy-Forchheimer source term
SIMPLE	=	Semi-Implicit Method for Pressure-Linked Equations
St	=	Strouhal number
S_ε	=	deformation tensor scalar
t	=	time
TKE	=	turbulent kinetic energy
U_o	=	mean horizontal wind velocity
u_i	=	velocity of the i-component
u_j	=	velocity of the j-component
$\tilde{U}$	=	mean velocity sensitized to pressure gradients
$\bar{U}$	=	average wind speed
U_i	=	wind speed at a time interval
U_{ref}	=	reference wind speed at the reference elevation
u(t)	=	input signal in system model
U(z)	=	power-law profile for the incoming wind speed
V	=	horizontal wind velocity
V_{turb}	=	wind turbine wind speed
w	=	width of building
x_j	=	distance of the j-component
y*	=	optimal grid cell parameter
y(t)	=	output signal in system model
z	=	height of rectangular domain
z_0	=	surface roughness length
z_{ref}	=	reference elevation
α	=	exponent of the power-law profile for wind speed
α_p	=	permeability of a porous medium
α_k	=	inverse Prandtl number for turbulent kinetic energy
α_ε	=	inverse Prandtl number for turbulence dissipation rate
β	=	exponent of the power-law profile for turbulence intensity
Δt	=	time step interval
δ_{ij}	=	Kronecker delta

ε	=	turbulence dissipation rate (epsilon)
μ_d	=	dynamic viscosity
μ_t	=	turbulent viscosity
ρ	=	air density
τ_ω	=	shear stress

Chapter 1 - Introduction

In the first chapter, I will introduce the research objectives. The techniques, details, and results are presented. I will also outline the organization of the thesis based on the goals.

There are three goals in this research: to analyze the wind behavior downwind from buildings and trees, to validate the accuracy of the simulations by comparing wind measurements to the simulation for a specific site, and to find a relationship between the wind speed and the power output of a small-scale wind turbine. The goals are discussed in the following text.

1.1 Simulating the Flow around Buildings and Trees

The first part of this study investigates a method using computational fluid dynamics (CFD) to model low-elevation atmospheric conditions. The small-scale wind turbine sector is one example of an industry that would benefit from improvements in predicting local-level atmospheric conditions (Elizondo et al., 2009). The placement of small-scale wind turbines is critical in optimizing their performance. Extrapolating high-altitude data lacks validity in estimating local-scale wind because of the exclusion of atmospheric instability due to the obstructions near the ground (Archer and Jacobson, 2003). Turbulence on a local scale is mostly controlled by structures near the ground, such as buildings and tree canopies. A three-dimensional model is generated in this research, consisting of a porous sphere and a square cylinder to mimic a tree and a building. Several turbulence models for the simulation of trees have been evaluated, and the k-epsilon renormalization group turbulence model provides an effective calculation, by validating turbulent kinetic energy and wind-velocity profiles with existing wind tunnel test results on model trees. To assess the conditions of a low-elevation turbulence environment, turbulent kinetic energy and wind-velocity spectra at different points in the flow-field with buildings and trees are analyzed. Local turbulence properties from the simulation results are then analyzed using Fast Fourier Transform (FFT). The CFD models in this research are developed using a commercial fluid flow solver (Fluent User's Guide, 2006). Developing a generalized CFD model that can correlate to different landscapes is important (Heath et al., 2007). A previous CFD model includes an array of house-shaped solid obstructions, but it has a limited computational domain and analyzes only near-wall effects of

wind velocity, neglecting turbulence (Heath et al., 2007). Another CFD study includes aligned, single-standing, porous media, but only investigates drag force characteristics of the porous media, and applies a uniform incoming wind velocity (Wu, 2006). Another study using optical methods to measure tree porosity provides erratic estimations, due to depth-related limits of the method (Grant and Nickling, 1998). This research aims to overcome these problems with the aid from wind tunnel results that are available for model trees of different porous media correlating to a variety of tree crowns (Gromke and Ruck, 2008).

Using the wind tunnel results by Gromke and Ruck (2008) as a basis for setting up trees, simulations are developed to study the effect of buildings and trees on downwind turbulence conditions. The trends in the Strouhal number are found to correlate to changes in building height and the wind resistance of a tree as supported in literature, with minor differences with the addition of a tree. Combining these simulations with wind measurements will provide the information needed by investors to find the best possible location for a wind turbine within a populated area. By studying the downwind characteristics after changing the height of a building or changing the properties of a tree, the downwind turbulence can be interpreted to suggest feasible conditions for the siting of a wind turbine in urban environments.

1.2 Simulating Wind Speeds for an Actual Environment

The second goal of this study is to model an actual low-elevation environment to compare the energy output predictions for a small-scale wind turbine versus traditional methods. The simulations will validate if data at a nearby open location can be used to estimate the wind at an urban site with the use of published wind flow characteristics for different terrains.

Siting a small-scale wind turbine still lies on a rule-of-thumb and data on high-elevation winds (Nordmeyer, 2006, Heath et al., 2007, Manwell et al., 2002) that do not incorporate terrain characteristics. A wind turbine usually should not be located within a hemispherical region with dimensions of two building heights above, and twenty building heights downwind from a set of buildings or trees (Nordmeyer, 2006). Following this rule-of-thumb may lead to problems, such as availability of space in an urban site, as well as cable length limitations (Manwell et al., 2002).

Recent research has gone into predicting the turbulence downwind from a building, primarily in the flow of three-dimensional rectangular cylinders. These groups have shown that the frequency of vortices downwind from a building could be analyzed to predict the feasibility

of siting a wind turbine in the wake of a building at a certain distance (Huang et al., 2010, Yoon et al., 2010).

Since using high-elevation wind data is too general for specific sites, there can be a considerable difference between estimated and actual power outputs from two wind turbines located in the same city. A method in estimating the power output of a proposed site involves the average annual wind speed read from a high-elevation wind map (Elmore and Gallagher, 2009, Schuster, 2009), then interpreting the corresponding annual power production from a power curve. The Warwick Wind Trials conducted in Warwick, England, showed that two wind turbines in the city were estimated to have an equivalent amount of energy output of 127 to 129 kWh, based on the National Objective of Boundary Layer wind map (Hailes, 2009). However, the measured wind speeds at one wind turbine position in an open yard had a corrected energy output estimate of 166 kWh, two times larger than the other wind turbine located among residential buildings, calculated to only 88 kWh (Hailes, 2009). This case exemplifies the inaccuracy of using high-elevation wind data to estimate energy outputs for small-scale wind turbines.

An improvement to the energy output estimation can be achieved by incorporating the specific terrain of a wind turbine into a numerical simulation, without paying the high costs associated with measuring wind at every proposed site. A number of studies have been conducted to improve the understanding of low-elevation wind behavior at various surface terrains, ranging from open fields to urban environments (Kozmar, 2008, Tamura et al., 2007). An accurate estimation can be performed by averaging the wind speed from a local weather station or airport, then using vertical, power-law profiles for wind speed and turbulence intensity for the terrain of the proposed site to simulate the atmospheric behavior. The profiles for wind speed have been proposed by different research groups, including Counihan (1975) and Spera (2009). The profiles for turbulence intensity are supplied by various organizations, including the American Society of Civil Engineers (ASCE) and the National Research Council of Canada (NRCC), and are summarized by Bashor and Kareem (2009), and Zhou and Kareem (2002). Past research has specified that low-elevation turbulence is significant in the energy production of a wind turbine. Neglecting turbulence in the wind can result in a deviation of over nine percent in the annual energy output (Sheinman and Rosen, 1992). Incorporating terrain characteristics in a

computational simulation will provide information necessary in siting a wind turbine without taking excessive and costly wind measurements.

Simulations of a wind turbine site in Manhattan, KS, are generated and compared to wind measurements, recorded by the wind turbine rotor and two anemometers installed on the tower. The wind speed and direction are measured at three elevations on a meteorological tower located in an open terrain outside of the city. The anemometer readings from the meteorological tower are used to calculate the power-law profiles for wind speed and turbulence intensity for the simulations. The key settings to simulate the low-elevation atmosphere of a site are also presented. These include the incoming power-law profiles for wind speed and turbulence intensity, the boundary conditions, and the grid resolution.

The use of CFD avoids the excessive costs and uncertainty in predicting the potential and actual energy at a location. The savings in cost and time, as well as the reduction in uncertainty of estimation accuracies, will not only benefit commercial investors, but also customers in under-developed countries in which a single wind turbine may provide enough electricity for a single day's use. These reasons support the usefulness of accurate CFD modeling of low-elevation atmospheric conditions towards improving the estimation of attainable energy at a potential small-scale wind turbine site.

1.3 Predicting Power Production using System Identification

The third goal is to provide a relationship between the wind speed and the power output of a small-scale wind turbine. Providing this relationship will allow the use of an anemometer to accurately estimate the attainable power output of a proposed site, incorporating the mechanical response of the wind turbine itself. This will provide crucial cost and time savings in siting a small-scale wind turbine.

To accomplish this task, system identification is implemented. A transfer function is first implemented to correlate the wind speed measured by an anemometer to the rotational speed of a wind turbine. The modeled rotational speed is then used to calculate the power output. Finally, the modeled power output is compared to the measured power output. To model the system, the anemometer wind speed is selected as the input signal and the wind turbine rotational speed is selected as the output signal. Three random days with a quasi-steady state wind speed and power output response from the wind turbine are chosen.

Since the mechanics in the wind turbine are assumed to be complex, parametric identification is used to define the model of the system (Erdogan and Gulal, 2009). Identifying a suitable system is conducted by comparing three different models. The traditional auto regression model with exogenous input variables (ARX), its moving average counterpart (ARMAX), and the output error (OE) model are compared in this study. The model characteristics rely on the preference of the designer in balancing accuracy and algorithmic complexity (Barbounis and Theocharis, 2007). The advantage of using auto regression models is that they can be generated quickly, given a known input and output of the system (Ljung, 1999).

Previous research on wind farm wind speeds found that auto regression models with up to three poles were sufficient in estimating the power output based on the minimized error between the actual and modeled power output (Kanellos et al., 2011). This study finds that the transfer function provided by a low-order ARX model sufficiently estimates the power output of the studied wind turbine. This is validated using parametric modeling, where the measured and modeled power outputs are compared.

Depending on the application related to the wind turbine, even a marginal improvement in predicting the power output on a day-to-day basis may be vital. The results presented in this study present an improvement in predicting wind turbine power production using anemometer wind speeds to estimate the power output of a wind turbine.

With all three goals addressed, the feasibility of small-scale wind turbines in different low-elevation environments is assessed. Studying the turbulence characteristics of the wind flow downwind from buildings and trees aids in optimizing the siting of a small-scale wind turbine in an urban environment. Accurately simulating a low-elevation environment to assess the attainable power output of a wind turbine will save costs and time, as well as improve the estimates versus using a wind map. To further improve wind turbine siting, the relationship between wind speeds measured by an anemometer and the power output of a wind turbine is found using system identification. In accomplishing these tasks, the siting of a small-scale wind turbine can be optimized qualitatively and quantitatively.

Chapter 2 - Computational Simulation of Local Atmospheric Turbulence for Flow past Buildings and Trees

2.1 Computational Scheme Validation with Flow around a Solid Sphere

In the second chapter, I will introduce the approach in numerically simulating buildings and trees in a turbulent environment. The CFD criteria are established, and the trends in different building heights and in different wind resistances of trees are discussed.

2.1.1 Geometry of the Solid Sphere Model

A solid sphere is modeled first to validate the accuracy of the chosen software based on the conditions of this research. The computational domain of the solid sphere model is an origin-centered rectangular volume with (x, y, z) dimensions of (±0.09 m, ±0.12 m, ±0.09 m), where y and z are the lengthwise and vertical-components, respectively, with a centered, 0.06 m diameter, solid sphere.

The grid size and shape are critical elements in the accuracy of the post-processing results. Tetrahedral volumes with edge spacing lengths of 0.006 m (one-tenth of the sphere diameter) are chosen. A grid sensitivity study based on values estimated around the y* cell length parameter around the sphere is accomplished by testing grid spacing lengths of 0.010 m, 0.008 m, 0.006 m, 0.004 m, and 0.003 m (Fluent User's Guide, 2006). Each of the grid spacing lengths show negligible differences in the resulting drag coefficient, wind velocity, and turbulent kinetic energy contours, specifically for the solid and porous sphere test simulations that will be presented in the upcoming sections. The 0.006 m grid spacing length is chosen to avoid computer memory restrictions and excessive processing time of the finer grid spacing lengths tested. The grid is refined around the sphere to double the amount of cells. This refinement is generated within one diameter, or 0.06 m, from the surface of the sphere. The entire rectangular domain is also refined with volume changes of 2.5 to prevent sudden jumps in grid volume between the mesh boundaries which could impair the flow calculations. Based on the chosen grid length, sphere diameter, and grid refinement, it is recommended that at least twenty grid cells along the diameter of the sphere are generated to resolve the flow accurately.

2.1.2 Computational Setup of the Solid Sphere Model

After the generation of the grid, a set of incompressible flow equations (Reynolds-averaged Navier-Stokes equations) with turbulence models are then solved (Fluent User's Guide, 2006). The first equation is the mass conservation, or continuity, equation modeled by Eq. (2.1), where u_j is the velocity of the j-component, and x_j is the distance. The second equation is the momentum conservation, or Reynolds-Averaged Navier-Stokes equation, modeled by Eq. (2.2),

$$\frac{\partial u_j}{\partial x_j} = 0 \tag{2.1}$$

$$\rho \frac{\partial u_i}{\partial t} + \rho u_j \frac{\partial u_i}{\partial x_j} = -\frac{\partial p}{\partial x_i} + \mu_d \frac{\partial^2 u_i}{\partial x_j \partial x_j} - \rho \frac{\partial}{\partial x_j}(\overline{u_i' u_j'}) + \rho g_i \tag{2.2}$$

where t is the time, ρ is the air density, p is the local pressure, μ_d is the dynamic viscosity for air, and g_i is the gravitational body force. The turbulence stresses are calculated from the mean deformation rate using Eq. (2.3),

$$\overline{u_i' u_j'} = -\frac{\mu_t}{\rho}\left(\frac{\partial u_i}{\partial x_j} + \frac{\partial u_j}{\partial x_i}\right) + \frac{2}{3} k \delta_{ij} \tag{2.3}$$

where the Reynolds stress tensor is the left-hand side of Eq. (2.3), μ_t is the turbulent viscosity for air, k is the turbulence kinetic energy, and δ_{ij} is the Kronecker delta, where $\delta_{ij}=0$ for $i \neq j$ and $\delta_{ij}=1$ for $i=j$.

The first-order in time and space, steady implicit solver is used in the solid sphere simulation. The turbulence model is set as the k-epsilon (k-ε), renormalization-group (RNG), non-equilibrium near-wall treatment model. This model is selected based on recommendations in literature, in which the k-ε model is well-suited for high Reynolds number (Re), fully turbulent flows (Launder and Spaulding, 1972, Versteeg and Malalasekera, 1995). The RNG option is selected to improve the vorticity and epsilon parameter calculations (Yakhot and Orszag, 1986). The k-ε, RNG turbulence kinetic energy (k) and turbulence dissipation rate (or epsilon, ε) throughout the flow-field are solved using Eqs. (2.4), (2.5), and (2.6),

$$\rho \frac{\partial k}{\partial t} + \rho u_i \frac{\partial k}{\partial x_i} = \frac{\partial}{\partial x_j}\left(\alpha_k \mu_t \frac{\partial k}{\partial x_j}\right) + G_k - \rho \varepsilon \tag{2.4}$$

$$\rho\frac{\partial\varepsilon}{\partial t}+\rho u_i\frac{\partial\varepsilon}{\partial x_i}=\frac{\partial}{\partial x_j}\left(\alpha_\varepsilon\mu_t\frac{\partial\varepsilon}{\partial x_j}\right)+1.42G_k\frac{\varepsilon}{k}-\left[1.68+\frac{0.0845\rho\eta^3\left(1-\frac{\eta}{4.38}\right)}{1+0.012\eta^3}\right]\frac{\varepsilon^2}{k} \tag{2.5}$$

$$\eta=\frac{S_\varepsilon k}{\varepsilon} \tag{2.6}$$

where α_k and α_ε are the inverse Prandtl numbers for k and ε, respectively, G_k is the turbulence kinetic energy generation production by mean velocity gradients, and S_ε is the deformation tensor scalar (Santiago and Martin, 2005, Chan et al., 2002). The non-equilibrium near-wall treatment is selected to improve the boundary calculations for the pressure gradient effects, since the solid sphere model consists of a three-dimensional flow with vortices (Kim and Choudhury, 1995). This option specifically improves the drag coefficient calculations for the solid sphere model. The non-equilibrium near-wall treatment option adds a mean-velocity log-law that is sensitized to pressure gradients which is modeled by Eq. (2.7),

$$\rho\tilde{U}\frac{0.0845^{0.25}k^{0.5}}{\tau_\omega}=\frac{1}{0.4187}\ln\left(9.793\rho\frac{0.0845^{0.25}k^{0.5}h}{\mu_d}\right) \tag{2.7}$$

where $\tilde{U}$ is the mean velocity sensitized to pressure gradients, τ_ω is the shear stress, and h is the distance from the wall (Kim and Choudhury, 1995). The material is air with a density (ρ) of 1.225 kg·m^{-3} and a dynamic viscosity (μ_d) of $1.789\cdot10^{-5}$ kg·m^{-1}·s^{-1}.

The accuracy of the solid model is investigated over a range of incoming wind velocity conditions. The inlet boundary condition is set as a velocity inlet and the outlet is set as an outflow boundary condition. Three separate simulations are generated for three different uniform horizontal-velocities at the inlet of 4.9 m·s^{-1}, 9.7 m·s^{-1}, and 14.6 m·s^{-1}. These wind velocities correspond to Re values of 20,131, 39,852, and 59,983, respectively, to cover the range of the drag coefficient curve from literature (Schlichting, 2000). The time-dependent horizontal-velocities are calculated using Eq. (2.8) for Re and the hydraulic diameter (D_h) of the sphere in meters is calculated using Eq. (2.9),

$$\mathrm{Re}=\frac{\rho V D_h}{\mu_d} \tag{2.8}$$

$$D_h=\frac{4A_c}{P} \tag{2.9}$$

where the density and dynamic viscosity of air are used, the sphere cross-sectional area, A_c, is 0.182 m^2, the sphere perimeter (P) is the circumference of $0.06 \cdot \pi$ m, and V is the horizontal-velocity.

A value of 10% is assigned to the turbulence intensity, I(z), to model a fully-developed turbulent flow (Pope, 2000). The solid sphere wall is set as hydrodynamically-smooth to compare the solid sphere wall drag coefficient calculations to the drag coefficient curve established by Schlichting (2000). A hydrodynamically-smooth wall is established by setting the roughness height coefficient to zero which also sets the additive constant in the log-law for a hydrodynamically-smooth wall to zero (Cebeci and Bradshaw, 1977).

The accuracy and data monitoring settings are applied next. For the convergence accuracy of the residuals, continuity and turbulence dissipation rate are both set to $1 \cdot 10^{-3}$ and the velocities are set to $1 \cdot 10^{-5}$. The continuity and velocity residuals are adjusted from the default value of 0.001 for each parameter in order to improve the accuracy of the drag coefficient calculations, based on iterative simulations (Fluent User's Guide, 2006). The solution relaxation controls are set as a momentum relaxation factor value of 0.4, a turbulence kinetic energy of 0.1, a turbulence dissipation rate of 0.1, and a turbulent viscosity of 0.6, each based on default industry use and iterative simulations (Fluent User's Guide, 2006). The SIMPLE (Semi-Implicit Method for Pressure-Linked Equations) method is chosen over the PISO (Pressure-Implicit with Splitting of Operators) method is chosen over the PISO (Pressure-Implicit with Splitting of Operators) method because of the unnecessary re-iterations based on the velocity calculations, since the velocity calculations are usually of a high degree of accuracy to the fifth decimal (Patankar, 1980). Initialization settings match the previous settings, in which the horizontal-velocity is the same as the input uniform horizontal-velocity, and the turbulent kinetic energy is the same value as set in the solution relaxation controls. Monitoring is applied under the force option, to read the drag coefficient calculations on the solid sphere wall face in the y-direction. The final pre-processing settings are the reference values for the sphere-body cross-sectional area, A_c, and velocity under the report menu. A_c is $0.032 \cdot \pi$ m^2, and each of the velocity inputs are set as the corresponding initialization values for the three separate simulations.

2.1.3 Results of the Solid Sphere Model

The results of the solid sphere model confirm that the computational model is sufficiently accurate. From literature, the drag coefficients are approximately 0.43, 0.47, and 0.44, for Re values of 20,000, 40,000, and 60,000, respectively (Schlichting, 2000). The drag coefficients for these three cases agree very well with the drag coefficient curve generated by Schlichting, with an average of 3% error. The simulation results also compare well with the Gromke and Ruck (2008) measurement data, within 4% error. The drag coefficient results are shown in Fig. 2.1.

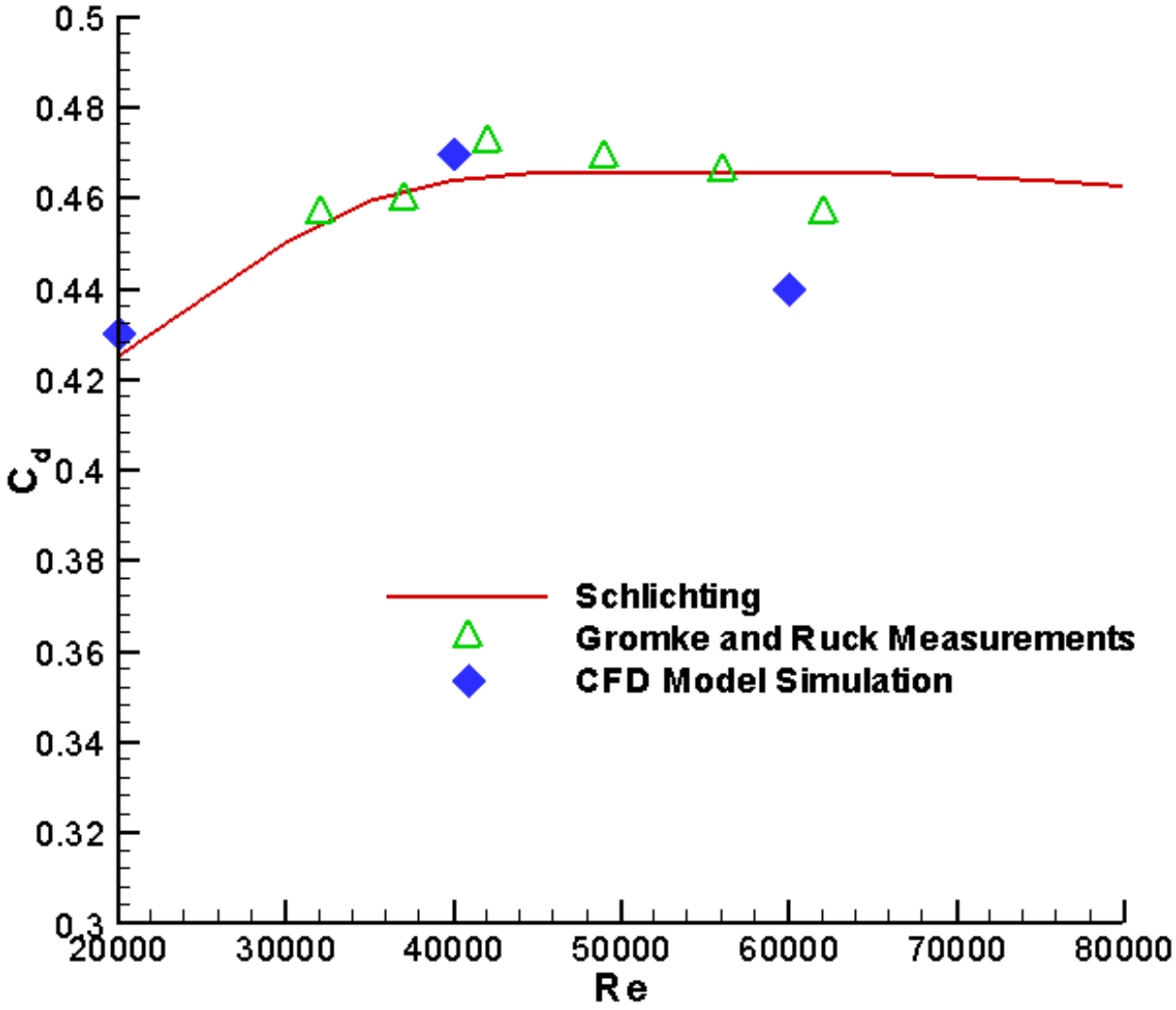

Figure 2.1 CFD simulation results compared to literature data

The horizontal-velocity, vertical-velocity, and turbulent kinetic energy contours shown in Figs. 2.2(a), 2.2(b), and 2.2(c), respectively, present similar flow profiles and magnitudes as a

model tree equivalent to the solid sphere made from an impermeable Styrofoam used by Gromke and Ruck (2008).

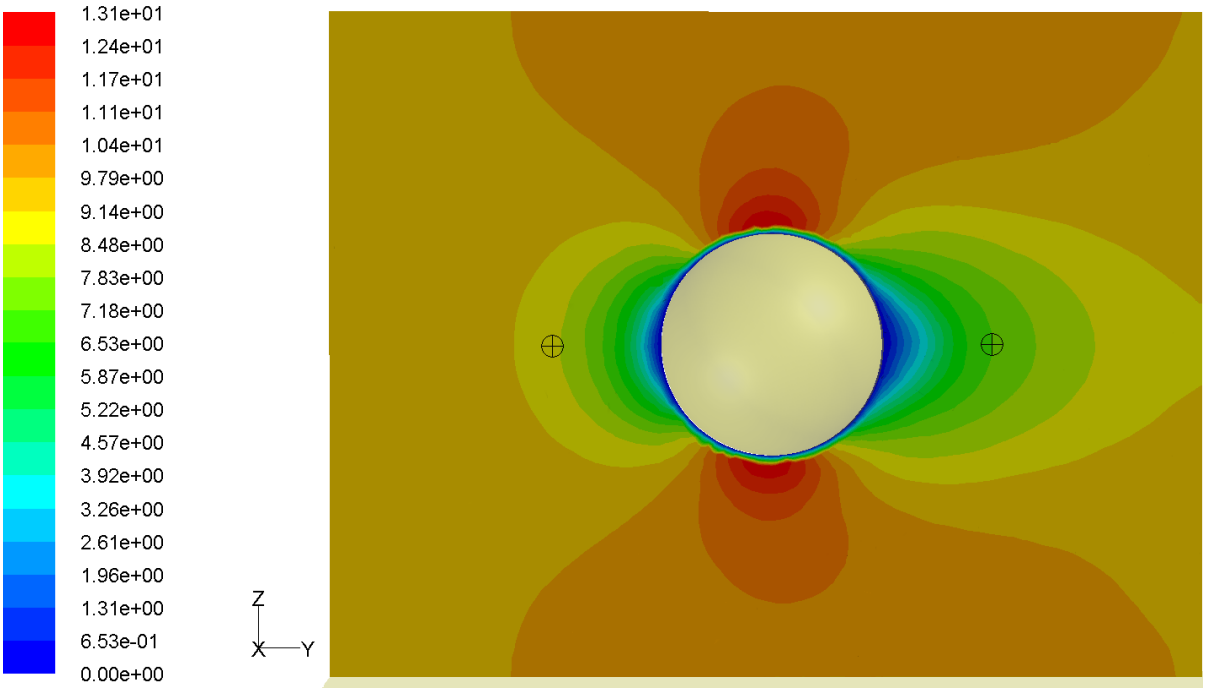

(a) Horizontal-velocity contour plot

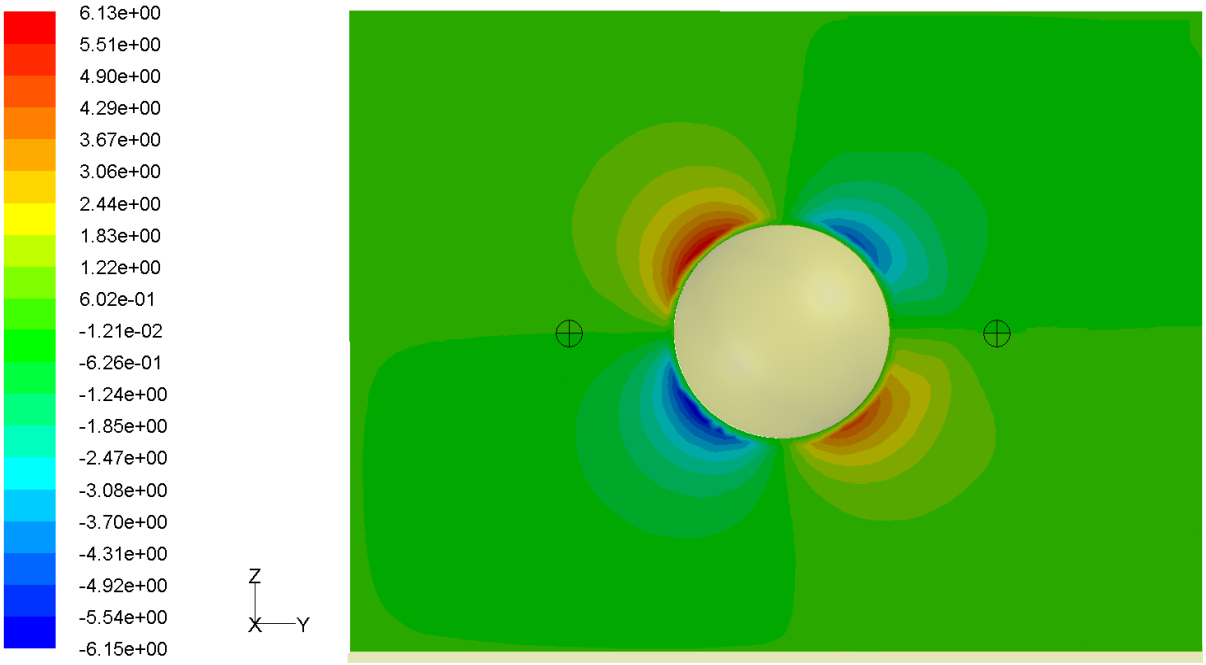

(b) Vertical-velocity contour plot

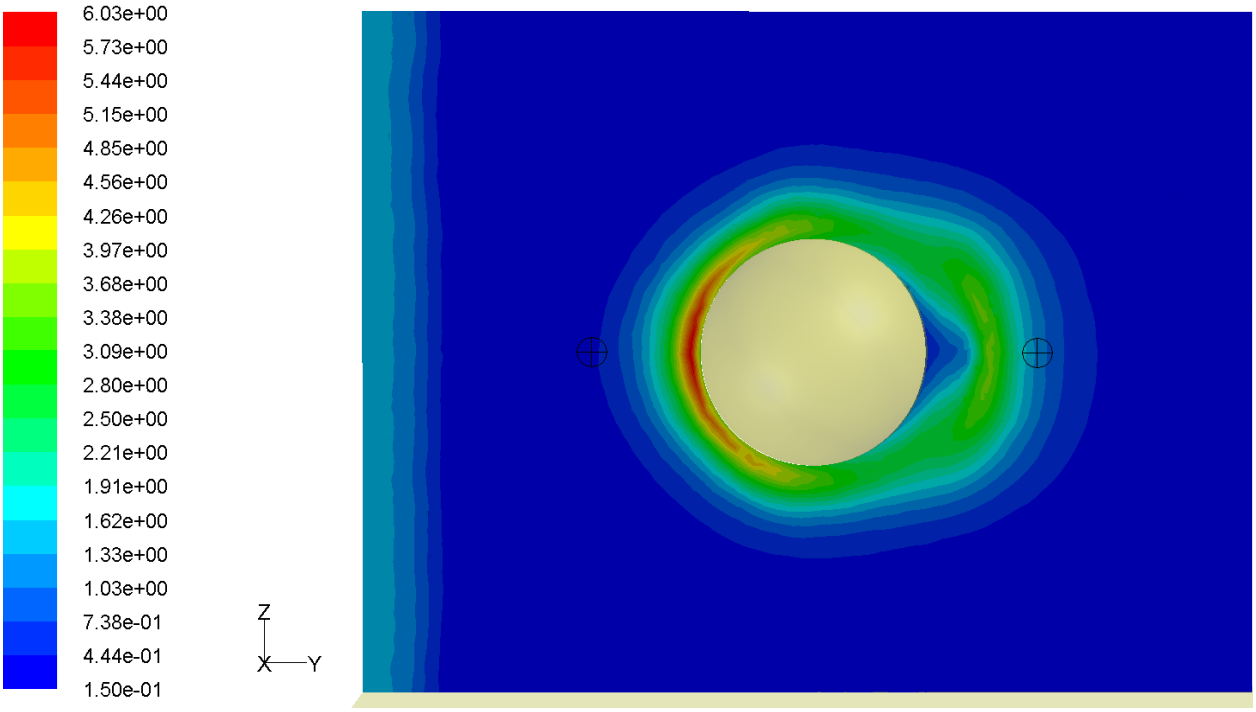

(c) Turbulent kinetic energy contour plot

Figure 2.2 Solid sphere contour plots with Re=40,000

The solid sphere simulation results are quantified by comparing three points listed in Table 2.1.

Table 2.1 Solid sphere CFD model compared to wind tunnel results

Point-by-Point Comparison Between the CFD Model and the Gromke and Ruck Contours along a Centerline Plane Going Through the Solid Sphere Model						
(x, y, z) m Coordinates of CFD Model	Horizontal-Velocity ($m \cdot s^{-1}$)		Vertical-Velocity ($m \cdot s^{-1}$)		Turbulent Kinetic Energy ($m^2 \cdot s^{-2}$)	
	CFD	Gromke and Ruck	CFD	Gromke and Ruck	CFD	Gromke and Ruck
(0.12, 0.06, 0.07)	8.51	7.29	-0.17	-0.25	0.48	3.65
(0.12, 0.06, 0.07)	7.12	2.70	-0.06	0.09	1.47	10.33

The negligible discrepancies between the CFD solid sphere model and the wind tunnel results of the solid Styrofoam model are due to the CFD model not including a wall boundary on the bottom face, as well as a cylinder to mimic a tree trunk. The CFD model utilizes a uniform incoming wind velocity, while the wind tunnel tests include the bottom wall as a boundary, use a model tree with a trunk, and most importantly, employ power-law profiles for the incoming wind parameters (Gromke and Ruck, 2008). However, the general agreements in the drag coefficients, the velocity magnitudes, and the shape of the contours in Fig. 2.2 provide sufficient evidence for the accuracy of the CFD model and the settings to be further used for simulating flow around porous spheres and around more complicated, combined building-tree simulations.

2.2 Validation with Wind Tunnel Data for Flow around a Single-Standing Porous Sphere

2.2.1 Geometry of the Porous Sphere Model

The next step towards developing a full-scale CFD application is validating CFD results for a porous sphere model to wind tunnel data. The porous sphere model adopts similar settings as the solid sphere model, except for a few modifications.

The computational domain of the porous sphere model is a rectangular volume in the first quadrant, i.e., $0 \leq x \leq 0.24$ m, $0 \leq y \leq 0.42$ m, and $0 \leq z \leq 0.18$ m. To model a simple spherical tree that is similar to the wind tunnel models, a 0.06 m-diameter sphere is centered at the (x, y, z) coordinates of (0.12 m, 0.18 m, 0.07 m) (Gromke and Ruck, 2008). The tree trunk is a 0.04 m-high cylinder with a diameter of 0.02 m and has a contour to match the sphere face beyond the 0.04 m tree trunk height (Gromke and Ruck, 2008). The porous sphere is created by changing the spherical face from a solid wall to an interface and setting the spherical volume as a separate flow region.

2.2.2 Additional Equations of the Porous Sphere Model

The differences between the solid sphere model and the porous sphere model are the sphere wall interface and sphere volume changes, an added ground wall, and the incoming wind velocity and turbulence intensity profiles. The inlet wind velocity and inlet turbulence intensity profiles are modeled using user-defined functions incorporated into the flow solver, as power-law profiles specified in the wind tunnel tests by Gromke and Ruck (2008). These profiles are

imperative in validating the measurements from the porous media wind tunnel tests. The profiles of the incoming power-law profile wind velocity, U(z), and turbulence intensity, I(z), are modeled using Eqs. (2.10) and (2.11), respectively,

$$U(z) = 9.0\left(\frac{z}{0.1}\right)^{0.22} \quad m \cdot s^{-1} \tag{2.10}$$

$$I(z) = 18.3\left(\frac{z}{0.1}\right)^{-0.19} \quad m \cdot s^{-1} \tag{2.11}$$

where z is the height of the rectangular domain (Gromke and Ruck, 2008).

The inlet turbulence intensity profile is used to provide the incoming source for the turbulent kinetic energy and turbulence dissipation rate calculations in the flow field, which are set directly in the flow solver as the inlet profile conditions. The equations for the turbulent kinetic energy and the turbulence dissipation rate at the inlet are modeled using Eqs. (2.12) and (2.13), respectively,

$$k = 1.5\left[I(z) \cdot U(z)\right]^2 \quad m^2 \cdot s^{-2} \tag{2.12}$$

$$\varepsilon = 0.09^{0.75}\left(\frac{k^{1.5}}{0.07 D_h}\right) \tag{2.13}$$

where D_h is the sphere diameter (Pope, 2000).

The porous sphere volume, or substrate, is set as a laminar porous zone to calculate the internal substrate flow without turbulence, since the flow speed is substantially reduced inside the porous medium in the cases studied here. The porous zone parameters are set with the primary direction of y=1 and secondary directions of x=1 and z=1. The viscous resistance (R_v) and the form drag, or inertial resistance (R_i), values of the porous medium are set based on evaluating the added Darcy-Forchheimer source term (S_i) in the i-direction for the turbulent kinetic energy and momentum equations (Da Silva et al., 2006, Katul et al., 2004, Sanz, 2003). The source term is modeled using Eq. (2.14),

$$S_i = -u_i\left(\frac{\mu_d}{\alpha}\right) - \frac{1}{2} C_2 \rho |u| u_i \tag{2.14}$$

where α is the permeability of the porous medium, and C_2 is the inertial resistance factor (Sanz, 2003). The first grouped term on the right-hand side of Eq. (2.14) is the viscous resistance term, and the second grouped term is the inertial resistance. The viscous resistance is set to zero

because it is negligible as compared to the inertial resistance due to the leaf fluttering properties of an actual tree (Laadhari et al., 1994). The inertial resistance term is set to 250 m^{-1} in the x, y, and z directions in the flow solver (Gromke and Ruck, 2008).

The porous sphere solution process is solved similarly as the previous solid sphere CFD model, using the first-order implicit flow solver with the RNG, k-ε turbulence model, and non-equilibrium near-wall treatment for the same reasons. However, to study time-dependent effects in the flow field, the flow solver is set to unsteady state.

The residual accuracy is 10^{-3} for continuity, k, and ε, and 10^{-5} for the velocities in each direction. These values are chosen after iteratively simulating the porous model case and based on typical settings used in industry (Fluent User's Guide, 2006). The same solution and initialization settings are used for the porous sphere validation model as before in the solid sphere model, with the exception that the horizontal velocity is set to 8.4 $m \cdot s^{-1}$ to correspond to the power-law inlet velocity calculation at the maximum height of the sphere crown where z=0.10 m.

2.2.3 Results of the Porous Sphere Model

An analysis of the time-history of the turbulent kinetic energy and the horizontal-velocity is performed at the upwind and downwind points. After a simulation time of 30 s, each of the time-history signals approach asymptotic values. The steady-state responses are expected, since an inflicted velocity profile in a mixing layer for a single tree does not appear as it does for an array of trees (Gromke and Ruck, 2008). The lack of a common characteristic energy shift in the supplied frequency range for various single-standing model trees, such as for sisal fiber and wood wool model trees, is also observed in the wind tunnel tests (Gromke and Ruck, 2008).

The time-history data is recorded at two points in the flow field for the turbulent kinetic energy and the horizontal velocity. One point is at the (x, y, z) coordinates of (0.12 m, 0.03 m, 0.07 m), and is labeled as the "upwind point." Another point is created at (0.12 m, 0.258 m, 0.07 m), and is labeled as the "downwind point." The upwind point is arbitrarily placed 0.03 m from the inlet, far enough in front of the sphere to avoid influence from the sphere. The downwind point is at a distance of 2.3 times the diameter of the sphere behind the sphere center to match the point location used in the spectral analysis by Gromke and Ruck (2008). A time step of 0.001 s is

used to correspond to the sampling frequency of 500 Hz used by Gromke and Ruck for the spectral analysis of the wind tunnel downwind point.

Contours of the horizontal-velocity, vertical-velocity, and turbulent kinetic energy are taken at an instantaneous time of 184 s, as shown in Figs. 2.3(a), 2.3(b), and 2.3(c), respectively, to compare to the instantaneous snapshots of the contours provided by existing wind tunnel testing (Gromke and Ruck, 2008). Post-processing the results for the porous sphere model finds that the horizontal-velocity and vertical-velocity contours compare very well with those of the wind tunnel tests, showing a similar separated circulatory flow field behind the porous sphere as displayed by that of the 10 ppi Styrofoam test sphere (Gromke and Ruck, 2008). The turbulent kinetic energy contour shown in Fig. 2.3(c) also matches the wind tunnel turbulent kinetic energy contour.

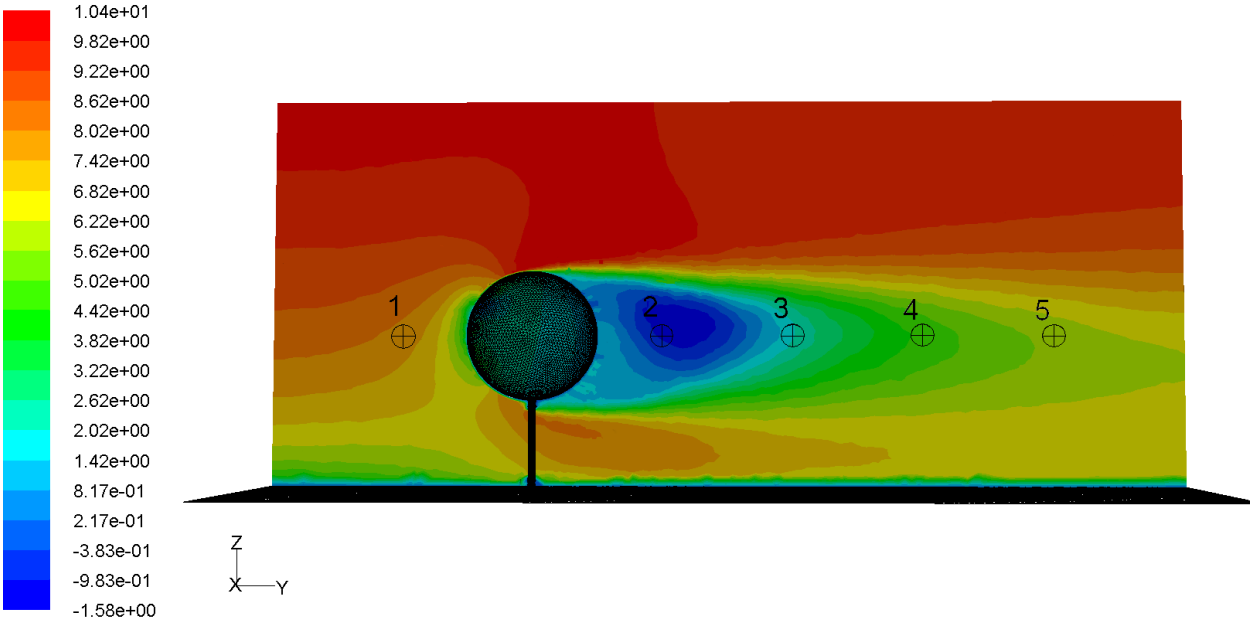

(a) Horizontal-velocity contour plot

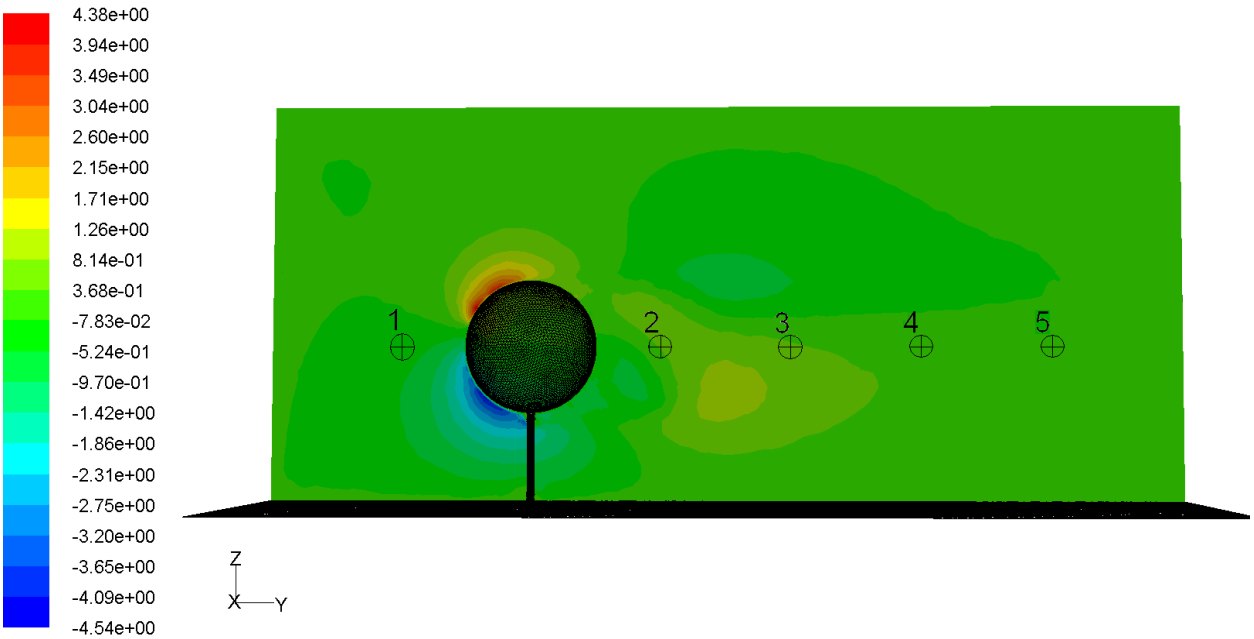

(b) Vertical-velocity contour plot

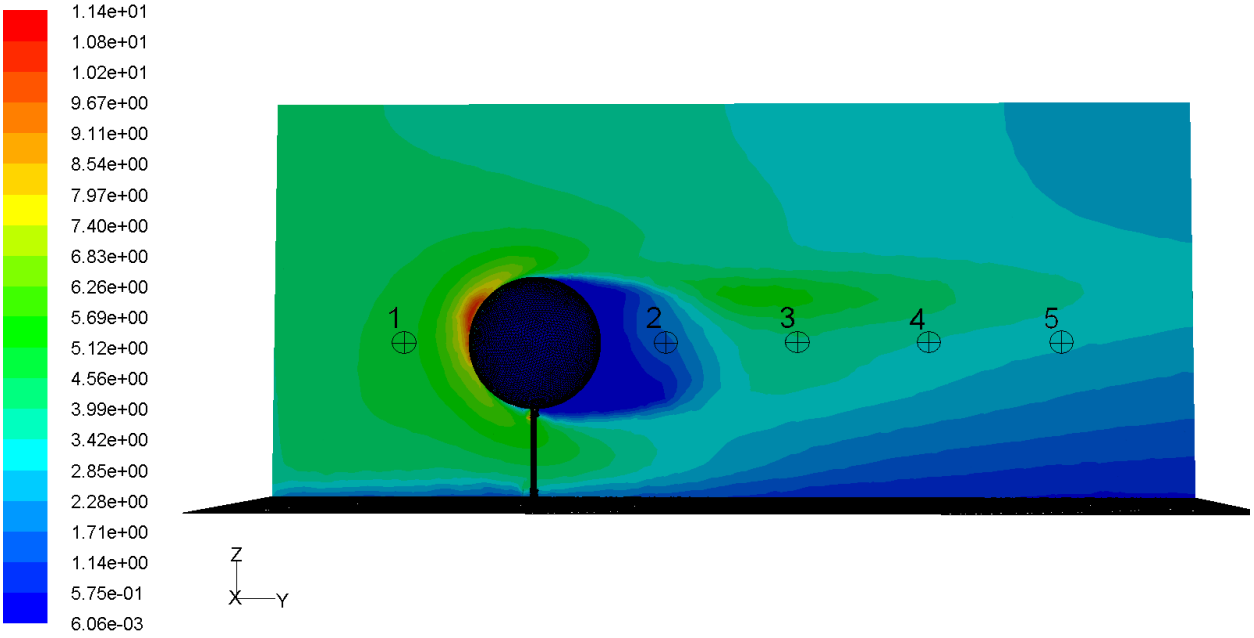

(c) Turbulent kinetic energy contour plot

Figure 2.3 Porous sphere contour plots taken at the instantaneous time of 184 s

To further quantify the comparison, data sets in the five locations indicated in the contour plots are compared in Table 2.2. The CFD simulation values compare reasonably well with the wind

tunnel results, where the values can be further improved by taking values at a later time in the unsteady-state flow to reduce the discrepancies between the data.

Table 2.2 Porous sphere model compared to wind tunnel results

Point-by-Point Comparison Between the CFD Model and the Gromke and Ruck Contours along a Centerline Plane Going Through the Porous Sphere Model at 184 s							
Data Point in the Porous Sphere Model	y-Coordinate of Data Point (m)	Horizontal-Velocity ($m \cdot s^{-1}$)		Vertical-Velocity ($m \cdot s^{-1}$)		Turbulent Kinetic Energy ($m^2 \cdot s^{-2}$)	
		CFD	Gromke and Ruck	CFD	Gromke and Ruck	CFD	Gromke and Ruck
1	0.09	8.21	6.84	-0.13	-0.18	4.47	4.25
2	0.24	-1.09	-1.35	0.39	0.22	1.57	4.86
3	0.28	1.94	2.43	0.43	0.35	3.88	6.48
4	0.32	4.58	4.86	0.17	0.11	3.38	5.27
5	0.36	5.81	6.03	0.10	-0.14	2.95	4.46

2.3 Spectral Analysis for Wind in an Environment with Buildings and Trees

2.3.1 A Building-Tree Model: Flow over a Square Cylinder and a Porous Sphere

The next step of this research is to examine the flow around a combined building-tree structure, modeled by a solid square cylinder and a porous sphere. A rectangular domain with (x, y, z) dimensions of (26 m, 62 m, 28 m) is used, with the building-base centered at the coordinates, (13 m, 12 m, 0). The building is placed upwind of the tree, so that the porous medium effects on the turbulent flow behavior downwind from the building can be studied. The building has hydrodynamically-smooth walls and an 8 m x 8 m base. The 11 m tall tree has a 6 m diameter spherical crown, with a 5 m tall cylinder as a tree trunk, and its vertical center is placed 16 m behind the rear wall of the square cylinder, with the central base at (x, y, z) coordinates of (13 m, 32 m, 0).

Different cases are simulated to compare their flow field characteristics, including changing the height of the building, moving the tree further downwind, and changing the inertial resistance of the tree. In addition to these comparisons, a tree with an extremely low R_i is compared to a case without a tree and a tree with an extremely high R_i is compared to a case with a solid tree to reinforce the validity of changing R_i to describe the resistance of a tree against wind flow.

To compare the cases using Fast Fourier Transform (FFT), the horizontal velocity and turbulent kinetic energy at two locations are tracked in each case. An "inner point" is between the building and tree, 10 m upwind from the center of the spherical tree crown (y=22 m). A "downwind point" is located a distance of 2.3 times the diameter of the sphere downwind from the center of the tree crown to stay consistent with the distance analyzed by Gromke and Ruck (y=45.8 m) (Gromke and Ruck, 2008). Both points are at 13 m in the lateral x-direction and 8 m in the vertical z-direction. The two points are shown in each of the following contour plots.

2.3.2 The Spectral Analysis Method used for Turbulence in the Building-Tree Simulation Model

To find how often a recirculation zone formulates in the flow field, spectral analyses are applied to quasi-steady state time-history data. Time step intervals are set to $\Delta t=0.0009$ s to sufficiently capture the flow recirculation frequency and corresponding Strouhal number (St) for each case. Videos are created and inspected to visualize the time intervals between recirculation zones in the flow fields to confirm the prominent prevailing frequencies calculated by the Fast Fourier Transform (FFT) processing.

A recirculation zone forms at different times at the inner and downwind points. This flow behavior matches the two-dimensional square cylinder experimental results by Sakamoto and Arie (1983) where recirculation zones occur for building height-width ratios greater than or equal to one. The values of the Strouhal numbers may differ versus the results from Sakamoto and Arie due to the addition of a tree downwind from the square cylinder and the general point location used in the calculations; however, the trends are the focus of the research, and show similar results. The Strouhal numbers (St) are calculated for each case using Eq. (2.15),

$$St = \frac{f_c w}{U_o} \tag{2.15}$$

where f_c is the prominent prevailing frequency or the plotted frequency peak, w is the width of 8 m of the square-based building in the x-direction, and U_o is the mean horizontal-velocity, which is approximated as 30 $m \cdot s^{-1}$ based on the horizontal-velocity contours near the top of the simulated domain for each case (Sakamoto and Arie, 1983). The spectral analyses at the inner and downwind points will be analyzed to show varying trends for modified simulations of the building and tree. Calculating each f_c is performed using spectral analyses, then validated by inspecting the videos for the flow recirculation time intervals.

After the unsteady-state simulation reaches several periods of quasi-period solutions, the spectral analysis is performed for each case to interpret the turbulence effects seen in the models. Spectral analyses are performed using FFT processing in Matlab®, by utilizing the "pwelch" function to calculate the power spectrum density (PSD). To perform the spectral analysis, a quasi-steady state time span of 58.9824 s was extracted from the full time span of each time-history for each point, with the time span correlating to the FFT parameter of 2n, where n=16 and the 58.9824 s time span is calculated from multiplying Δt of 0.0009 s and 216. The sampling frequency is 1,111 Hz based on the simulation time step interval of 0.0009 s. These settings are based on capturing the spectral analysis results found in the measurements conducted by Gromke and Ruck (2008). A 50% Blackman-Harris window is applied with an 85% window overlap based on calculating the desired frequency range to contain applicable spectral data (Xu, 2010). The lowest desired frequency, f_{lowest}, and highest desired frequency, $f_{highest}$, are calculated using Eqs. (2.16) and (2.17), respectively,

$$f_{lowest} = \frac{2}{\Delta t \cdot N_{window}} \tag{2.16}$$

$$f_{highest} = \frac{1}{2 \cdot \Delta t} \tag{2.17}$$

where Δt is the time step interval of 0.0009 s and N_{window} is the number of samples taken in a Blackman-Harris window (Xu, 2010). For a full data set of 65,536 total samples and using a 50% window, N_{window}=32,768 samples, to give f_{lowest}=0.068 Hz and $f_{highest}$=555 Hz. Applicable PSD data is taken from the lowest frequency up to the approximate highest frequency with applicable spectral data, f_{app}, which is calculated using Eqs. (2.18) and (2.19), respectively,

$$f_{app} = \frac{2}{2 \cdot \Delta t \cdot M_{windows}} \tag{2.18}$$

$$M_{windows} = \left[\frac{N_{total}}{(1 - overlap) \cdot N_{window}} \right] - 1 \tag{2.19}$$

where $M_{windows}$ is the number of total windows used in the FFT of the full range of time-history data, N_{total} is the total number of samples taken from the time-history data span, and overlap is the decimal equivalent of the window overlap percentage. In each simulation, the FFT calculations are based on N_{total}=65,536 samples and a window overlap of 85%, which give the values of M_{window}=12.3 and f_{app}=45 Hz. The range of applicable PSD data between the lowest frequency of 0.068 Hz and the applicable PSD data frequency of 45 Hz adequately spans across the frequency range between 4 Hz to 40 Hz of the Gromke and Ruck spectral analyses (Gromke and Ruck, 2008).

The PSD plots are presented in a log(frequency)-log(frequency•PSD) form to display an extensive range of the calculated spectral densities based on the broad range of frequencies (Stull, 1988). The Strouhal numbers are used to compare the cases, as well as the general curvature of the PSD data. Using this methodology, the variations in the square cylinder and porous tree CFD models are explored and compared to find trends and relationships between flow field structures and configurations and their corresponding spectral analyses.

2.3.3 Results of the Square Cylinder and Porous Sphere Models with Varying Building Height

A comparison regarding different building heights with the same tree of R_i=250 m^{-1} is analyzed first. The horizontal-velocity contours showing the inner and downwind points for the 8 m, 11 m, and 14 m building height cases are shown in Figs. 2.4(a), 2.4(b), and 2.4(c), respectively, taken at an instant in time. The corresponding turbulent kinetic energy contours are shown in Figs. 2.4(d), 2.4(e), and 2.4(f), respectively. Figure 2.4 also shows the recirculation zones that form intermittently with respect to time downwind from the buildings and the trees.

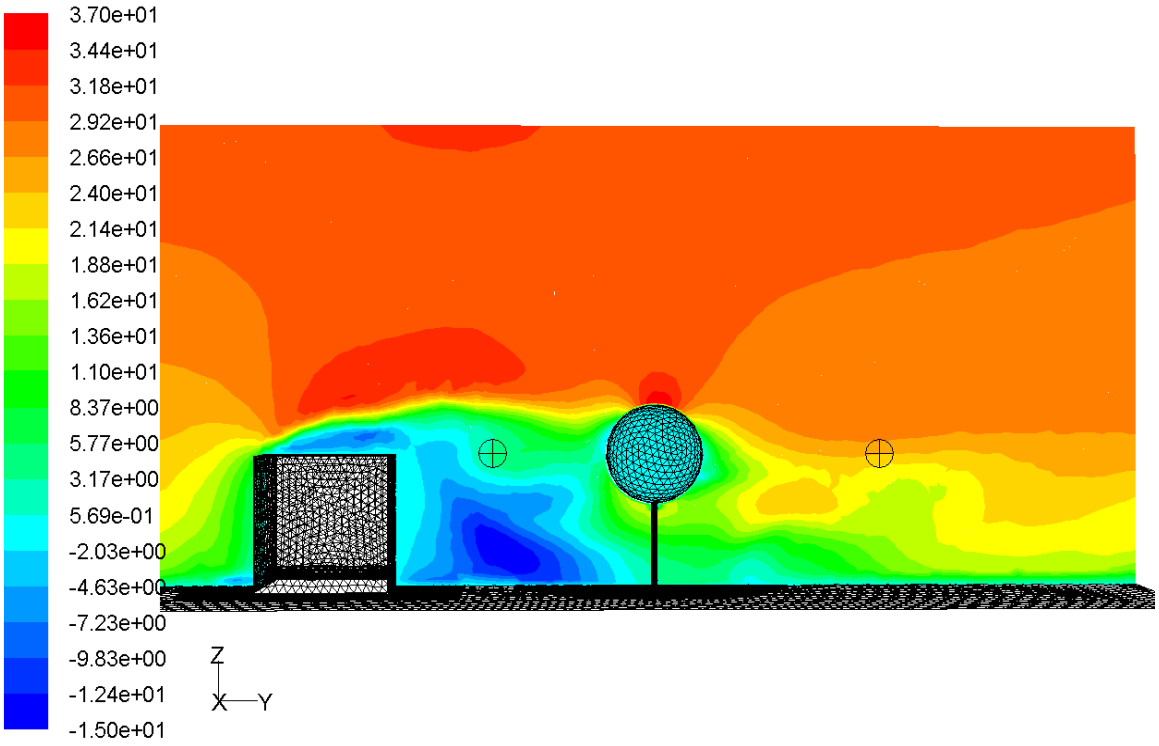

(a) 8 m building horizontal-velocity contour plot

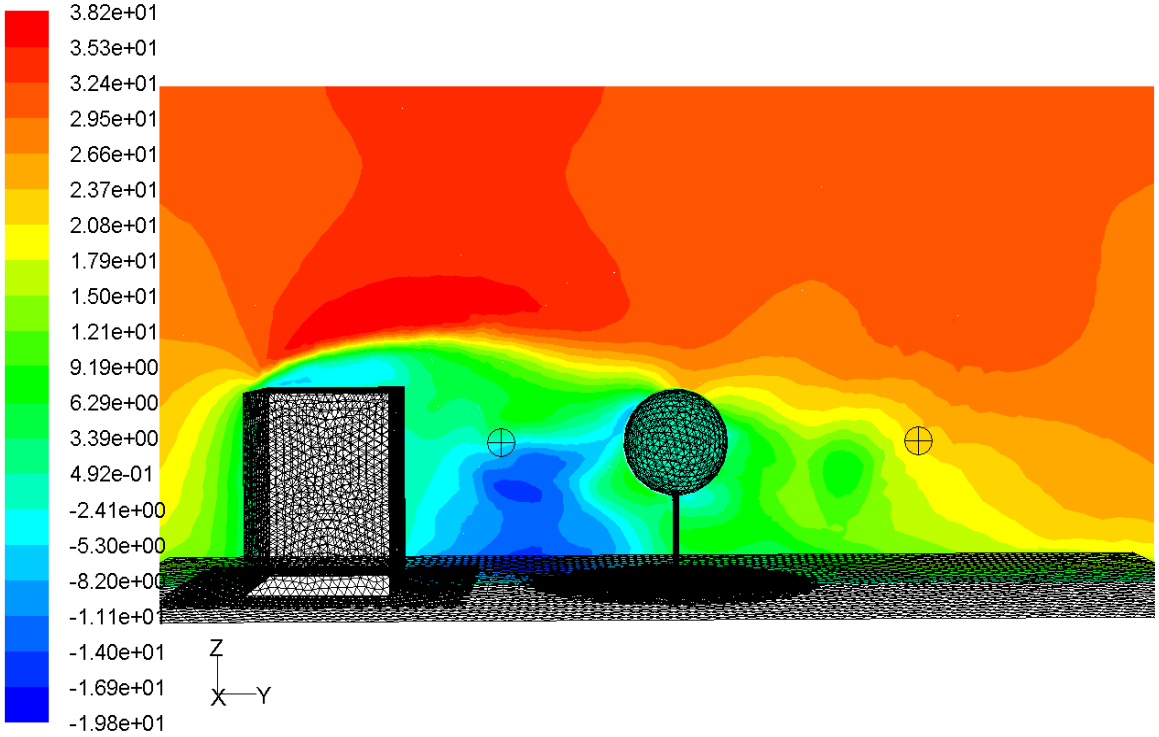

(b) 11 m building horizontal-velocity contour plot

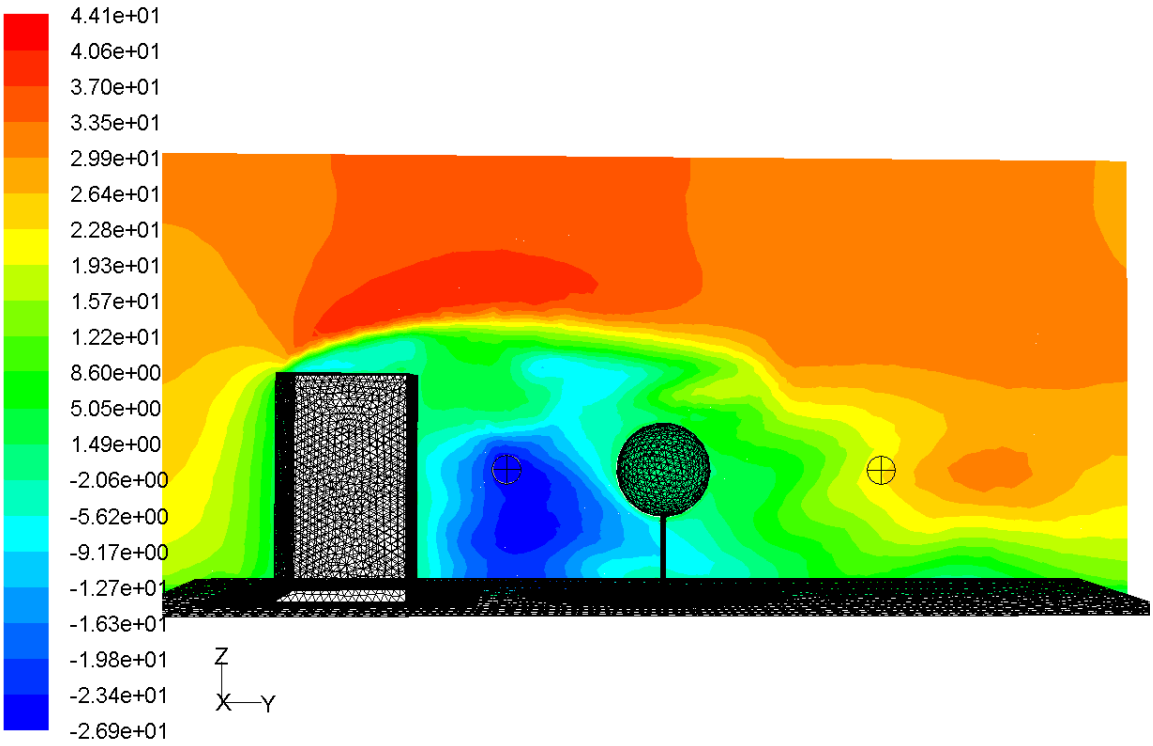

(c) 14 m building horizontal-velocity contour plot

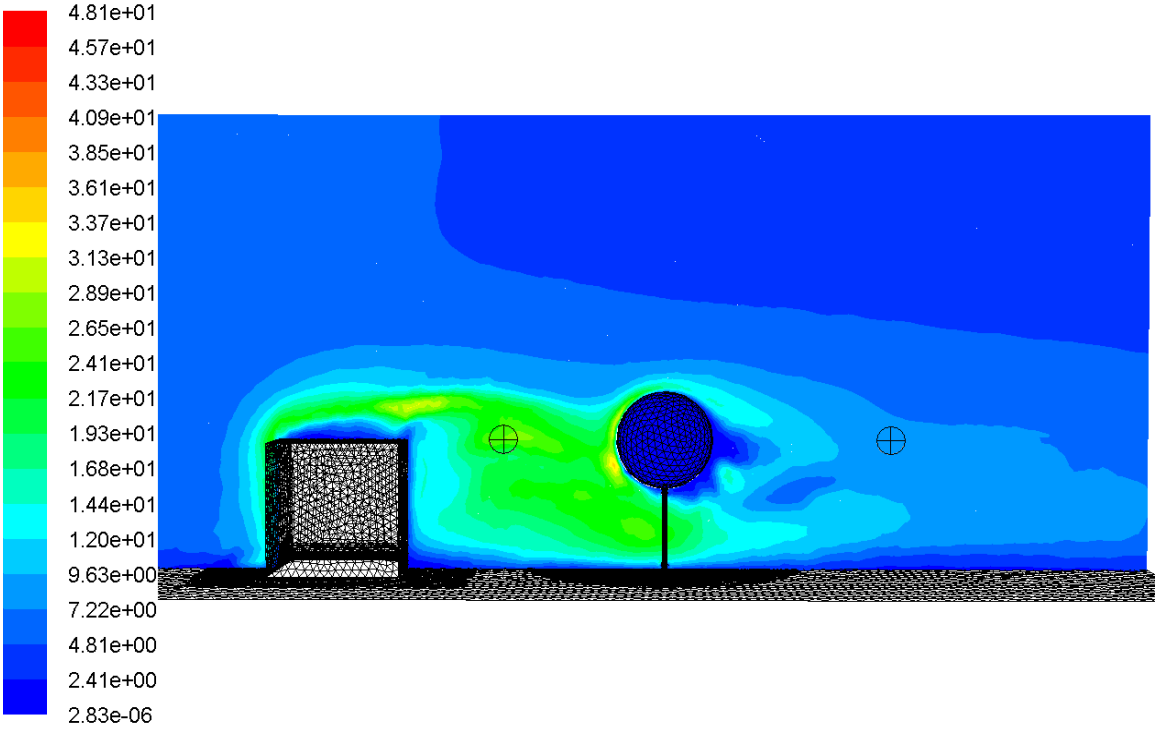

(d) 8 m building turbulent kinetic energy contour plot

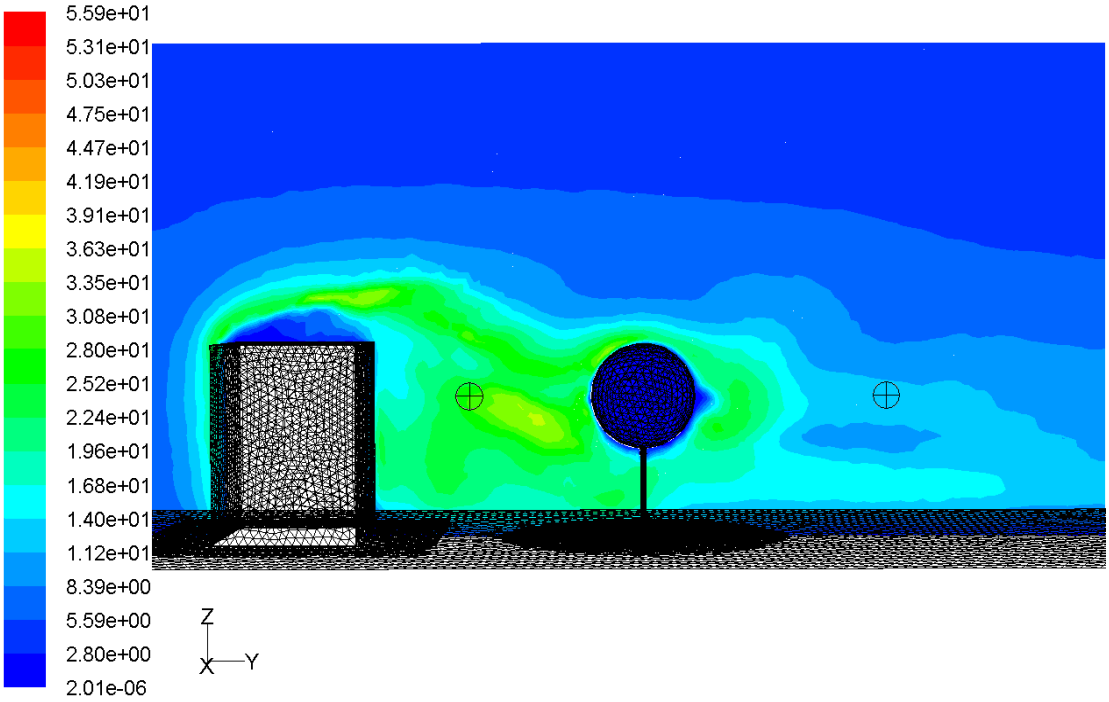

(e) 11 m building turbulent kinetic energy contour plot

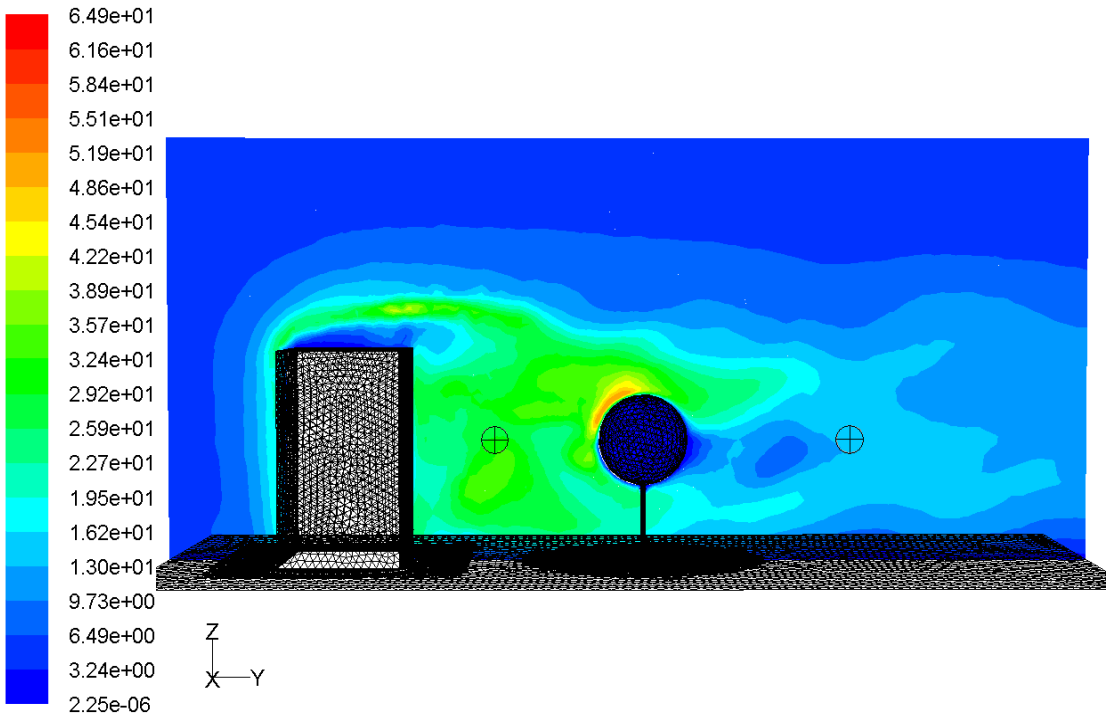

(f) 14 m building turbulent kinetic energy contour plot

Figure 2.4 Contour plots for varying building height

The horizontal-velocity time-history data graphs for the inner and downwind points in the 8 m, 11 m, and 14 m building cases are shown in Figs. 2.5(a), 2.5(c), and 2.5(e), respectively, and exhibit a quasi-steady state nature. Figures 2.5(b), 2.5(d), and 2.5(f) show the corresponding horizontal-velocity spectral analysis data.

For the 8 m building case, from the inner to the downwind point, f_c shifts to a lower frequency on the horizontal-velocity data, from 0.305 Hz to 0.170 Hz as shown in Fig. 2.5(b). Figure 2.5(b) also shows that the frequency·PSD curve of the horizontal-velocity at the inner point is higher than that of the downwind point between 0.07 Hz to 0.7 Hz, but the frequency·PSD curve for the downwind point is higher than that of the inner point beyond 0.7 Hz.

For the 11 m building case, from the inner to the downwind point, f_c shifts to a higher frequency on the horizontal-velocity data, from 0.203 Hz to 0.339 Hz as shown in Fig. 2.5(d). Figure 2.5(d) also shows that the frequency·PSD curve of the horizontal-velocity at the inner point is higher than that of the downwind point between 0.07 Hz to 0.7 Hz, but the curve for the downwind point is higher than that of the inner point beyond 0.7 Hz.

For the 14 m building case, from the inner to the downwind point, f_c shifts to a higher frequency on the horizontal-velocity data, from 0.136 Hz to 0.373 Hz as shown in Fig. 2.5(f). Figure 2.5(f) also shows that the frequency·PSD curve of the horizontal-velocity at the inner point is higher than that of the downwind point between 0.07 Hz to 0.2 Hz, but the curves for both analysis points are approximately equal beyond 0.2 Hz.

The prominent prevailing frequency in each case is difficult to locate by only locating it on the spectral graphs, which is why the video inspection for the time intervals between flow recirculation is necessary. The peak not being clearly distinct from the rest of the FFT curve corresponds to the general abruptness in the flow behavior in each case, where flow recirculation does not occur at discrete time intervals, but varies with time, even with constant inlet log-profile conditions. However, each case does show somewhat discrete time intervals when the average is taken, where this average flow recirculation over a span of time can be used to later estimate turbulent flow behavior based on a general terrain of obstacles based on the prominent prevailing frequency. The curves represent the amount of variance for a given period of time, where the frequency range can be used to evaluate the general time frame of these occurrences.

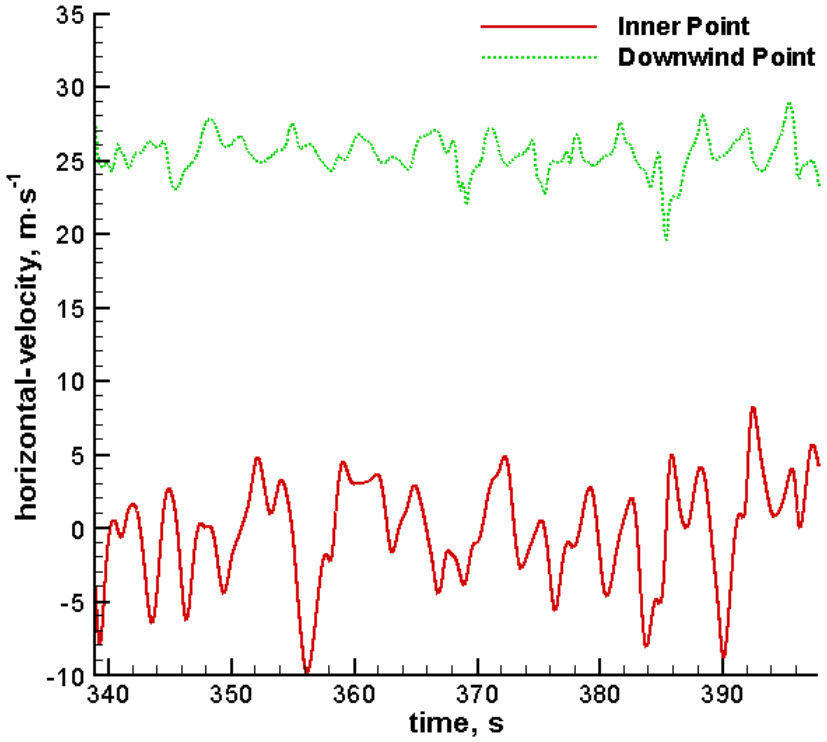

(a) 8 m building horizontal-velocity time-history

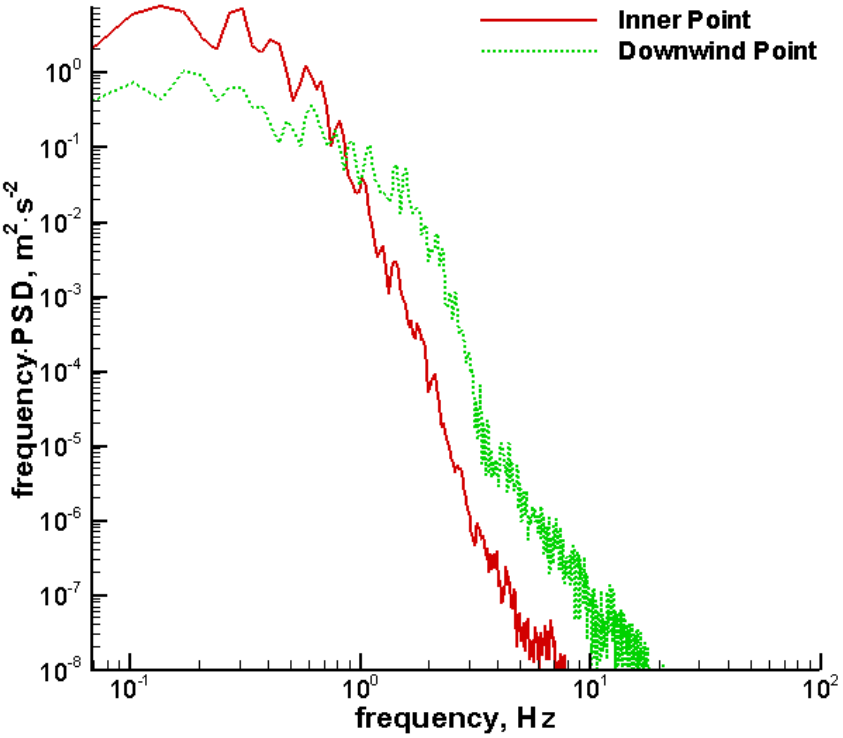

(b) 8 m building horizontal-velocity spectra

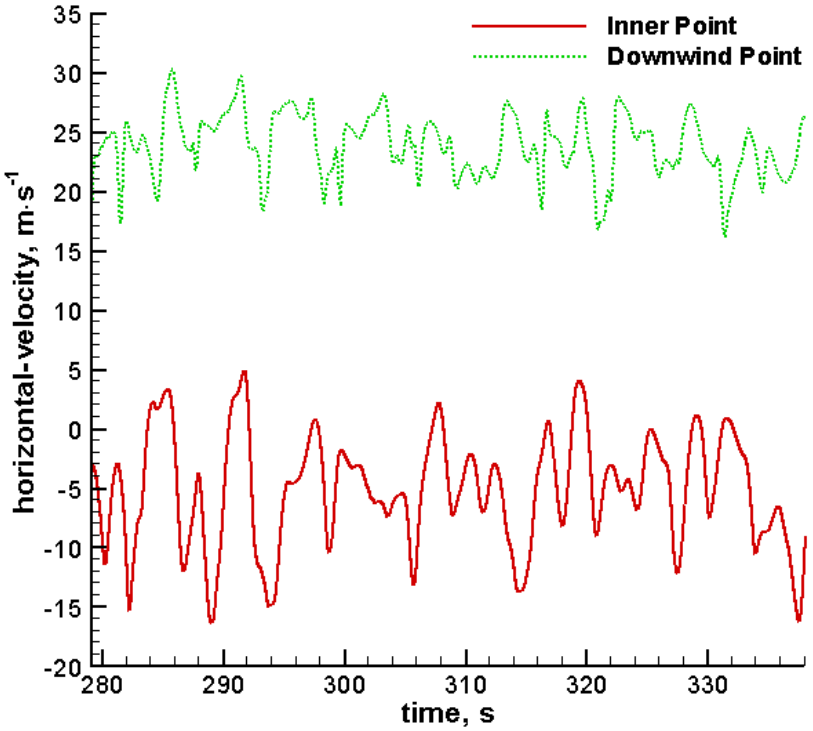

(c) 11 m building horizontal-velocity time-history

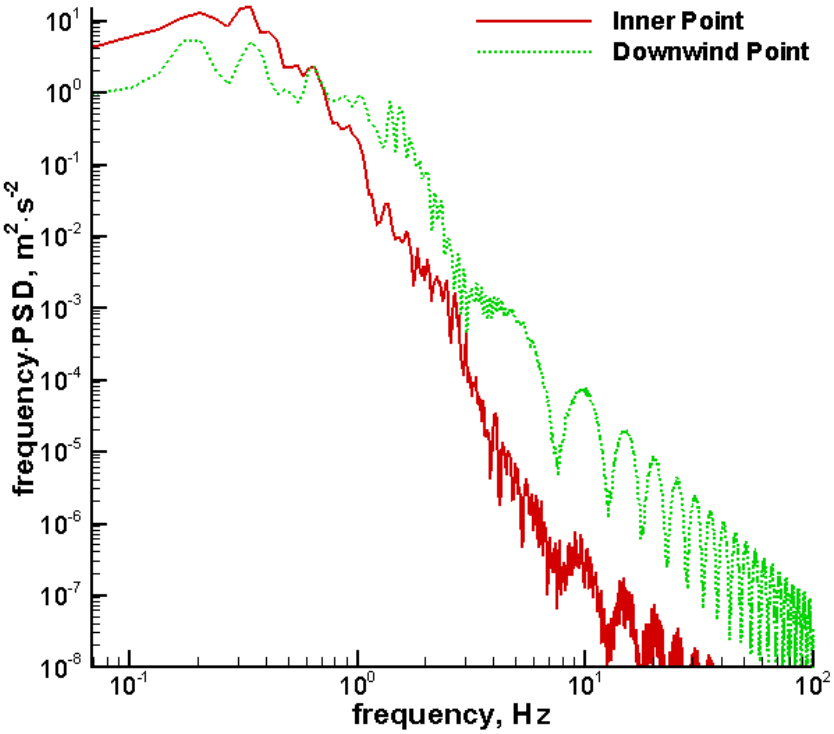

(d) 11 m building horizontal-velocity spectra

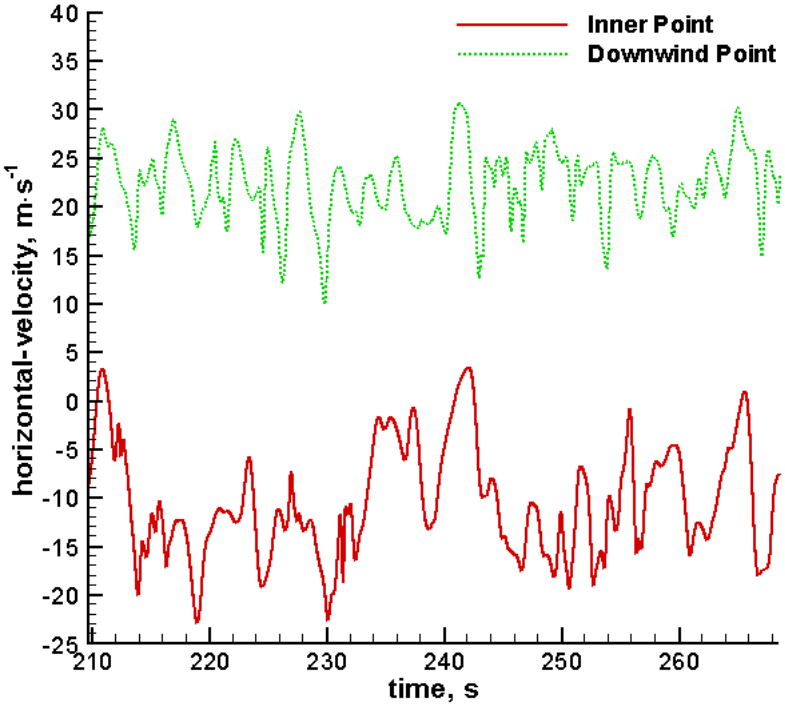

(e) 14 m building horizontal-velocity time-history

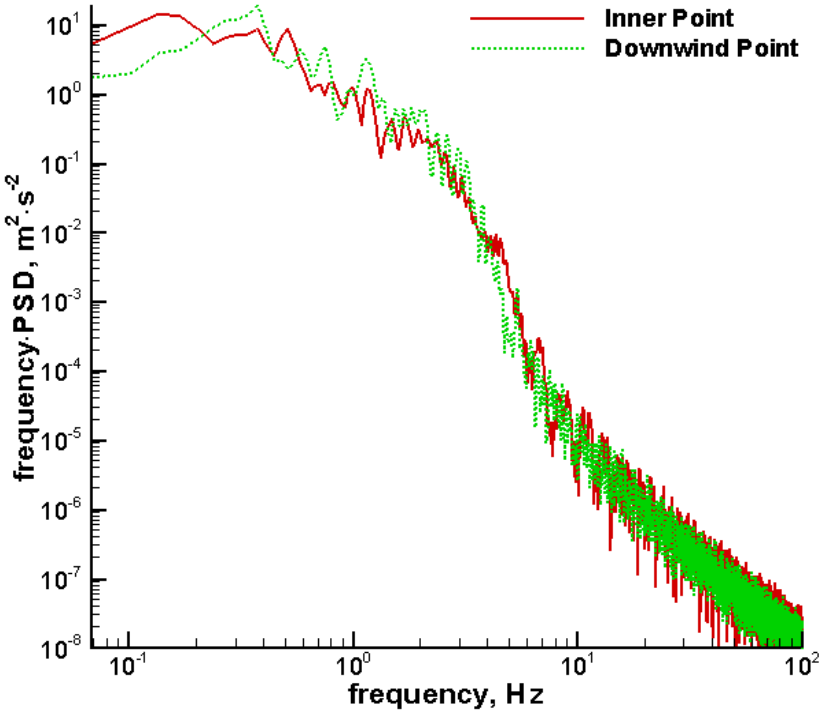

(f) 14 m building horizontal-velocity spectra

Figure 2.5 Horizontal-velocity time-history and FFT data for three building heights

The turbulent kinetic energy time-history data graphs for the inner and downwind points in the 8 m, 11 m, and 14 m building cases are shown in Figs. 2.6(a), 2.6(c), and 2.6(e), respectively, and exhibit a quasi-steady state nature. Figures 2.6(b), 2.6(d), and 2.6(f) show the corresponding turbulent kinetic energy spectral analysis data.

For the 8 m building case, from the inner to the downwind point, f_c shifts to a lower frequency on the turbulent kinetic energy data, from 0.136 Hz to 0.102 Hz as shown in Fig. 2.6(b). Figure 2.6(b) also shows that the frequency·PSD curve of the turbulent kinetic energy at the inner point is higher than that of the downwind point between 0.07 Hz to 2.0 Hz.

For the 11 m building case, from the inner to the downwind point, f_c shifts to a lower frequency on the turbulent kinetic energy data, from 0.305 Hz to 0.170 Hz as shown in Fig. 2.6(d). Figure 2.6(d) also shows that the frequency·PSD curve of the turbulent kinetic energy at the inner point is higher than that of the downwind point between 0.07 Hz to 3.0 Hz, and then the curve for the downwind point is higher than that of the inner point beyond 3.0 Hz.

For the 14 m building case, from the inner to the downwind point, f_c shifts to a higher frequency on the turbulent kinetic energy data, from 0.339 Hz to 0.644 Hz as shown in Fig. 2.6(f). Figure 2.6(f) also shows that the frequency·PSD curve of the turbulent kinetic energy at the inner point is higher than that of the downwind point between 0.07 Hz to 0.7 Hz, but the curves for both analysis points are approximately equal beyond 0.7 Hz.

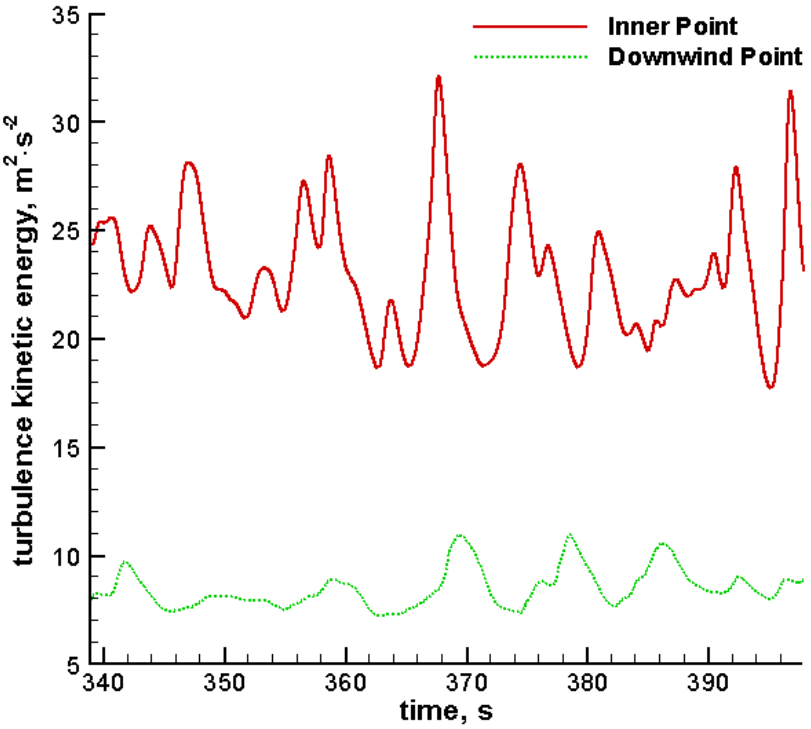

(a) 8 m building turbulent kinetic energy time-history

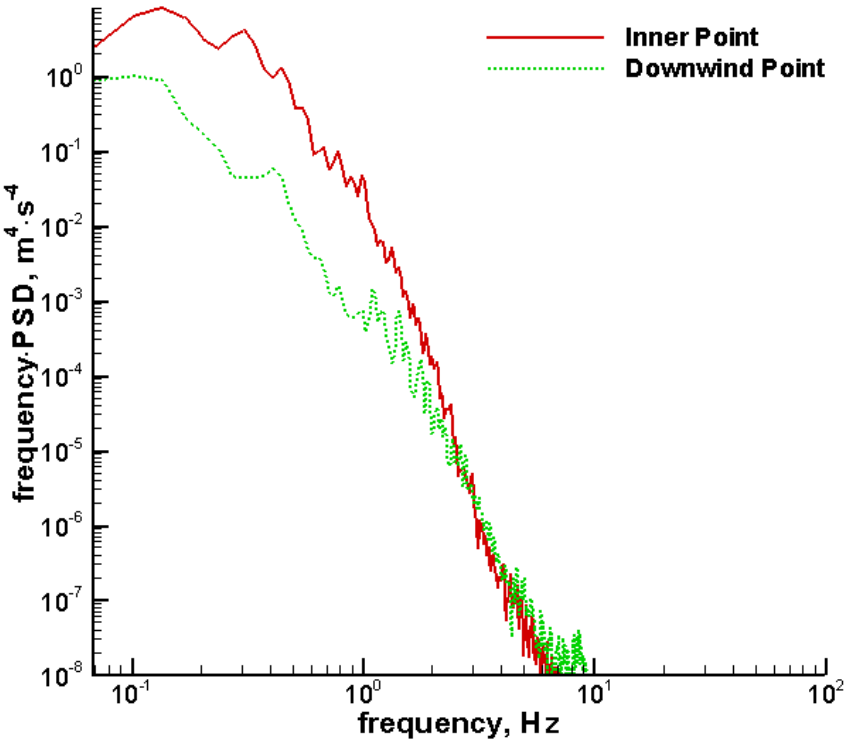

(b) 8 m building turbulent kinetic energy spectra

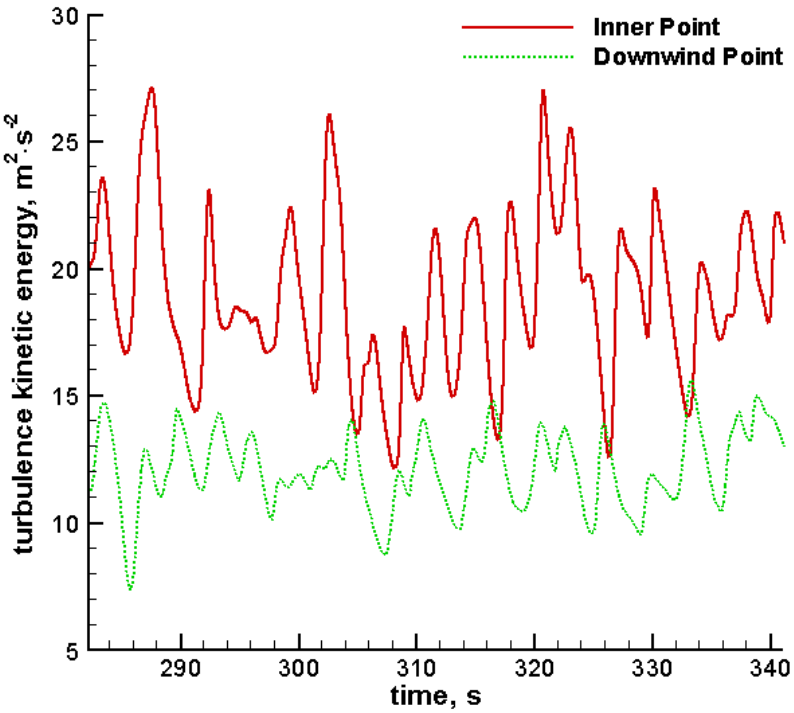

(c) 11 m building turbulent kinetic energy time-history

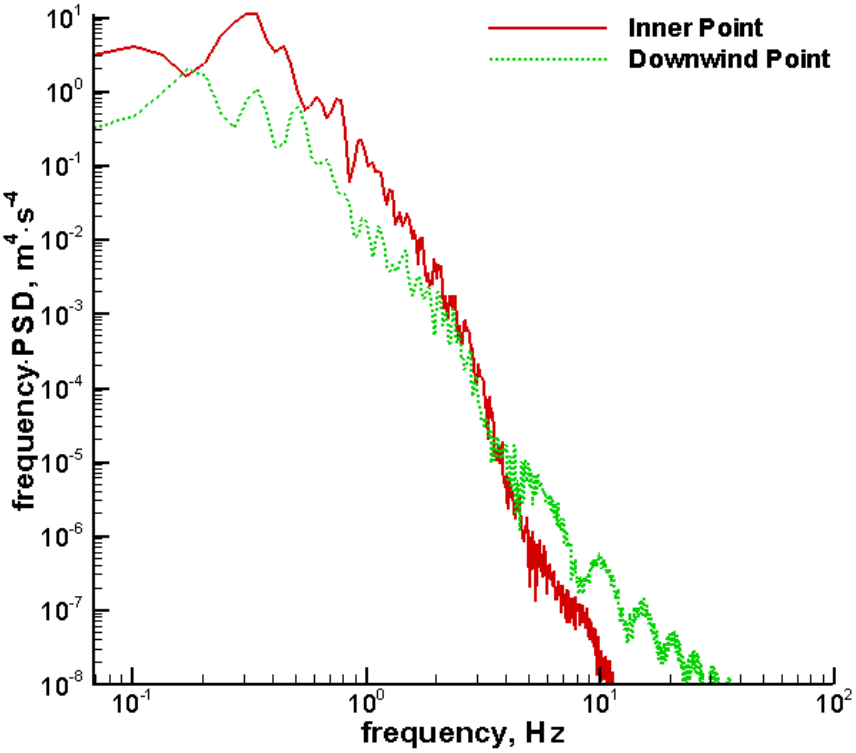

(d) 11 m building turbulent kinetic energy spectra

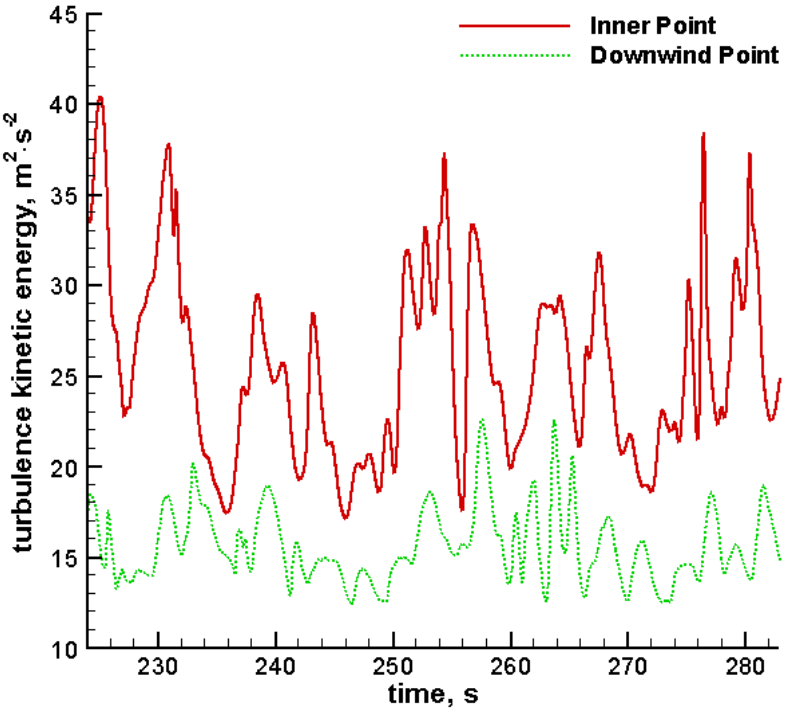

(e) 14 m building turbulent kinetic energy time-history

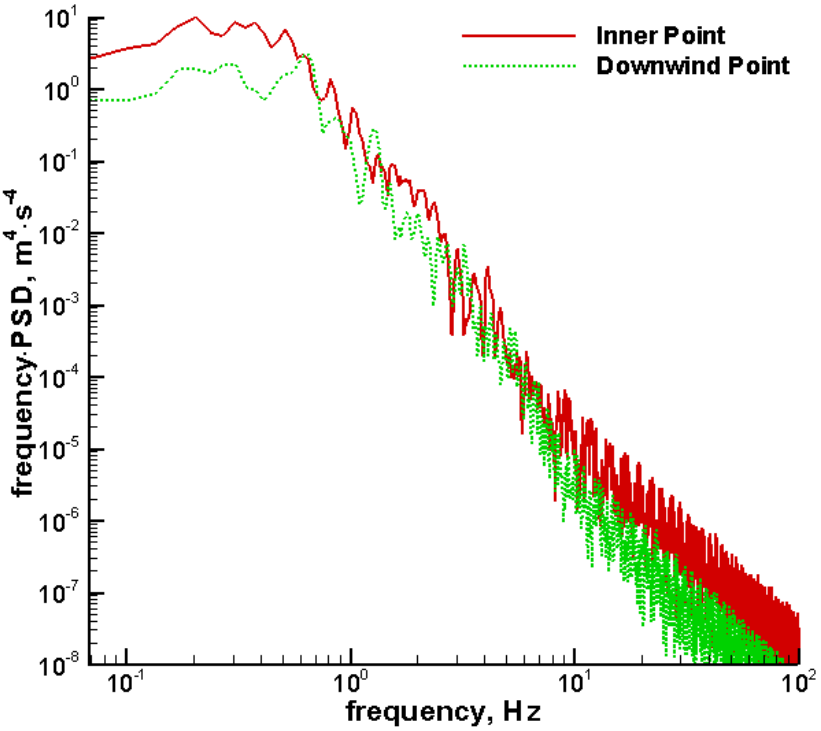

(f) 14 m building turbulent kinetic energy spectra

Figure 2.6 Turbulent kinetic energy time-history and FFT data for three building heights

To compare the three building height cases collectively, the spectral analyses on the horizontal-velocity at the inner and downwind points comparing the three building height cases are shown in Figs. 2.7(a) and 2.7(b), respectively, and on the turbulent kinetic energy at the inner and downwind points in Figs. 2.7(c) and 2.7(d), respectively.

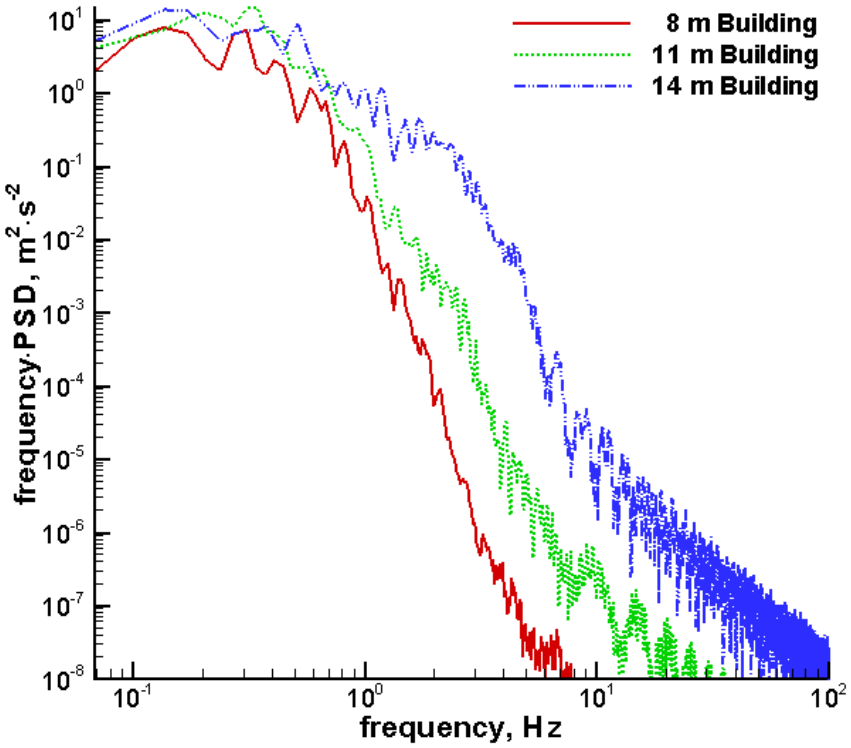

(a) Horizontal-velocity spectra at inner point

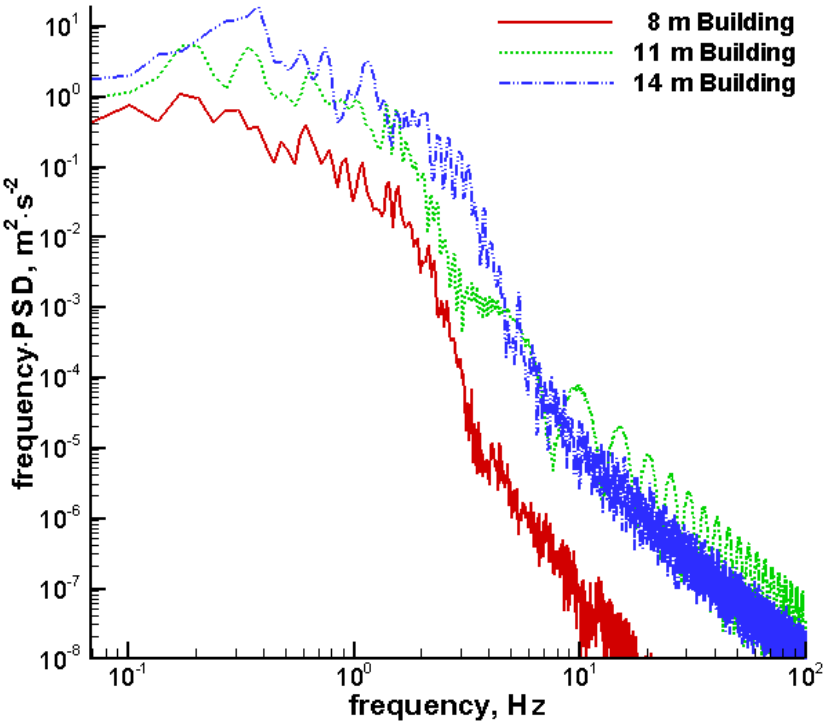

(b) Horizontal-velocity spectra at downwind point

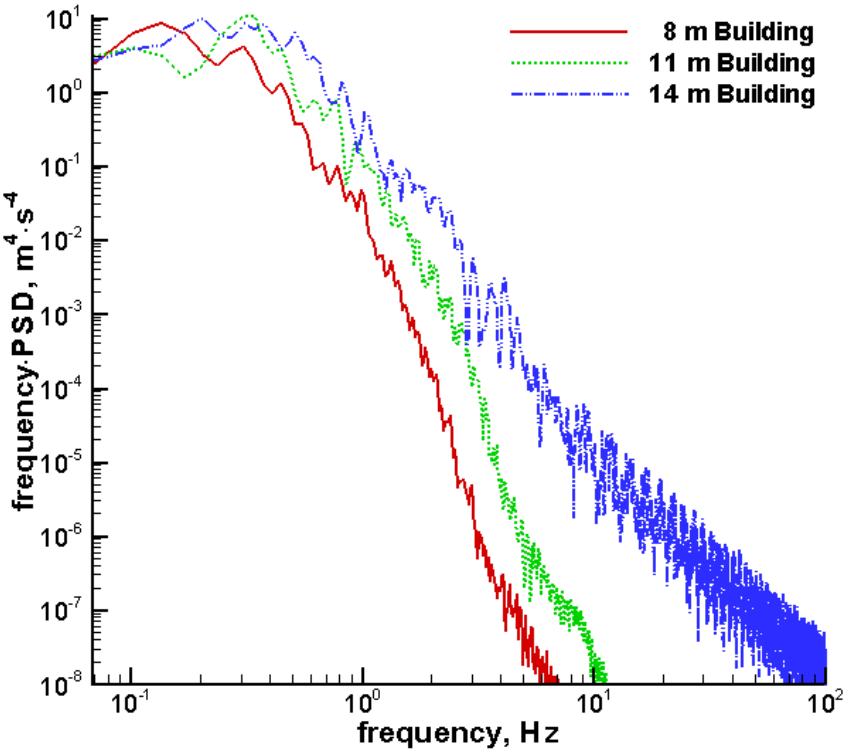

(c) Turbulent kinetic energy spectra at inner point

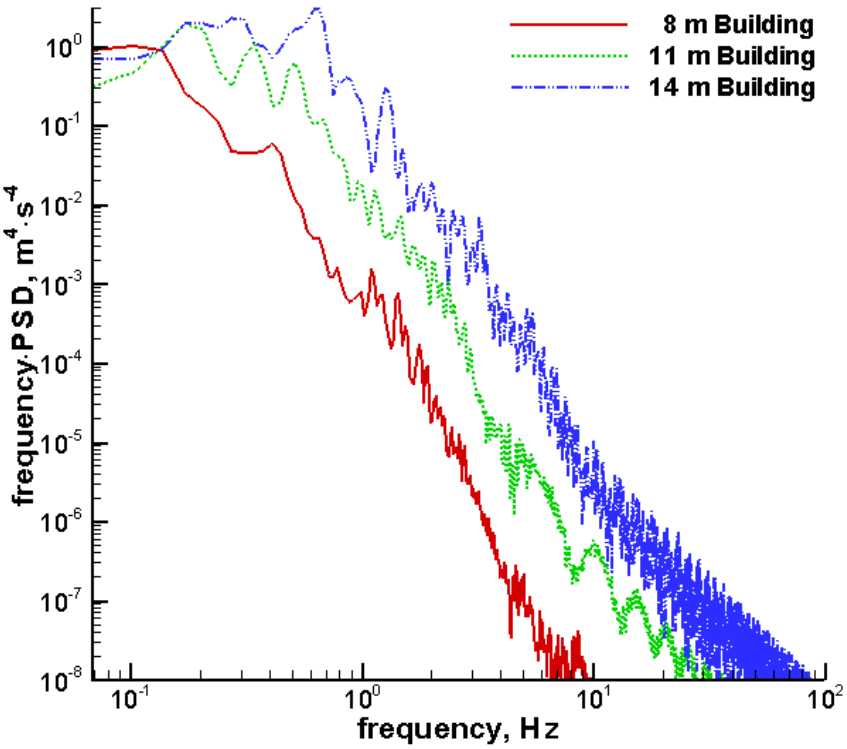

(d) Turbulent kinetic energy spectra at downwind point

Figure 2.7 Collective spectra plots for three separate cases with different building heights

In comparing the spectral analyses between the different building heights, the spectral analysis on the horizontal-velocity at the inner point shows that f_c decreases at a decreasing rate, from 0.305 Hz for the 8 m building to 0.136 Hz for the 14 m building as shown in Fig. 2.7(a). The spectral analysis on the horizontal-velocity at the downwind point shows that f_c increases at a decreasing rate, from 0.170 Hz for the 8 m building to 0.373 Hz for the 14 m building as shown in Fig. 2.7(b). The spectral analysis on the turbulent kinetic energy at the inner point shows that f_c increases at a decreasing rate, from 0.136 Hz for the 8 m building to 0.339 Hz for the 14 m building as shown in Fig. 2.7(c). The spectral analysis on the turbulent kinetic energy at the downwind point shows that f_c increases at an increasing rate, from 0.102 Hz for the 8 m building to 0.644 Hz for the 14 m building as shown in Fig. 2.7(d). The spectral analyses on the three building heights also show a trend in which the increase in building height corresponds to a greater frequency·PSD curve at increasing frequencies. This result matches the trend where an increasing square cylinder height-width ratio from the testing conducted by Sakamoto and Arie (1983).

2.3.4 Results of the Square Cylinder and Porous Sphere Models with the Tree Moved Downwind

The following section presents the differences in the spectral analyses between the case with the initial position of the tree with respect to the building and a case with the tree moved downwind in the y-direction. The case used as the initial position of the tree is the previously discussed 11 m building height case with the tree set with R_i=250 m^{-1}. The tree is moved downwind by 10 m, to central base (x, y, z) coordinates of (13 m, 42 m, 0), and the rectangular domain is extended in the y-direction by 6 m, with (x, y, z) dimensions of (26 m, 68 m, 28 m), to better accommodate and incorporate recirculation downwind from the tree in the flow field. The inner and downwind points are now at the (x, y, z) coordinates of (13 m, 32 m, 8 m) and (13 m, 55.8 m, 8 m), respectively, to maintain their position with respect to the tree as in the initial building and tree CFD model configuration. The horizontal-velocity and turbulent kinetic energy contours for the case with the tree moved downwind are shown in Figs. 2.8(a) and 2.8(b), respectively. The recirculation zones can be visualized by the contours at positions between the building and the tree and downwind of the tree.

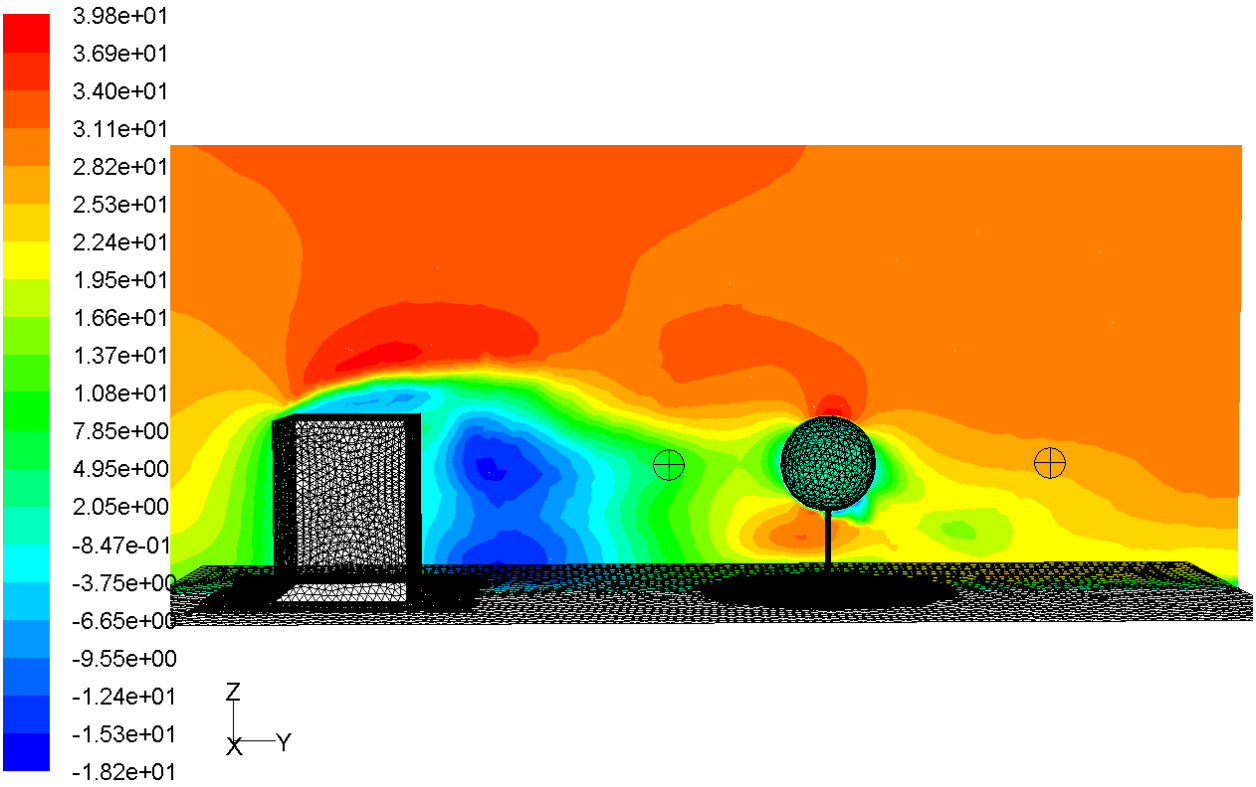

(a) Horizontal-velocity contour plot

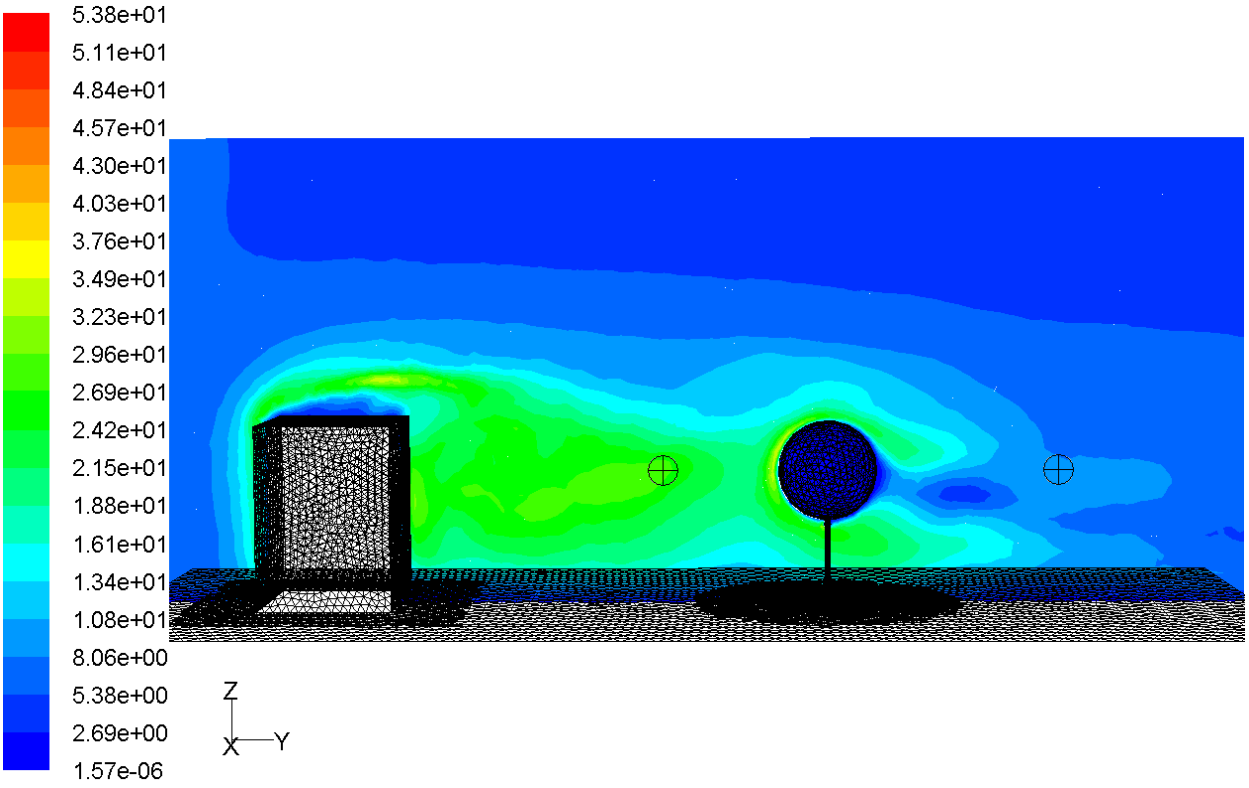

(b) Turbulent kinetic energy contour plot

Figure 2.8 Contour plots of 11 m building with the tree moved 10 m downwind

The horizontal-velocity time-history data for the inner and downwind points in the simulation with the tree moved downwind is shown in Fig. 2.9(a), and exhibits a quasi-steady state nature. Figure 2.9(b) shows the corresponding horizontal-velocity spectral analysis data. Figures 2.9(c) and 2.9(d) show the turbulent kinetic energy time-history and FFT data, respectively.

For the case with the tree moved downwind, from the inner to the downwind point, f_c shifts to a higher frequency on the horizontal-velocity data, from 0.170 Hz to 0.475 Hz as shown in Fig. 2.9(b). From the turbulent kinetic energy FFT data, f_c maintains the value of 0.170 Hz as shown in Fig. 2.9(d). Figures 2.9(b) and 2.9(d) also show that the frequency·PSD curve of the horizontal-velocity as well as the turbulent kinetic energy at the inner point is higher than that of the downwind point for all calculated frequencies.

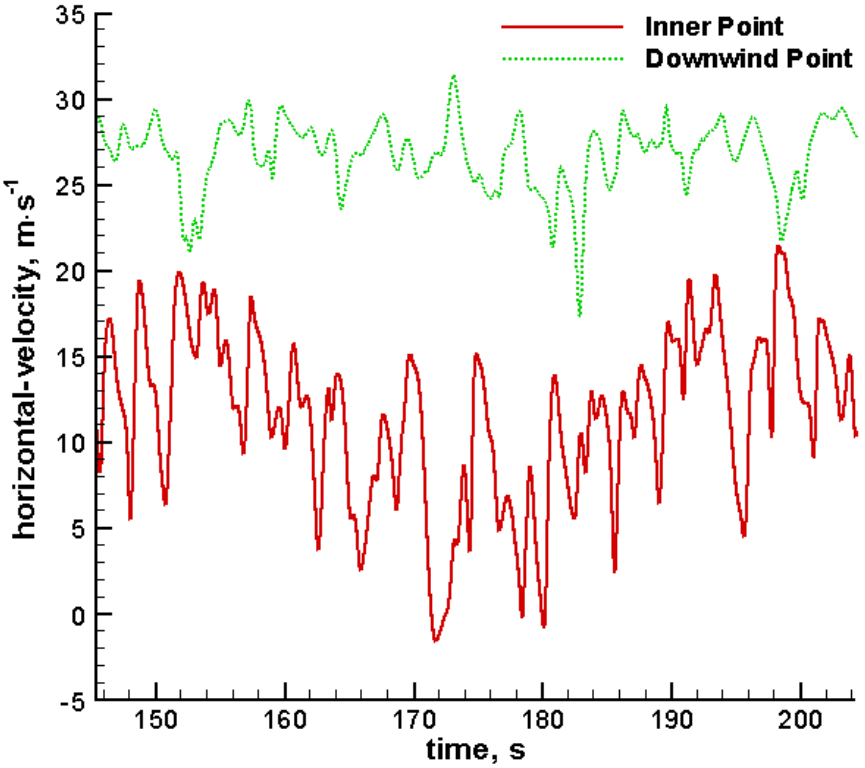

(a) Horizontal-velocity time-history at the inner and downwind points

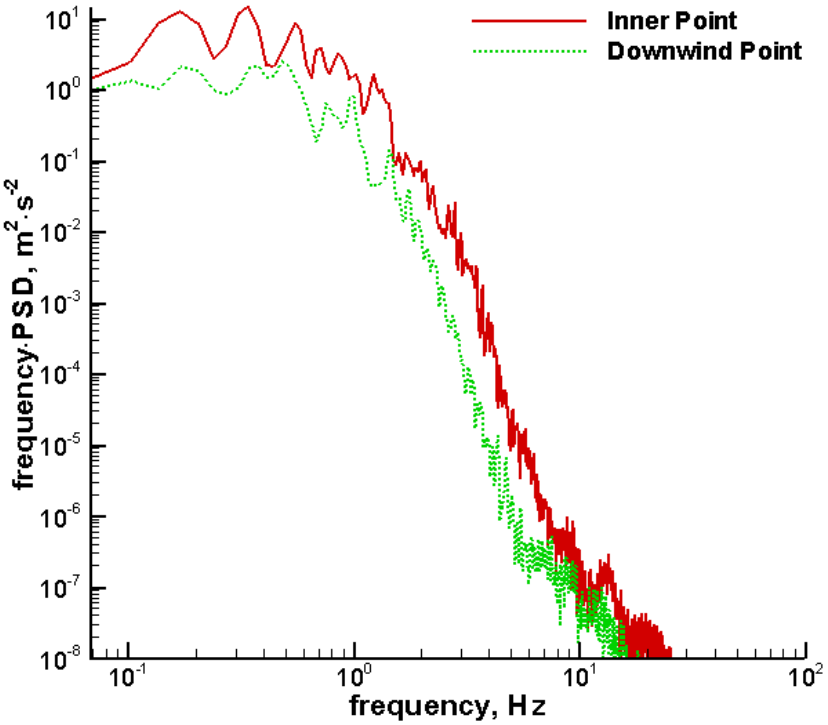

(b) Horizontal-velocity spectra at the inner and downwind points

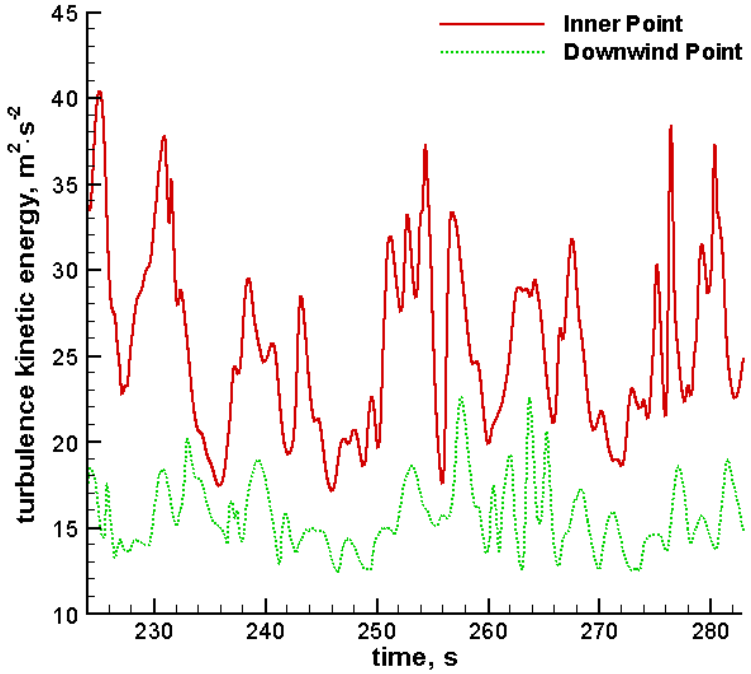

(c) Turbulent kinetic energy time-history at the inner and downwind points

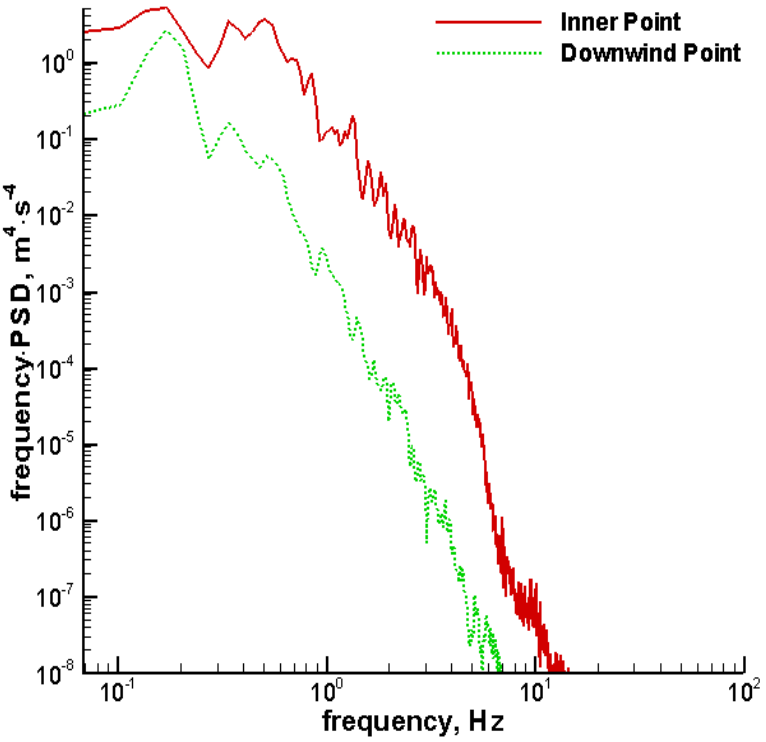

(d) Turbulent kinetic energy spectra at the inner and downwind points

Figure 2.9 Time-history and FFT data for the case with the tree moved 10 m downwind

To compare the initial tree position case versus the case with the tree moved 10 m downwind, their spectral analyses on the horizontal-velocity and turbulent kinetic energy at the inner and downwind points are shown in Fig. 2.10.

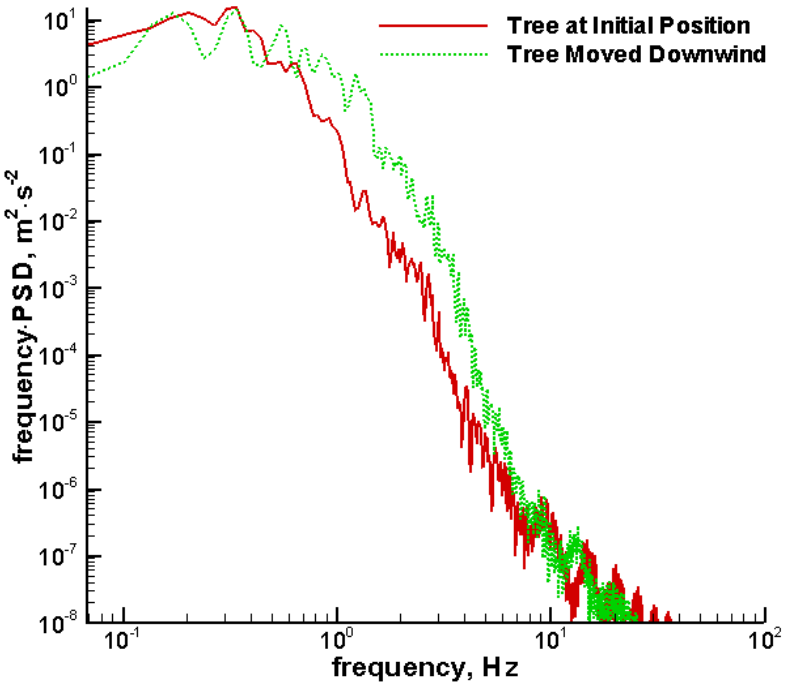

(a) Horizontal-velocity spectra at inner point

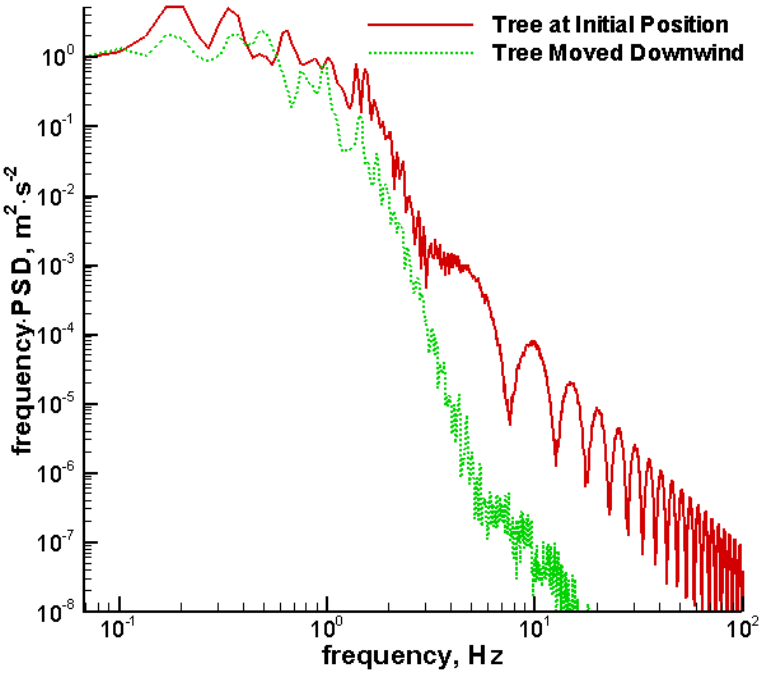

(b) Horizontal-velocity spectra at downwind point

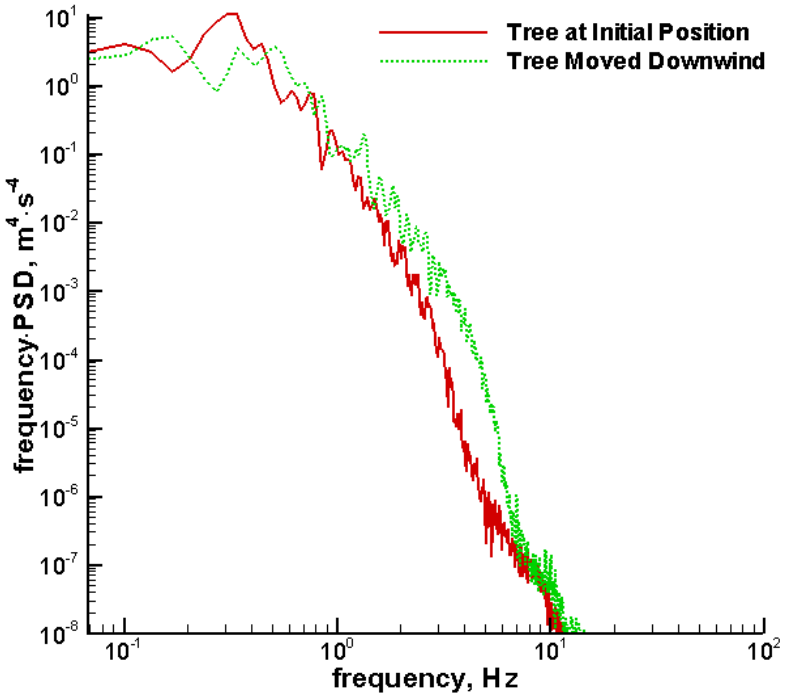

(c) Turbulent kinetic energy spectra at inner point

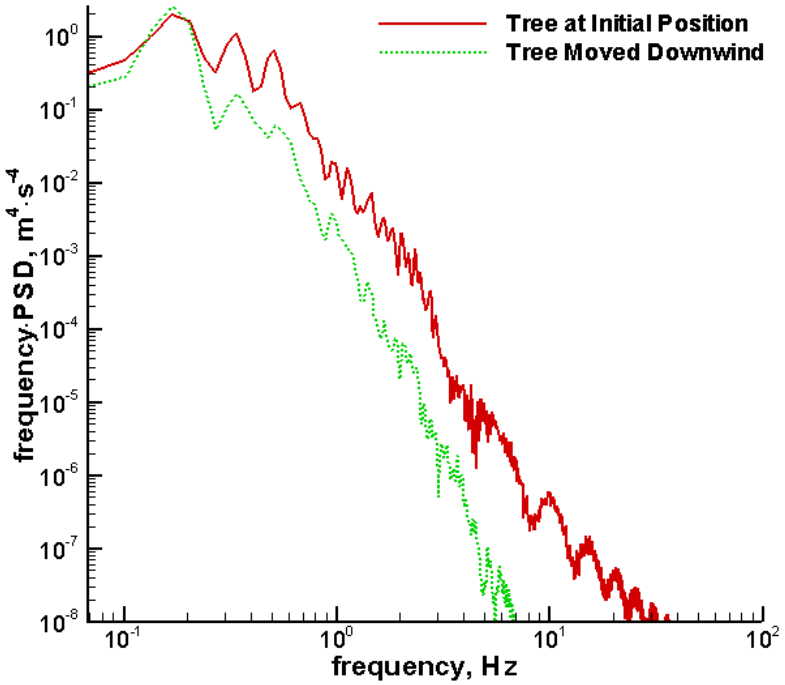

(d) Turbulent kinetic energy spectra at downwind point

Figure 2.10 Spectra comparison between the nominal 11 m building case versus moving the tree 10 m downwind

In comparing the spectral analyses after moving the tree downwind, the spectral analysis on the horizontal-velocity at the inner point shows that f_c decreases from 0.203 Hz initially to 0.170 Hz after moving the tree downwind as shown in Fig. 2.10(a). The spectral analysis on the horizontal-velocity at the downwind point shows that f_c increases from 0.339 Hz initially to 0.475 Hz after moving the tree downwind as shown in Fig. 2.10(b). The spectral analysis on the turbulent kinetic energy at the inner point shows that f_c decreases from 0.305 Hz initially to 0.170 Hz after moving the tree downwind as shown in Fig. 2.10(c). The spectral analysis on the turbulence kinetic energy at the downwind point shows that f_c maintains the value of 0.170 Hz for both cases as shown in Fig. 2.10(d). The spectral analyses between these two cases also show that the frequency·PSD curves for the horizontal-velocity at the inner point, the turbulent kinetic energy at the inner point, and the horizontal-velocity at the downwind point are nearly identical; however, the frequency·PSD curve for the turbulent kinetic energy at the downwind point is lower at increasing frequencies after moving the tree downwind.

2.3.5 Results of the Square Cylinder and Porous Sphere Models with Varying Tree Inertial Resistance

The following section presents the differences in the spectral analyses between cases where the inertial resistance of the spherical tree crown are changed. In addition to the previously discussed 11 m building height case with R_i=250 m^{-1}, other R_i values of $1 \cdot 10^{-9}$ m^{-1}, 17.706 m^{-1}, and 3,500 m^{-1} for the tree crown are simulated. An R_i value of 17.706 m^{-1} is selected based on the wood wool and sisal fiber models created by Gromke and Ruck (2008), where inertial resistances of regular trees will range between 16 m^{-1} to 18 m^{-1} (Gromke and Ruck, 2008). Two additional cases, one case without a tree and another case with a solid tree, are simulated and compared to the arbitrarily chosen extreme values of R_i of $1 \cdot 10^{-9}$ m^{-1} and 3,500 m^{-1}, respectively, to test the validity of the inertial resistance parameter.

The turbulent kinetic energy and horizontal-velocity contours taken at an instant in time for the cases with different inertial resistances of the tree are shown in Fig. 2.11. The recirculation zones that form intermittently can be visualized by the contours at positions downwind of the buildings and the trees.

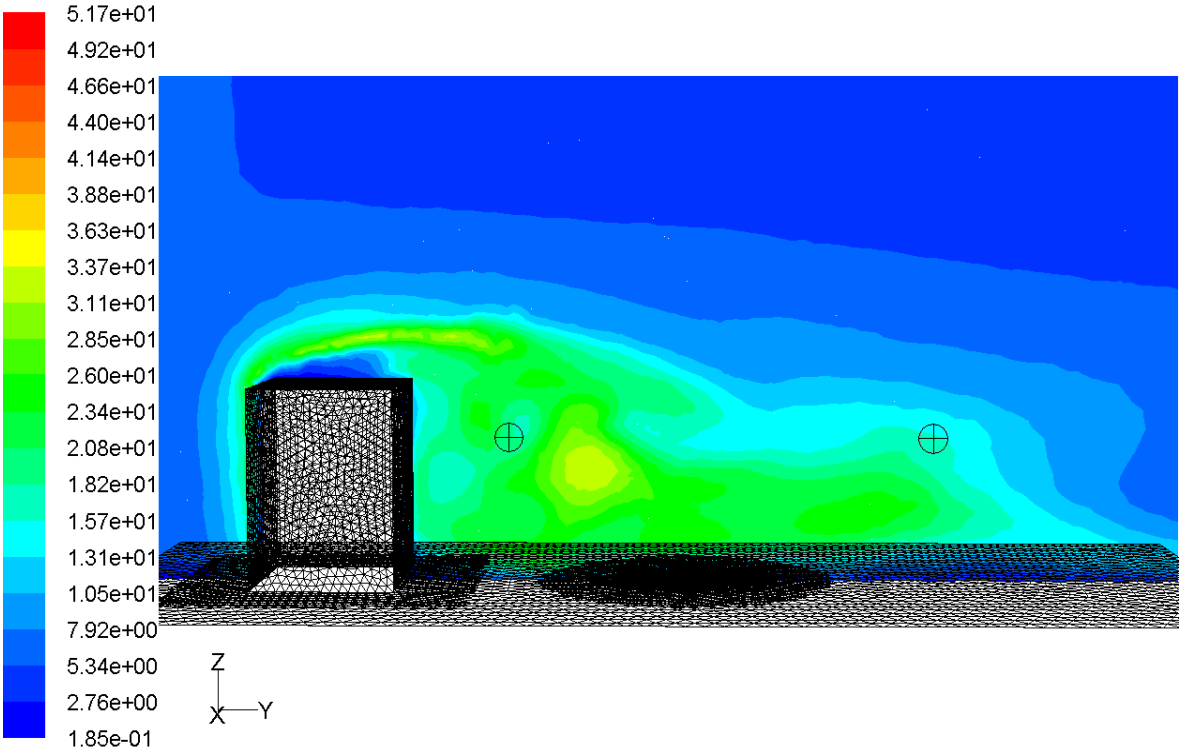

(a) Turbulent kinetic energy contour plot, no tree

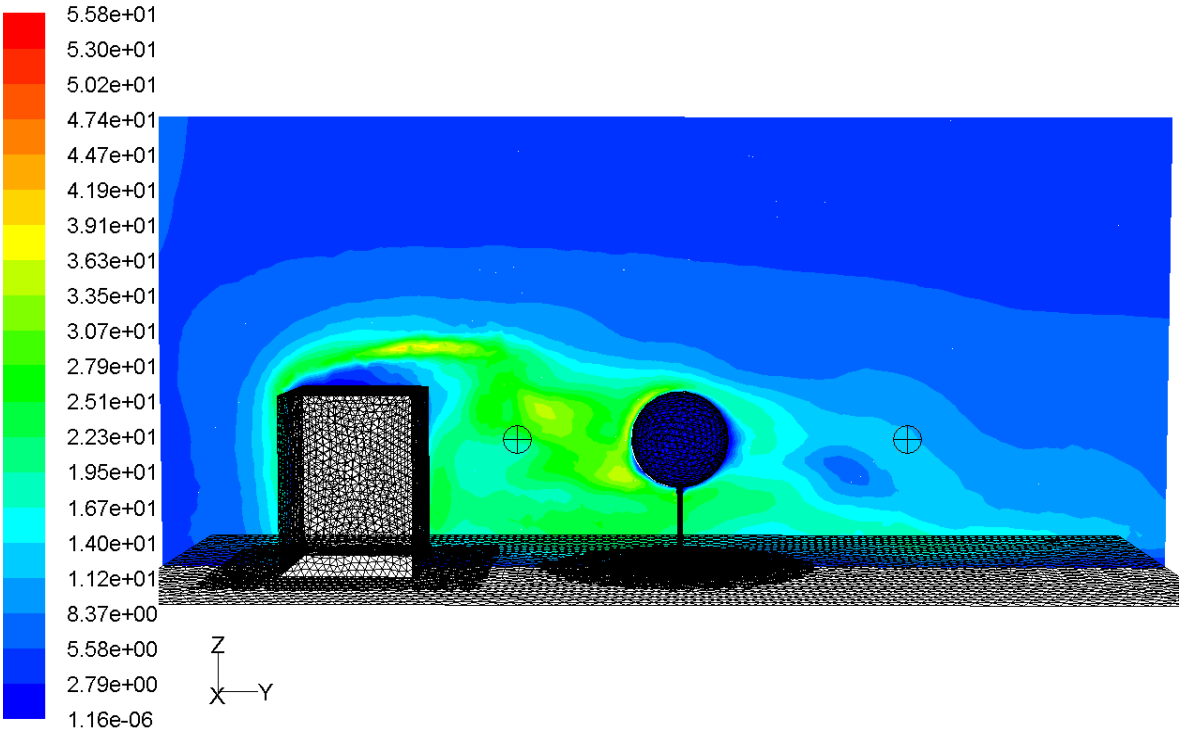

(b) Turbulent kinetic energy contour plot, $R_i=1\bullet10^{-9}$ m^{-1}

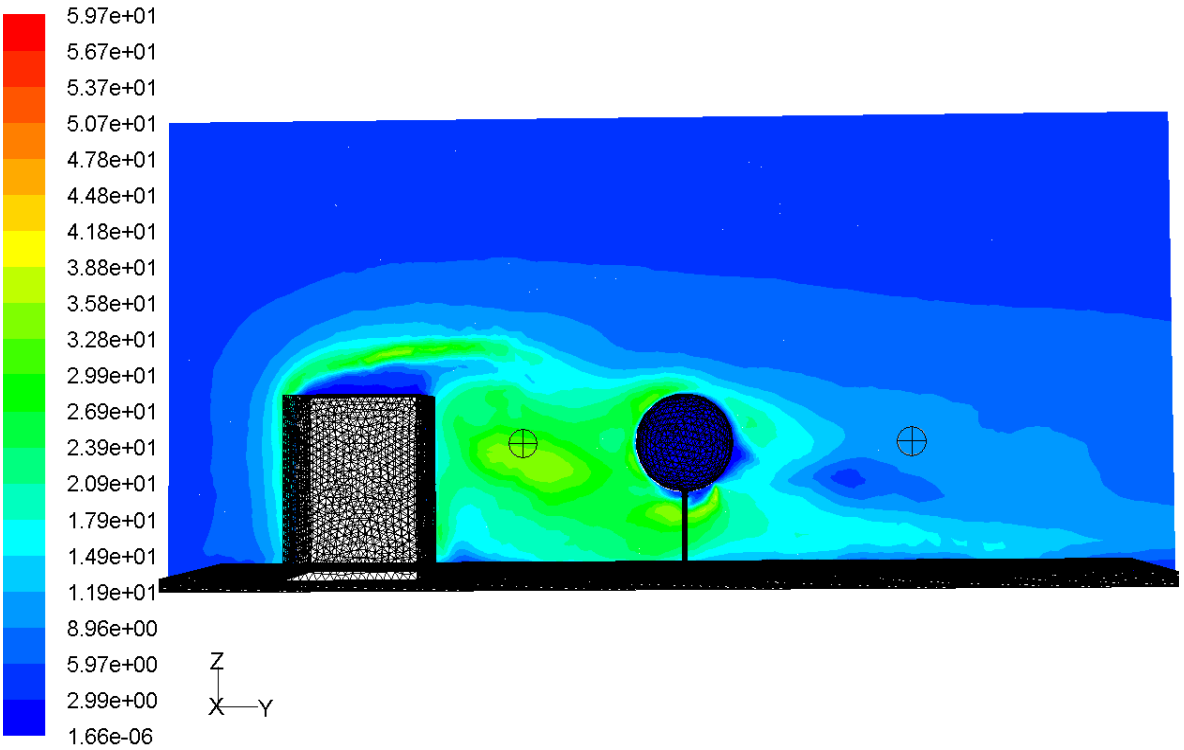

(c) Turbulent kinetic energy contour plot, R_i=17.706 m^{-1}

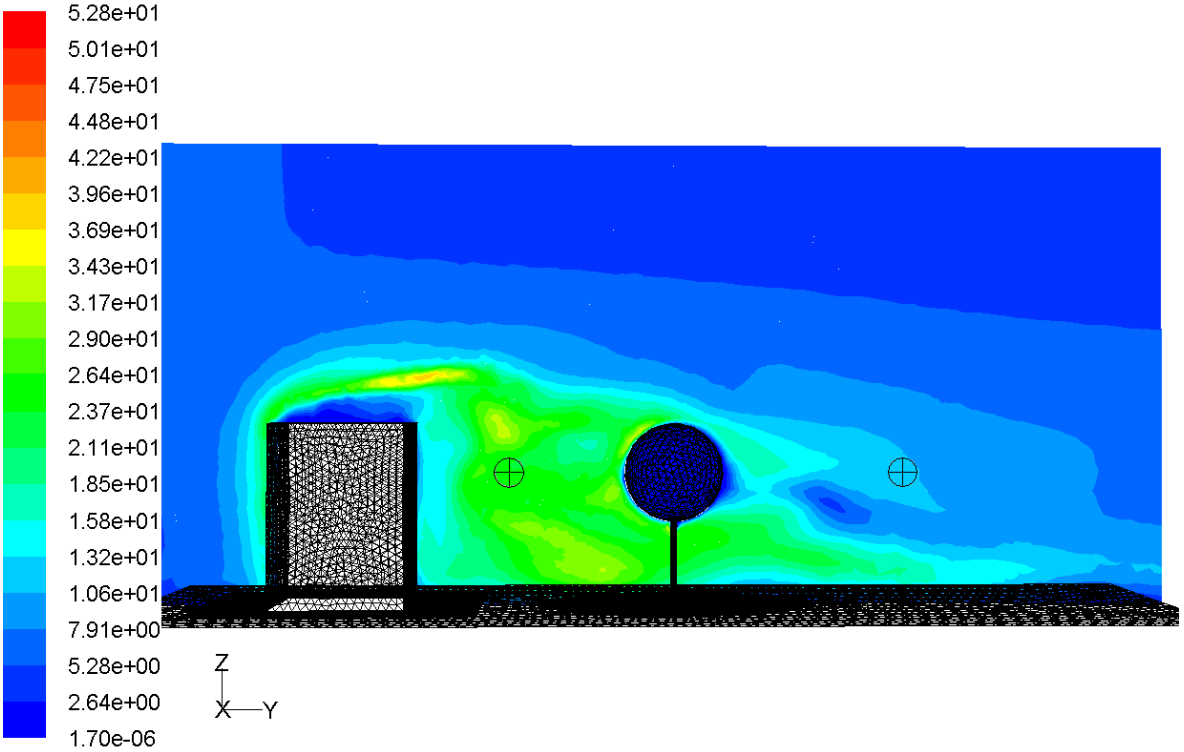

(d) Turbulent kinetic energy contour plot, R_i=3,500 m^{-1}

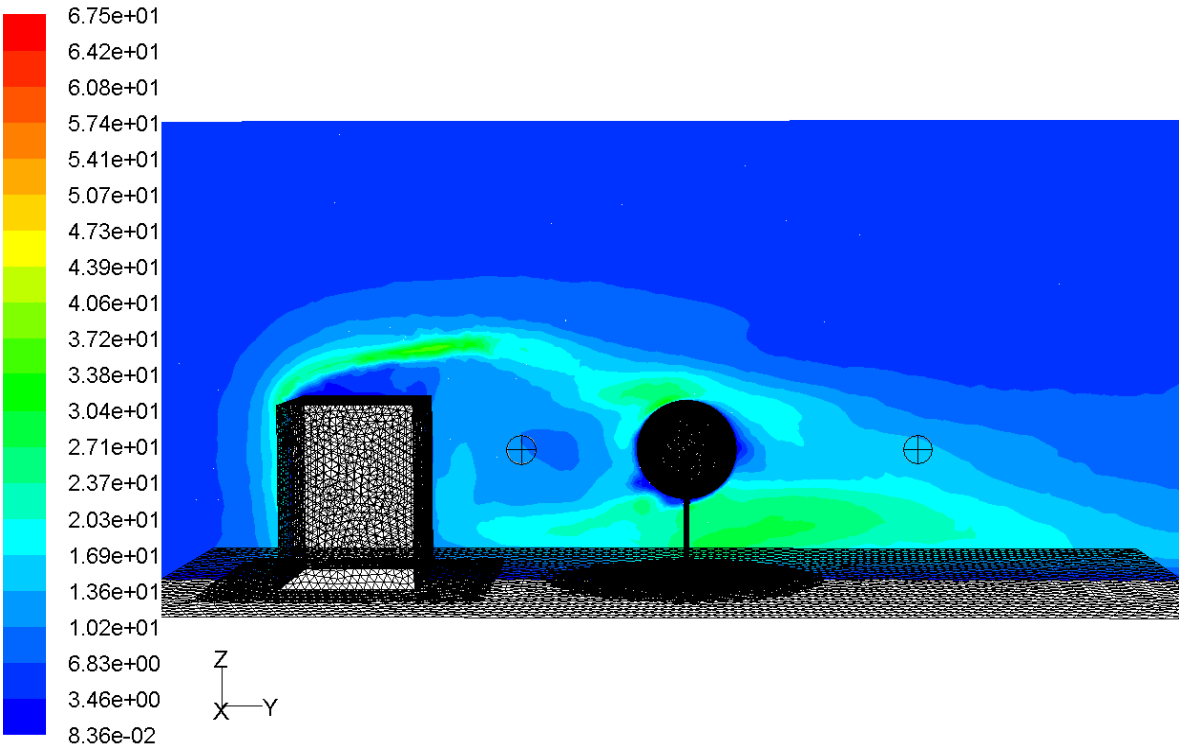

(e) Turbulent kinetic energy contour plot, solid tree

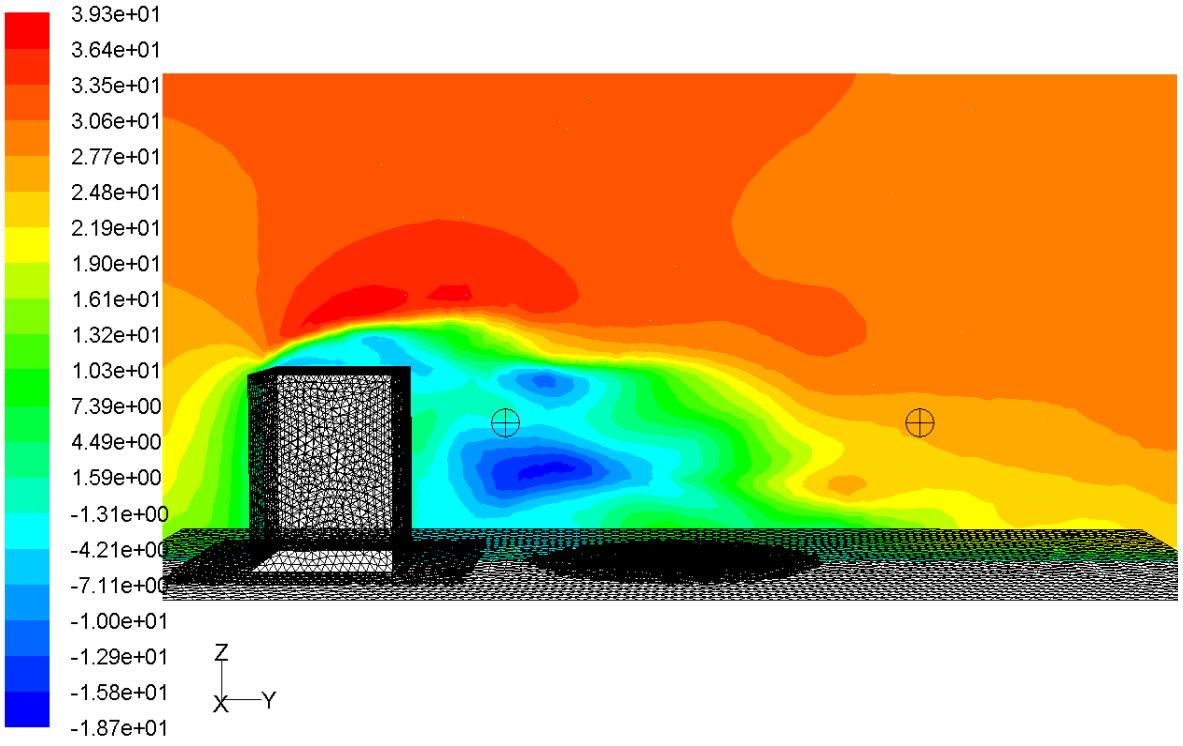

(f) Horizontal-velocity contour plot, no tree

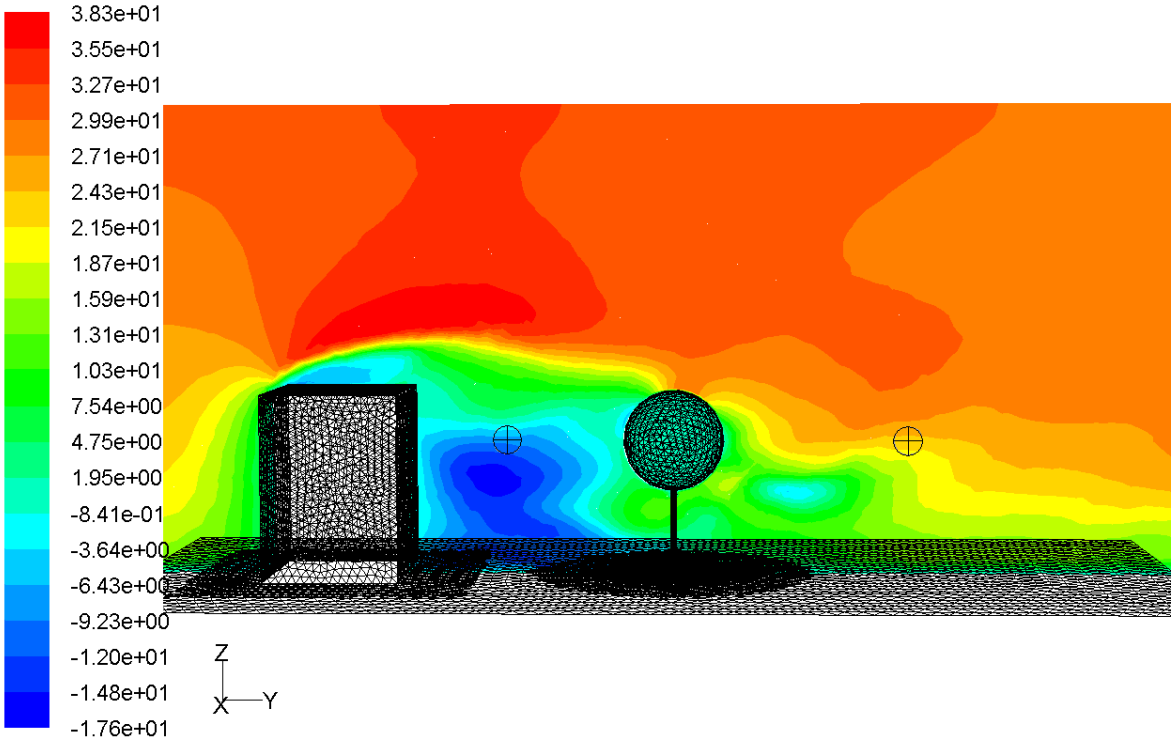

(g) Horizontal-velocity contour plot, $R_i=1\bullet10^{-9}$ m^{-1}

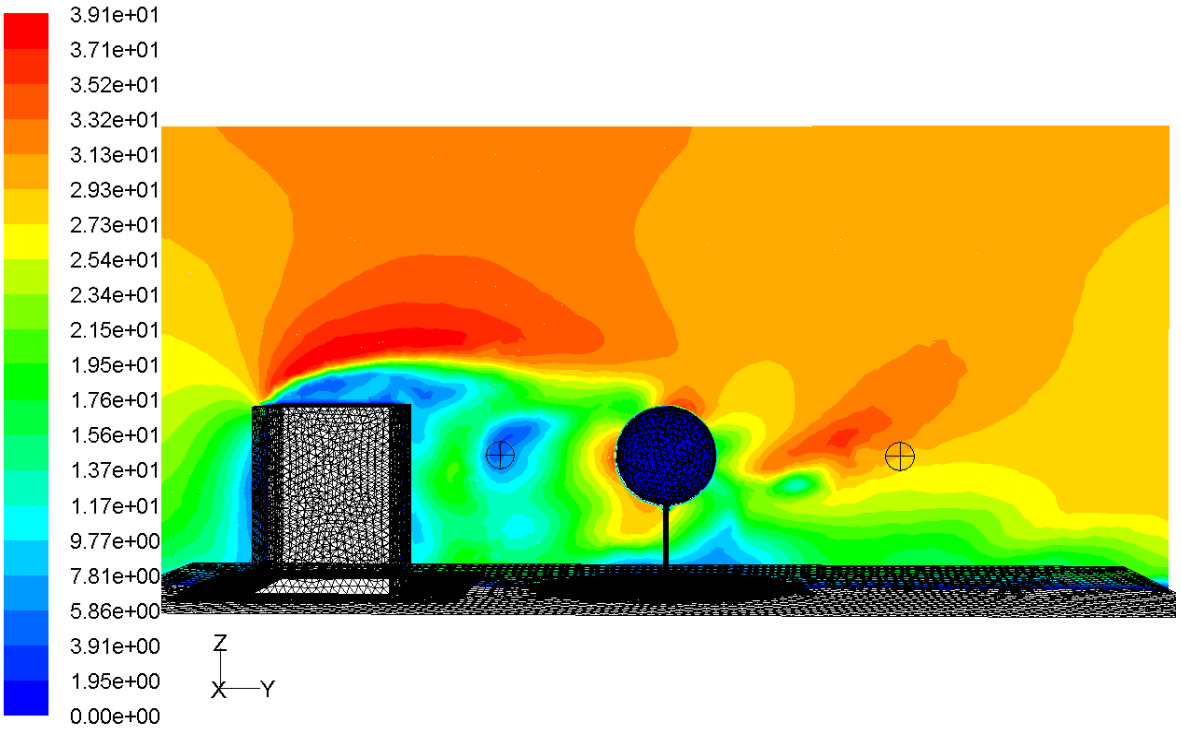

(h) Horizontal-velocity contour plot, $R_i=17.706$ m^{-1}

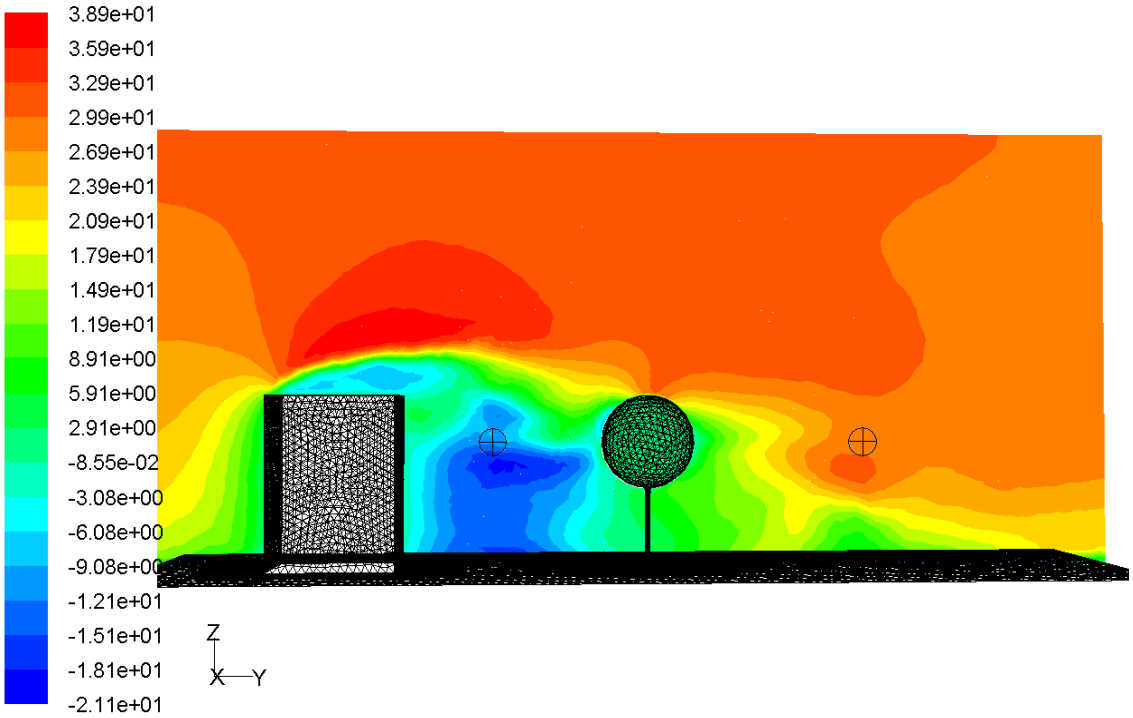

(i) Horizontal-velocity contour plot, R_i=3,500 m^{-1}

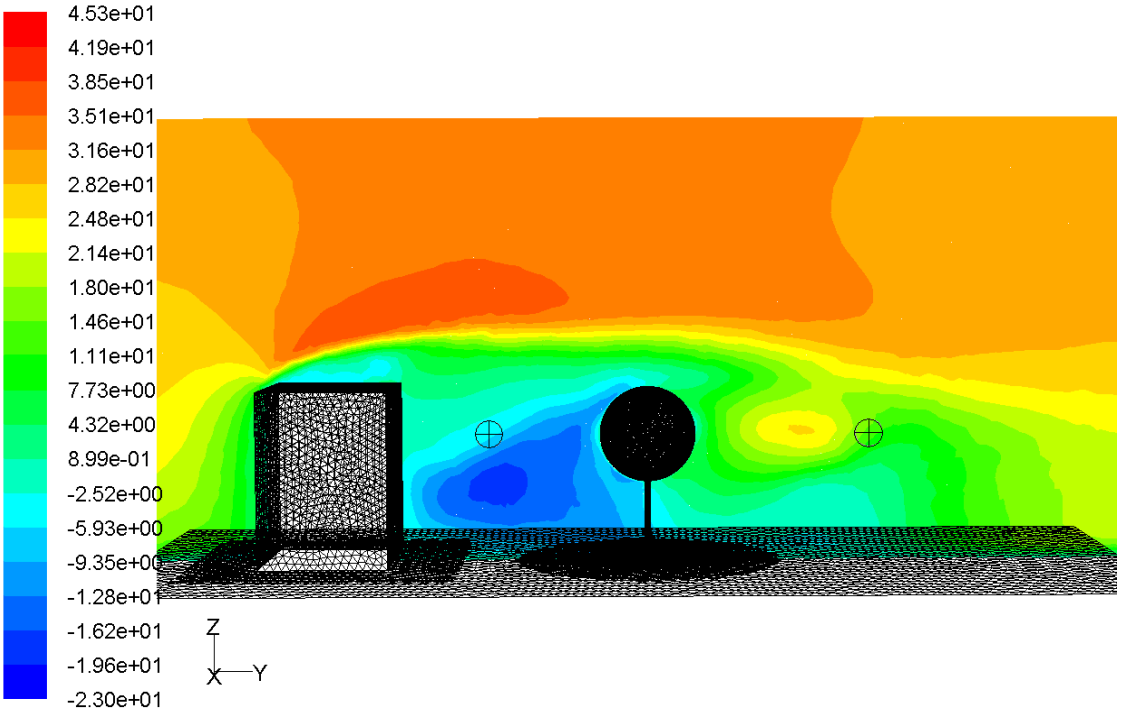

(j) Horizontal-velocity contour plot, solid tree

Figure 2.11 Contour plots for different inertial resistances

The time-history and spectral data for the horizontal-velocity at the inner and downwind points for different inertial resistance values for the tree are shown in Fig. 2.12.

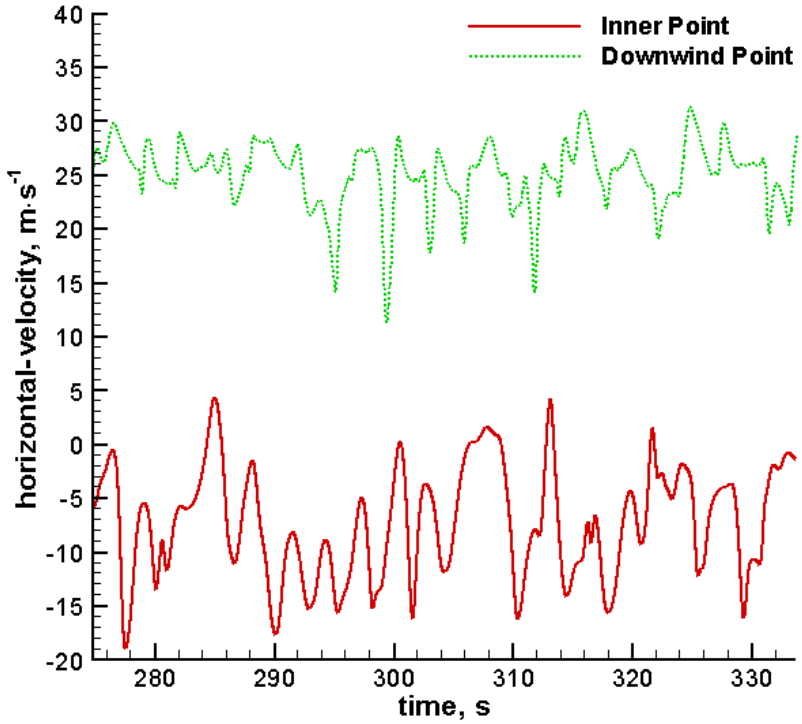

(a) Horizontal-velocity time-history for the inner and downwind points, no tree

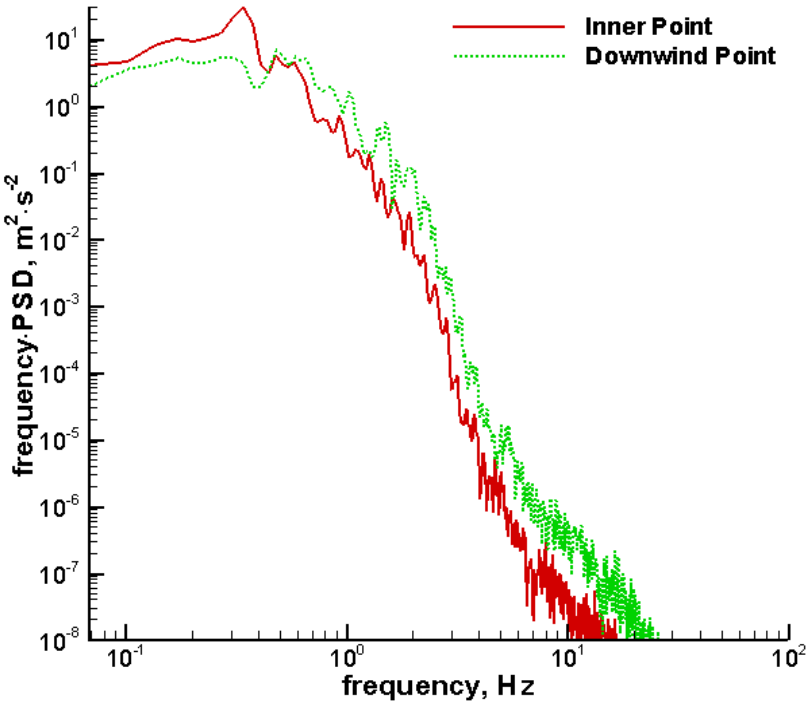

(b) Horizontal-velocity spectra for the inner and downwind points, no tree

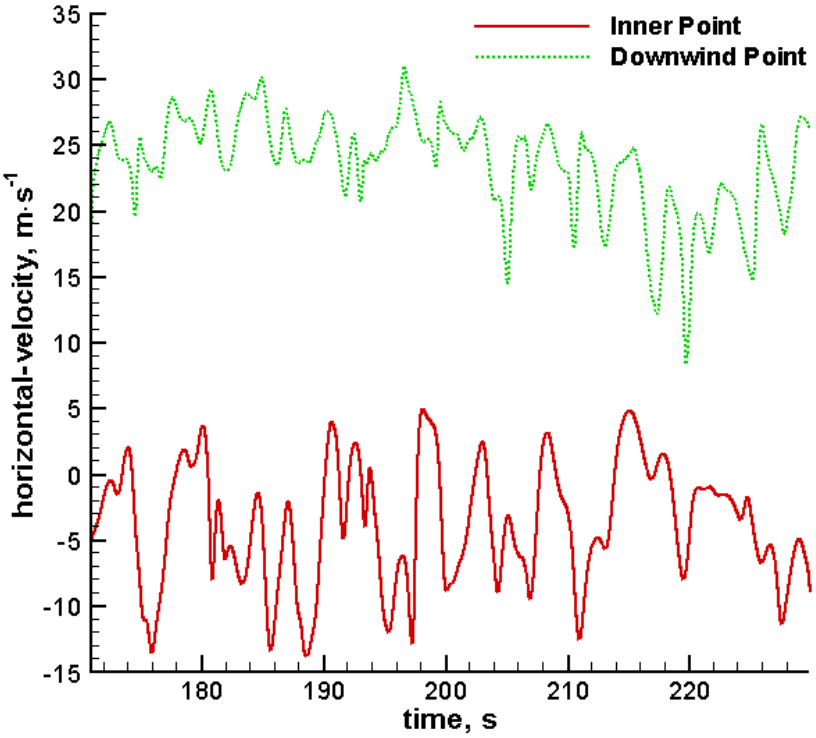

(c) Horizontal-velocity time-history for the inner and downwind points, $R_i=1\bullet10^{-9}$ m^{-1}

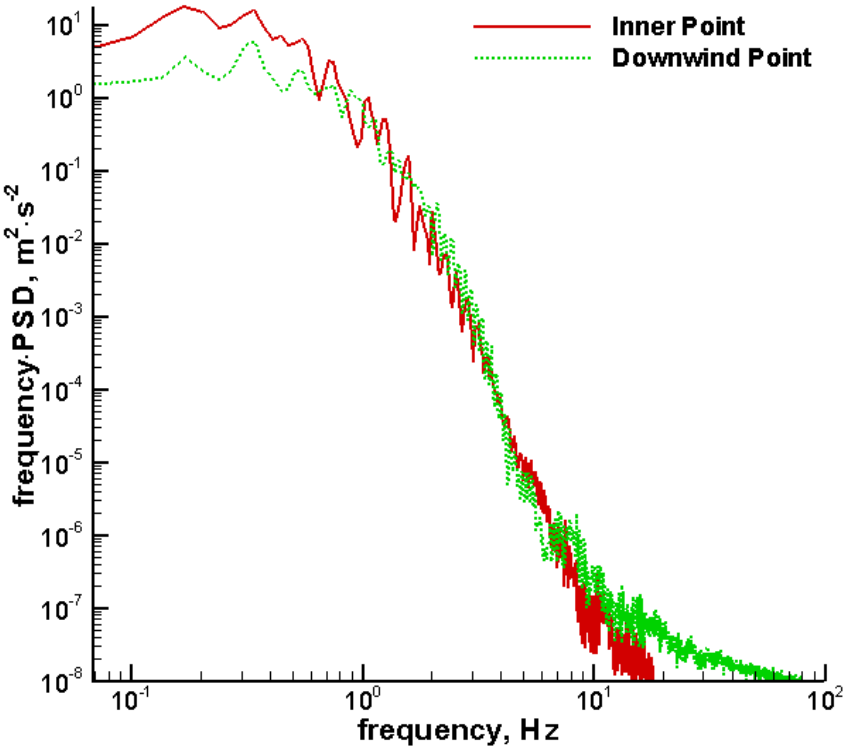

(d) Horizontal-velocity spectra for the inner and downwind points, $R_i=1\bullet10^{-9}$ m^{-1}

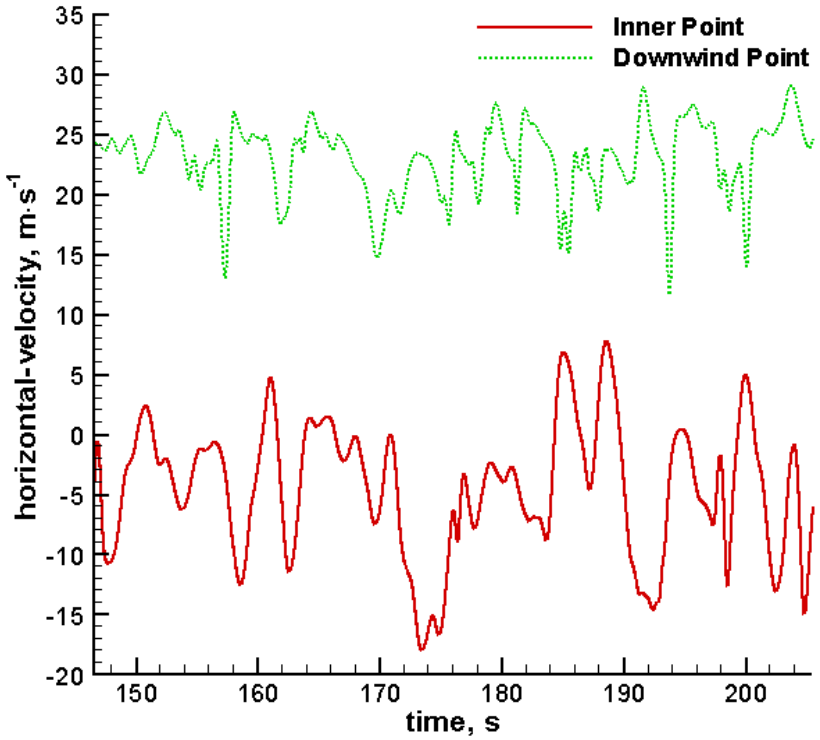

(e) Horizontal-velocity time-history for the inner and downwind points, R_i=17.706 m^{-1}

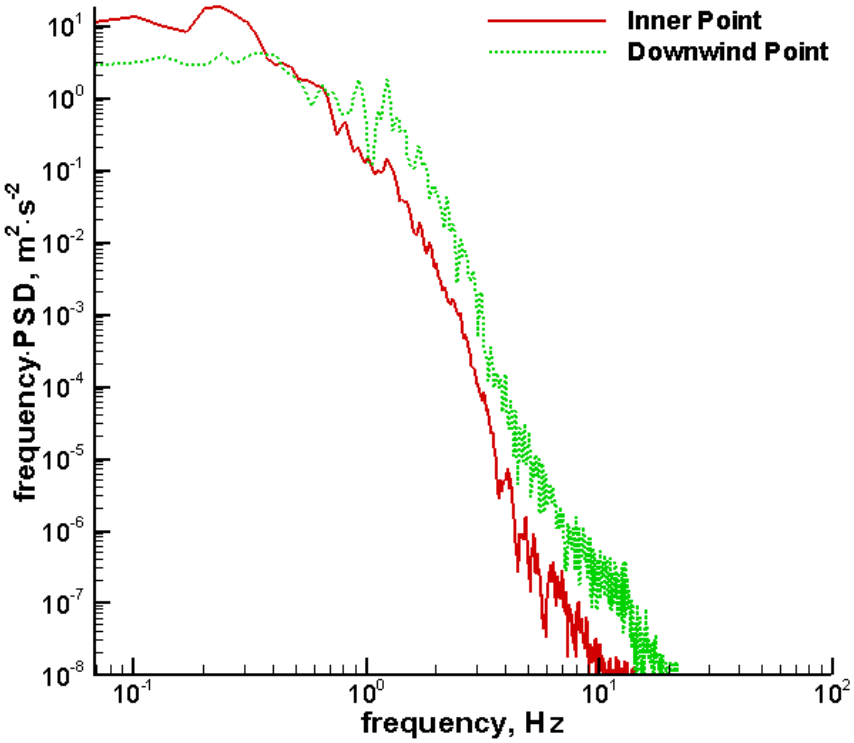

(f) Horizontal-velocity spectra for the inner and downwind points, R_i=17.706 m^{-1}

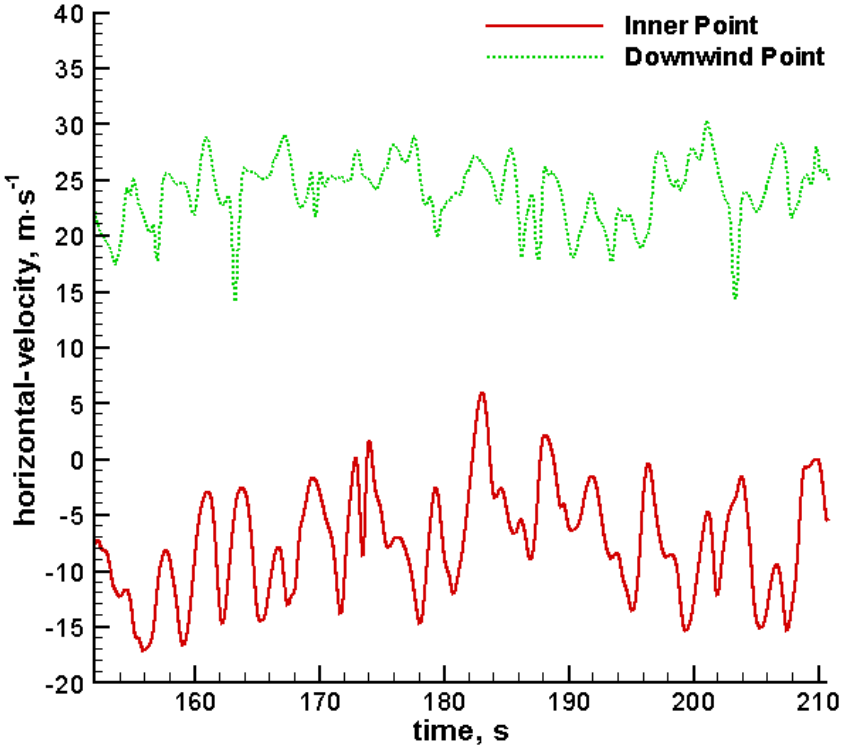

(g) Horizontal-velocity time-history for the inner and downwind points, R_i=3,500 m^{-1}

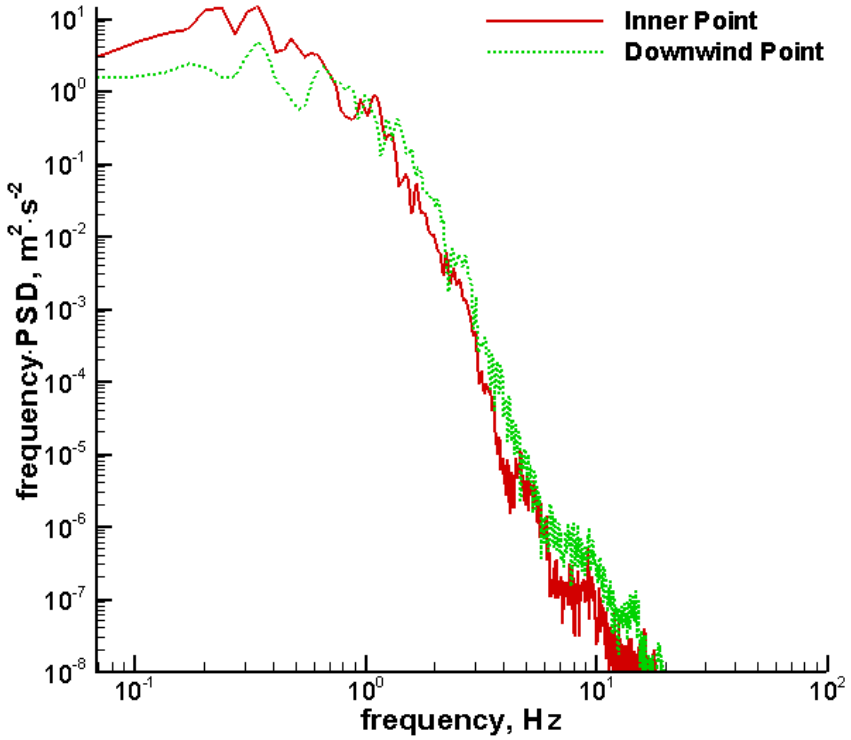

(h) Horizontal-velocity spectra for the inner and downwind points, R_i=3,500 m^{-1}

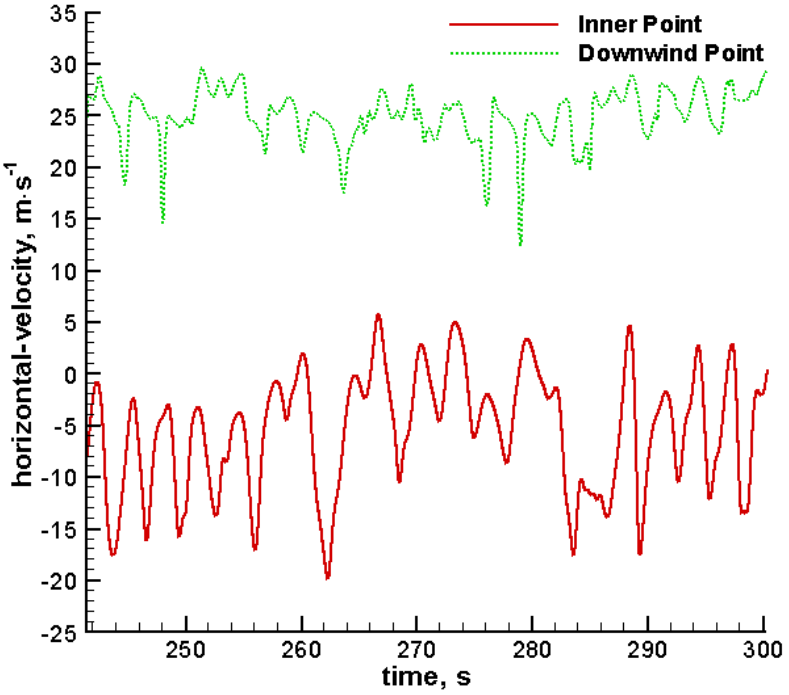

(i) Horizontal-velocity time-history for the inner and downwind points, solid tree

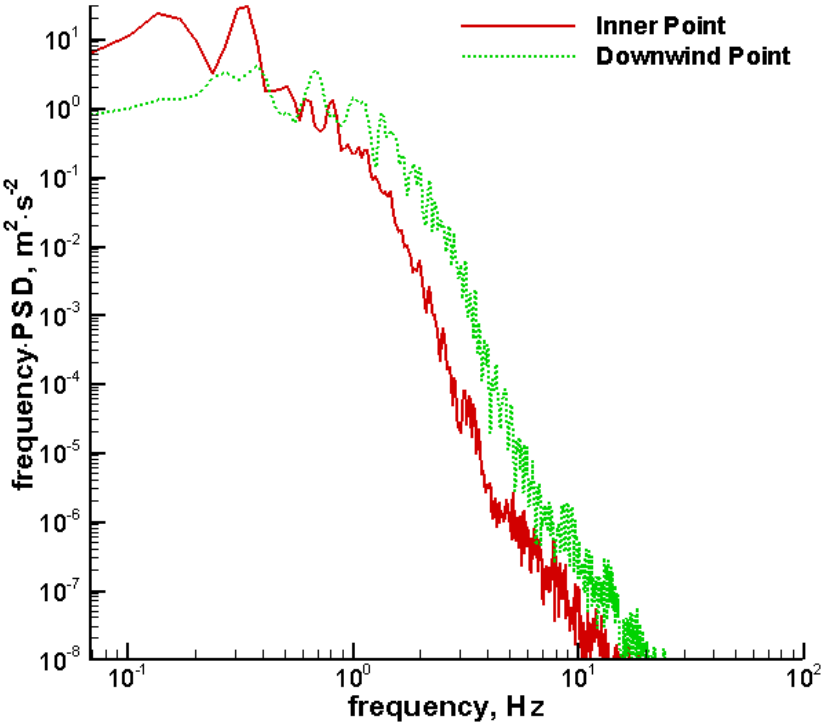

(j) Horizontal-velocity spectra for the inner and downwind points, solid tree

Figure 2.12 Horizontal-velocity time-history and FFT data for trees of different R_i

For the case without a tree, from the inner to the downwind point, f_c shifts to a lower frequency on the horizontal-velocity data, from 0.339 Hz to 0.271 Hz as shown in Fig. 2.12(b). The frequency·PSD curve of the horizontal-velocity at the inner point is higher than that of the downwind point between 0.07 Hz to 0.5 Hz, and the curve at the inner point is almost equivalent to that of the downwind point beyond 0.5 Hz.

In the simulation with a tree of an exceptionally low inertial resistance of $R_i=1\bullet10^{-9}$ m^{-1}, from the inner to the downwind point, f_c shifts to a lower frequency on the horizontal-velocity data, from 0.373 Hz to 0.170 Hz similarly as the case without a tree, as shown in Fig. 2.12(d). The frequency·PSD curve of the horizontal-velocity at the inner point is higher than that of the downwind point between 0.07 Hz to 0.5 Hz, and the curve at the inner point is nearly identical to that of the downwind point beyond 0.5 Hz as in the case without the tree. The similarity in the frequency values and the decreasing shift in frequency not shown in the other cases validate that a tree with an extremely low inertial resistance is comparable to a case without a tree.

A tree with a moderately low value of $R_i=17.706$ m^{-1} is simulated, a value calculated by multiplying the packing density and the cross-sectional area of the model tree crown then dividing the product by the wood-wool mass, to simulate the wood-wool model by Gromke and Ruck (2008). From the inner to the downwind point, f_c maintains the value of 0.237 Hz on the horizontal-velocity data as shown in Fig. 2.12(f). The frequency·PSD curve of the horizontal-velocity at the inner point is higher than that of the downwind point between 0.07 Hz to 0.4 Hz, but the curve for the inner point is lower than that of the downwind point beyond 0.4 Hz.

The next simulation involves a tree with a high inertial resistance of $R_i=3{,}500$ m^{-1}. From the inner to the downwind point, f_c shifts to a higher frequency on the horizontal-velocity data, from 0.237 Hz to 0.644 Hz as shown in Fig. 2.12(h). The frequency·PSD curve of the horizontal-velocity at the inner point is higher than that of the downwind point between 0.07 Hz to 0.7 Hz, and the curves for both points are approximately equal beyond 0.7 Hz.

The next case is the solid tree. From the inner to the downwind point, f_c shifts to a higher frequency on the horizontal-velocity data, from 0.170 Hz to 0.475 Hz as shown in Fig. 2.12(j), similar to the case with a tree of $R_i=3{,}500$ m^{-1}. The frequency·PSD curve of the horizontal-velocity at the inner point is higher than that of the downwind point between 0.07 Hz to 0.7 Hz, and the curves for both points are approximately equal beyond 0.7 Hz. Even though the f_c values for the solid tree and the case with $R_i=3{,}500$ m^{-1} do not match exactly, there is a unique

characteristic between the inner and downwind point. The f_c at the downwind point is a factor of about 2.7 of the inner point for both the solid tree and the case with R_i=3,500 m^{-1}, which is not seen in the porous tree cases. This similarity reiterates the validity of changing the inertial resistance parameter for the tree crown using CFD.

The time-history and spectral data for the turbulent kinetic energy at the inner and downwind points for different inertial resistance values for the tree are shown in Fig. 2.13.

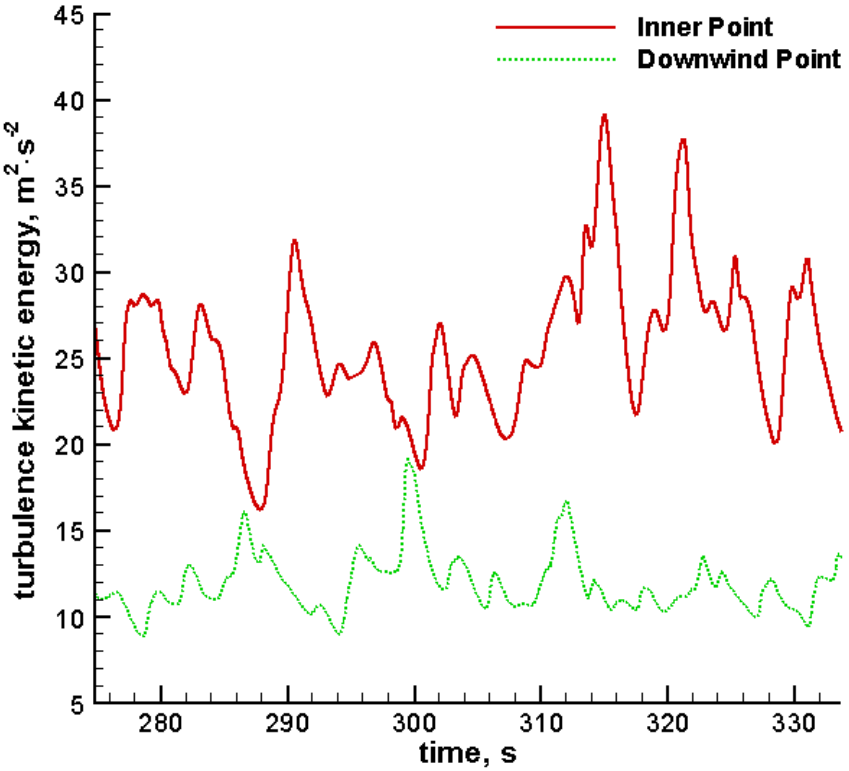

(a) Turbulent kinetic energy time-history for the inner and downwind points, no tree

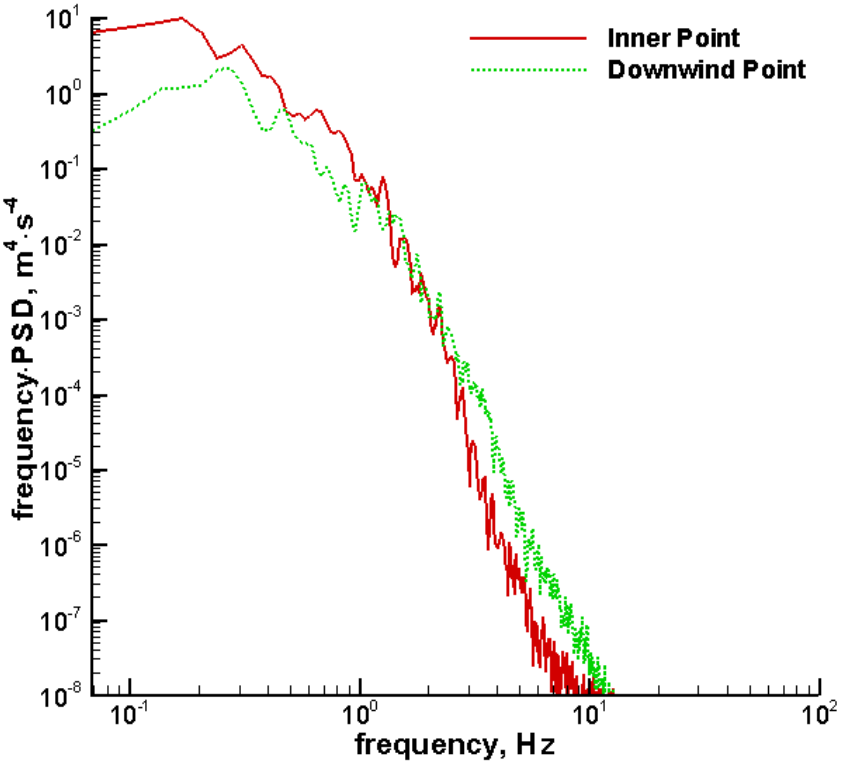

(b) Turbulent kinetic energy spectra for the inner and downwind points, no tree

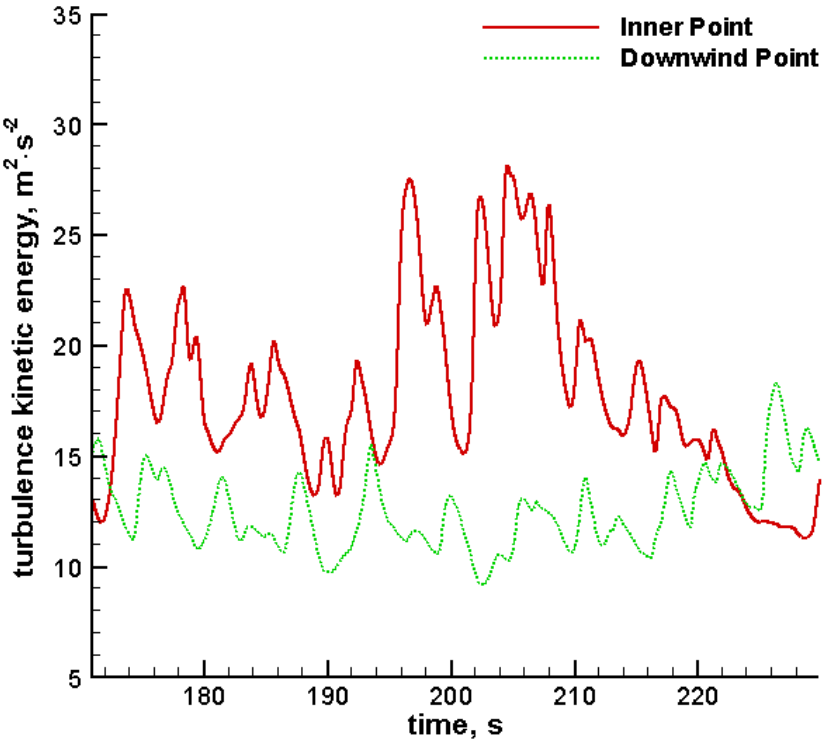

(c) Turbulent kinetic energy time-history for the inner and downwind points, $R_i=1\bullet10^{-9}$ m^{-1}

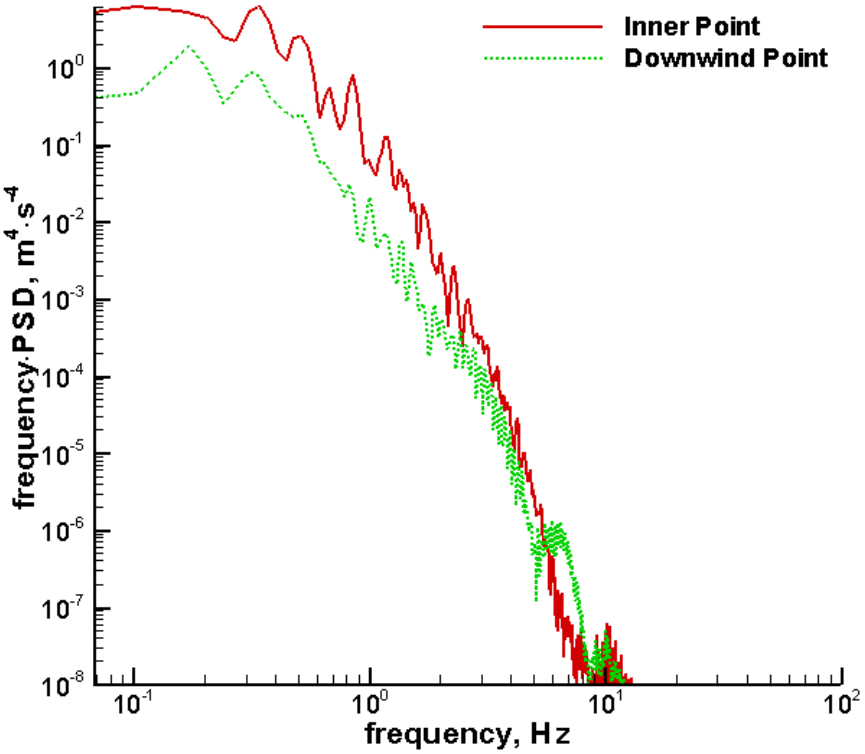

(d) Turbulent kinetic energy spectra for the inner and downwind points, R_i=1•10^{-9} m^{-1}

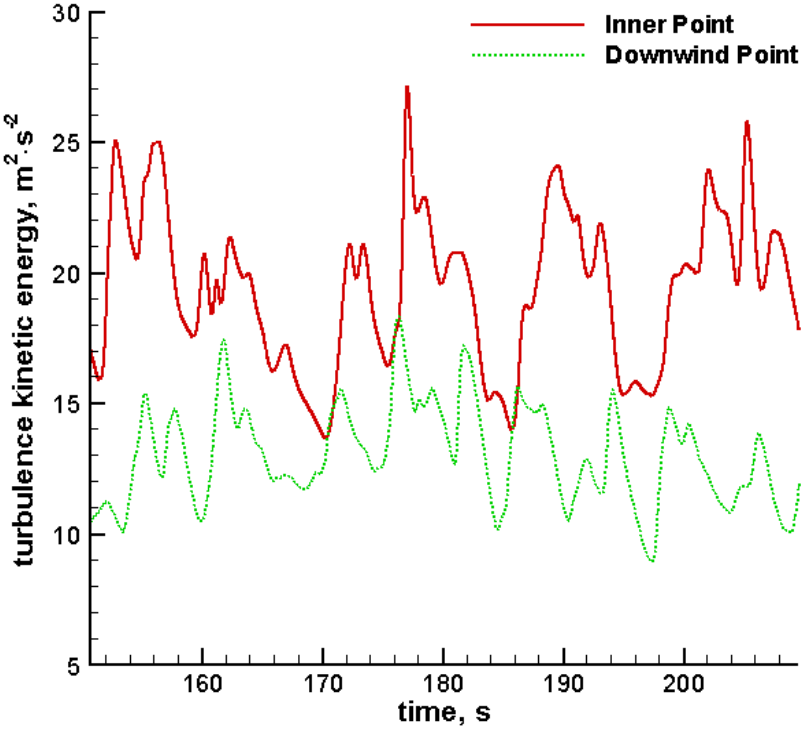

(e) Turbulent kinetic energy time-history for the inner and downwind points, R_i=17.706 m^{-1}

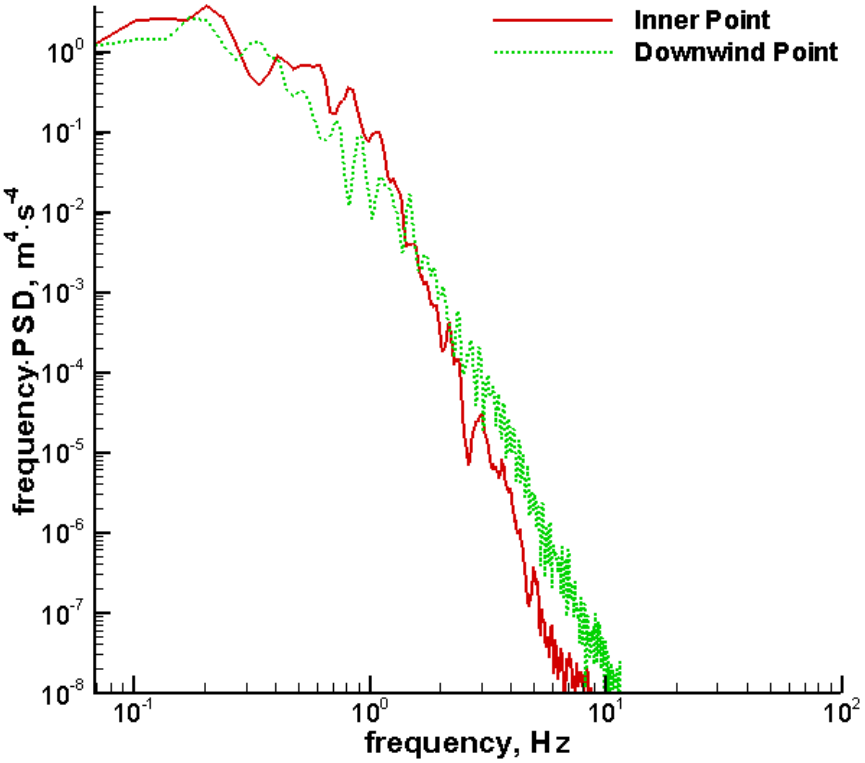

(f) Turbulent kinetic energy spectra for the inner and downwind points, R_i=17.706 m^{-1}

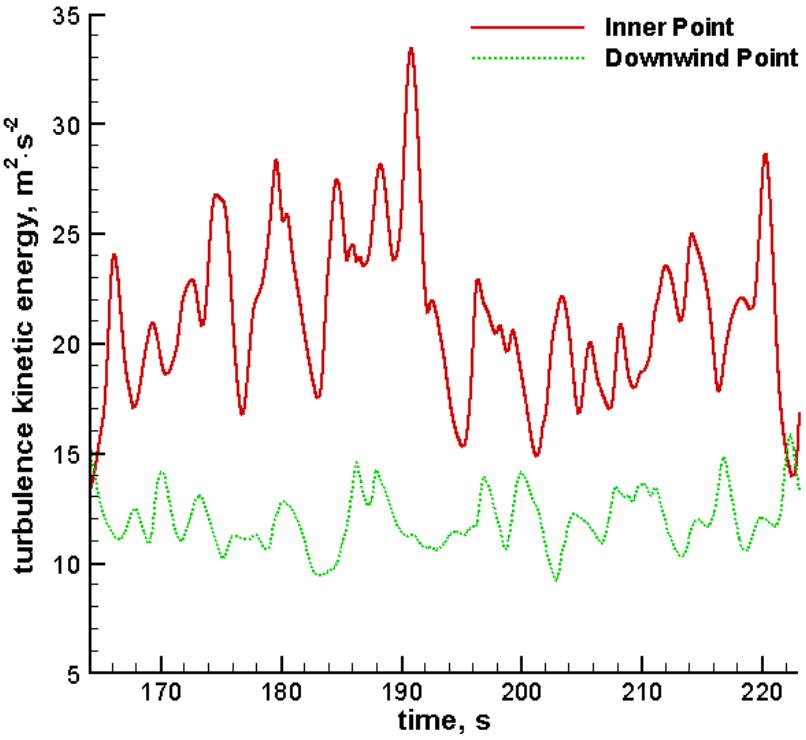

(g) Turbulent kinetic energy time-history for the inner and downwind points, R_i=3,500 m^{-1}

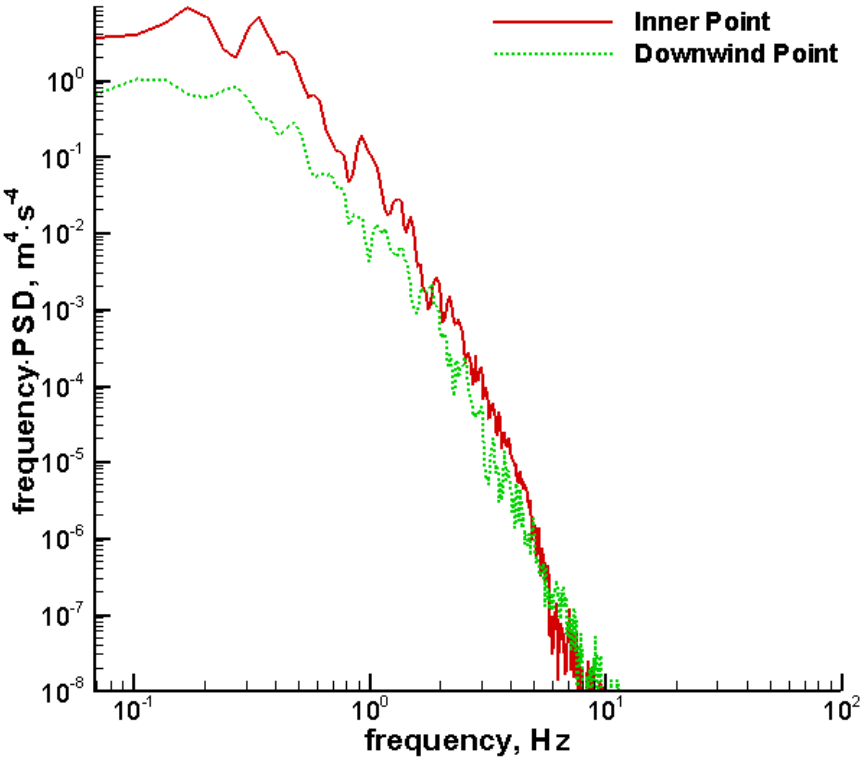

(h) Turbulent kinetic energy spectra for the inner and downwind points, R_i=3,500 m^{-1}

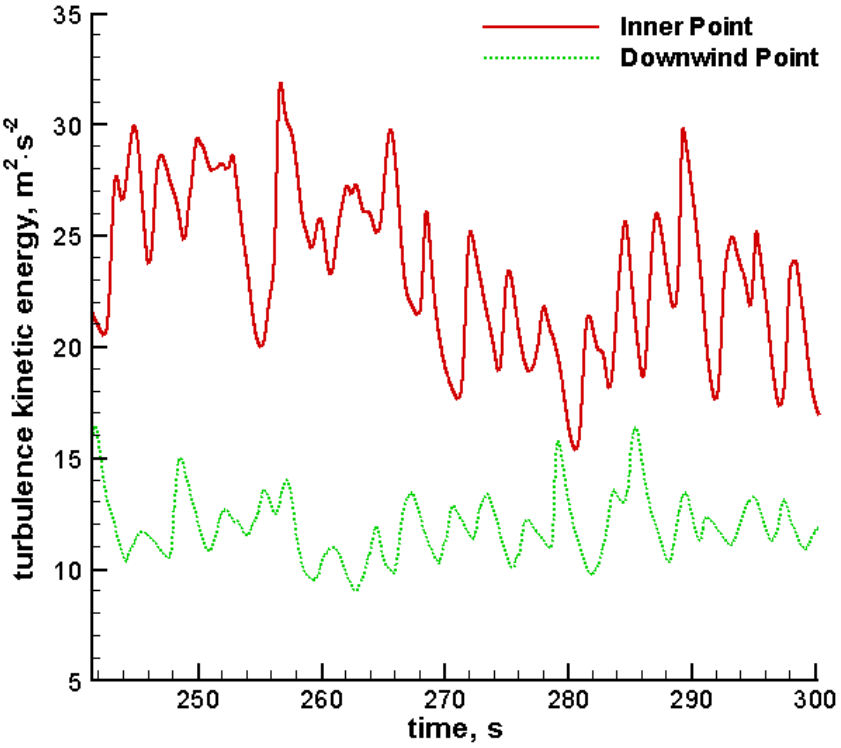

(i) Turbulent kinetic energy time-history for the inner and downwind points, solid tree

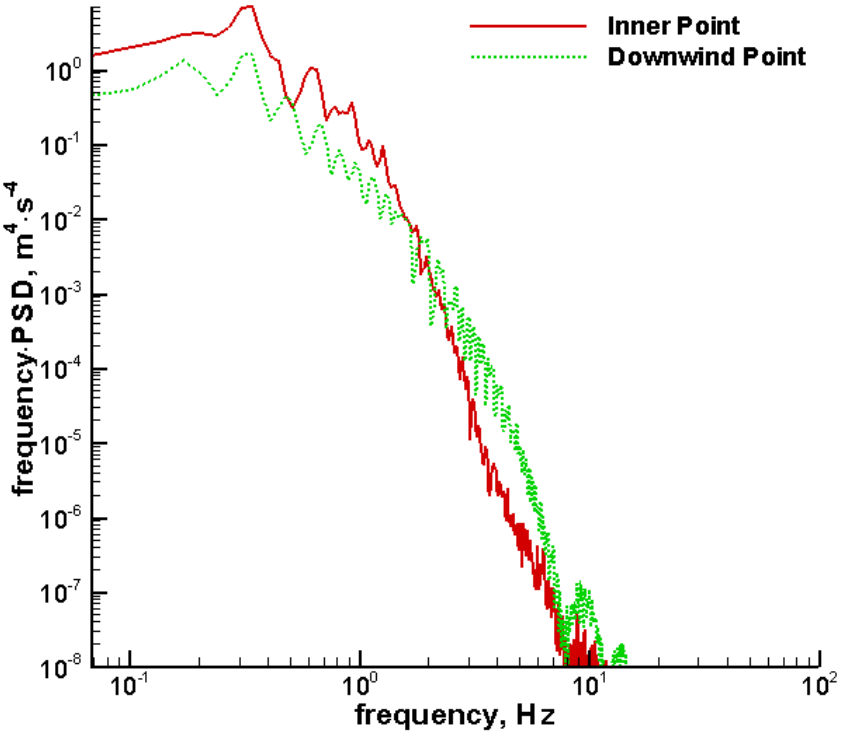

(j) Turbulent kinetic energy spectra for the inner and downwind points, solid tree

Figure 2.13 Turbulent kinetic energy time-history and FFT data for trees of different R_i

For the case without a tree, from the inner to the downwind point, f_c shifts to a higher frequency on the turbulent kinetic energy data, from 0.170 Hz to 0.271Hz as shown in Fig. 2.13(b). The frequency·PSD curve of the turbulent kinetic energy at the inner point is higher than that of the downwind point between 0.07 Hz to 1.5 Hz, and the curves for both points are approximately equal beyond 1.5 Hz.

In the simulation with a tree of an exceptionally low inertial resistance of $R_i=1\bullet10^{-9}$ m^{-1}, from the inner to the downwind point, f_c shifts to a higher frequency on the turbulent kinetic energy data, from 0.102 Hz to 0.203 Hz similarly as the case without a tree, as shown in Fig. 2.13(d). The frequency·PSD curve of the turbulent kinetic energy at the inner point is higher than that of the downwind point between 0.07 Hz to 1.5 Hz, and the curve at the inner point is identical to that of the downwind point beyond 1.5 Hz as in the case without the tree. The similarity in the frequency values and the increasing shift in frequency not shown in the other cases validate that a tree with an extremely low inertial resistance is comparable to a case without a tree.

In the simulation with a tree of a wood-wool model inertial resistance of R_i=17.706 m^{-1}, from the inner to the downwind point, f_c shifts to a higher frequency, from 0.203 Hz to 0.339 Hz, on the turbulent kinetic energy data as shown in Fig. 2.13(f). The curves of the turbulent kinetic energy at the inner and downwind points are approximately the same at all calculated frequencies.

The next simulation involves a tree with a high inertial resistance of R_i=3,500 m^{-1}. From the inner to the downwind point, f_c shifts to a lower frequency on the turbulent kinetic energy data, from 0.339 Hz to 0.102 Hz as shown in Fig. 2.13(h). The frequency·PSD curve of the turbulent kinetic energy at the inner point is higher than that of the downwind point between 0.07 Hz to 2.0 Hz, and the curves for both points are approximately equal beyond 2.0 Hz.

The next case is the solid tree. From the inner to the downwind point, f_c shifts to a lower frequency on the turbulent kinetic energy data, from 0.339 Hz to 0.170 Hz as shown in Fig. 2.13(j), similar to the case with a tree of R_i=3,500 m^{-1}. The frequency·PSD curve of the turbulent kinetic energy at the inner point is higher than that of the downwind point between 0.07 Hz to 2.0 Hz, and the curves for both points are approximately equal beyond 2.0 Hz, similarly as with the case with a tree of R_i=3,500 m^{-1}. Even though the f_c values for the solid tree and the case with R_i=3,500 m^{-1} do not match exactly, there is a unique characteristic between the inner and downwind point. The f_c at the inner point is a factor of about three times the downwind point for both the solid tree and the case with R_i=3,500 m^{-1}, which is not seen in the porous tree cases. This similarity reiterates the validity of changing the inertial resistance parameter for the tree crown using CFD.

To separately show the similarity and validity of setting R_i to modify the tree properties on the low inertial resistance end, the spectral analyses on the horizontal-velocity and turbulent kinetic energy at the inner and downwind points for the cases without a tree, with R_i=1•10^{-9} m^{-1}, and with R_i=17.706 m^{-1}, are shown in Fig. 2.14. Based on the spectral analyses on the three cases on the low inertial resistance end, each f_c and frequency•PSD curve is identical for each of these cases, justifying the validity of changing the inertial resistance parameter for the tree crown.

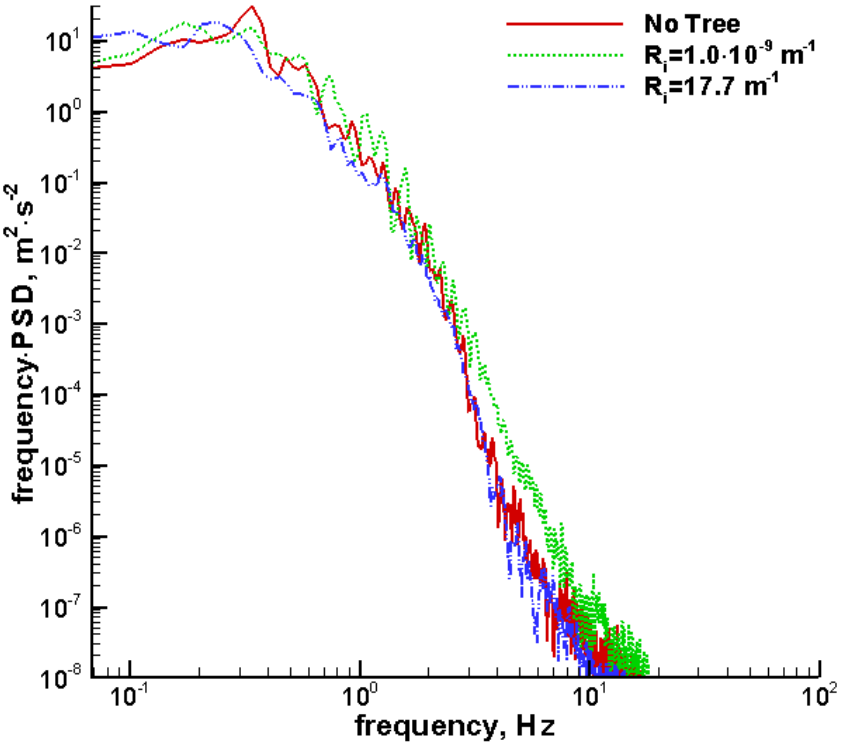

(a) Horizontal-velocity spectra at the inner point

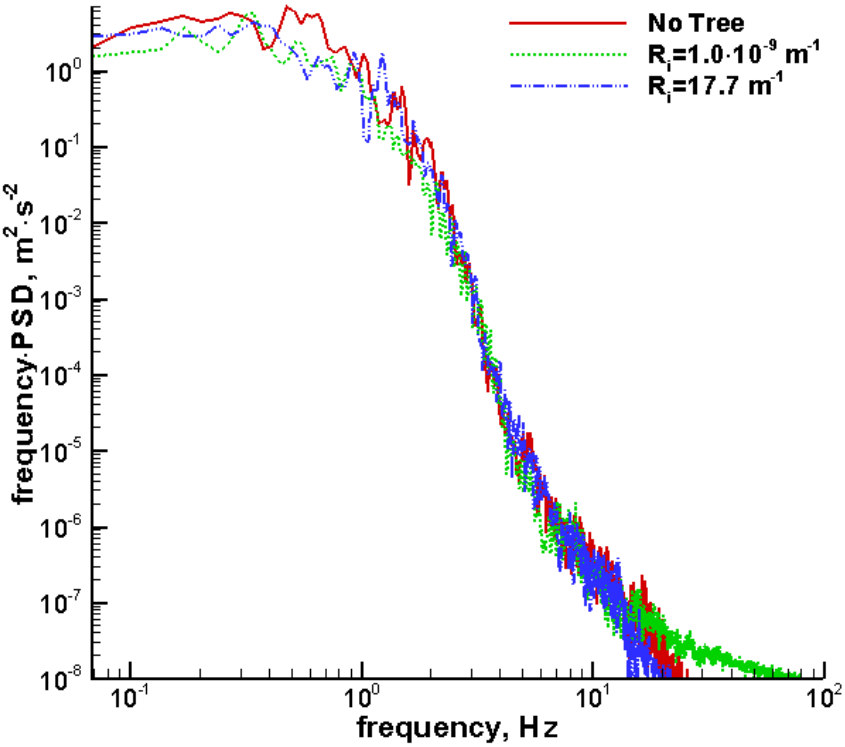

(b) Horizontal-velocity spectra at the downwind point

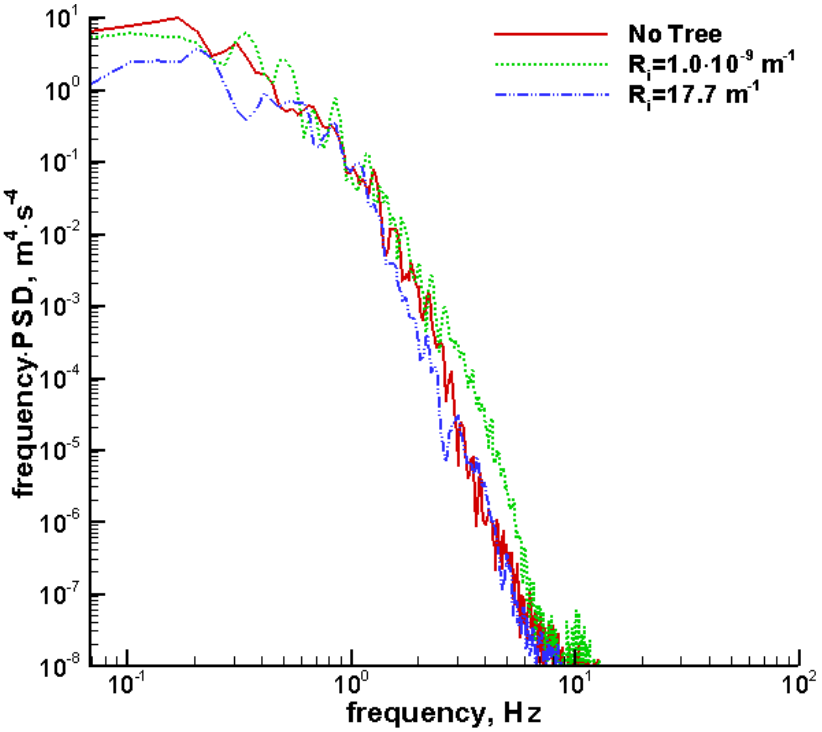

(c) Turbulent kinetic energy spectra at the inner point

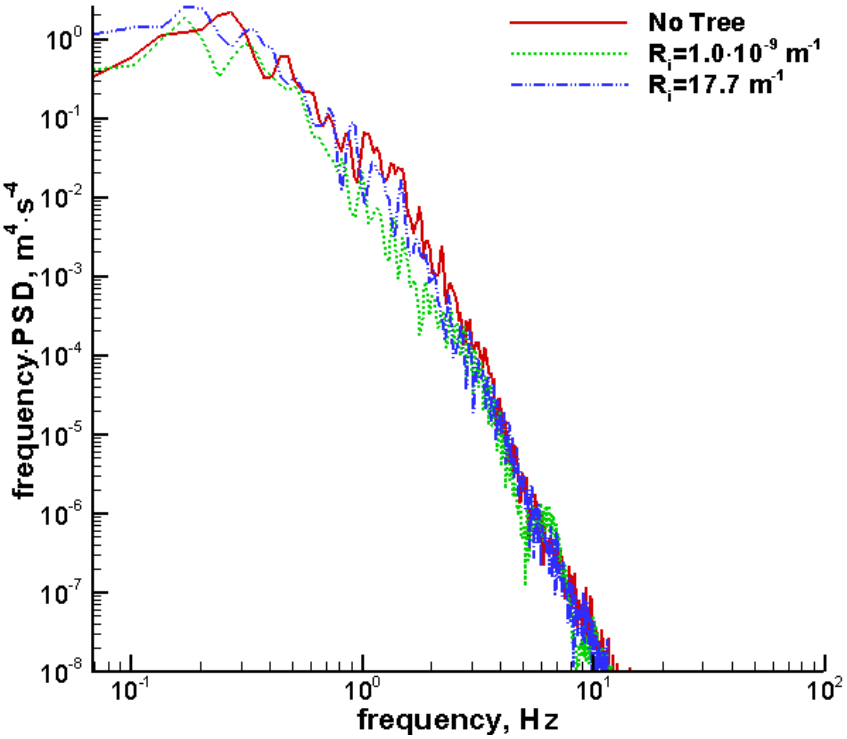

(d) Turbulent kinetic energy spectra at the downwind point

Figure 2.14 Collective spectra, low R_i cases

To separately show the similarity and validity of setting R_i to modify the tree on the high inertial resistance end, the spectral analyses on the horizontal-velocity and turbulent kinetic energy at the inner and downwind points for the cases with a solid-wall tree and with R_i=3,500 m^{-1} are shown in Fig. 2.15. Based on the spectral analyses on the three cases on the high inertial resistance end, each f_c and frequency•PSD curve is identical for each of these cases. Even though the f_c values for the solid tree and the case with R_i=3,500 m^{-1} do not match exactly, these cases show a unique characteristic between the inner and downwind point where the prominent prevailing frequency shifts largely at a factor of about three, not seen in the porous tree cases. This similarity reiterates the validity of changing the inertial resistance parameter for the tree crown using CFD.

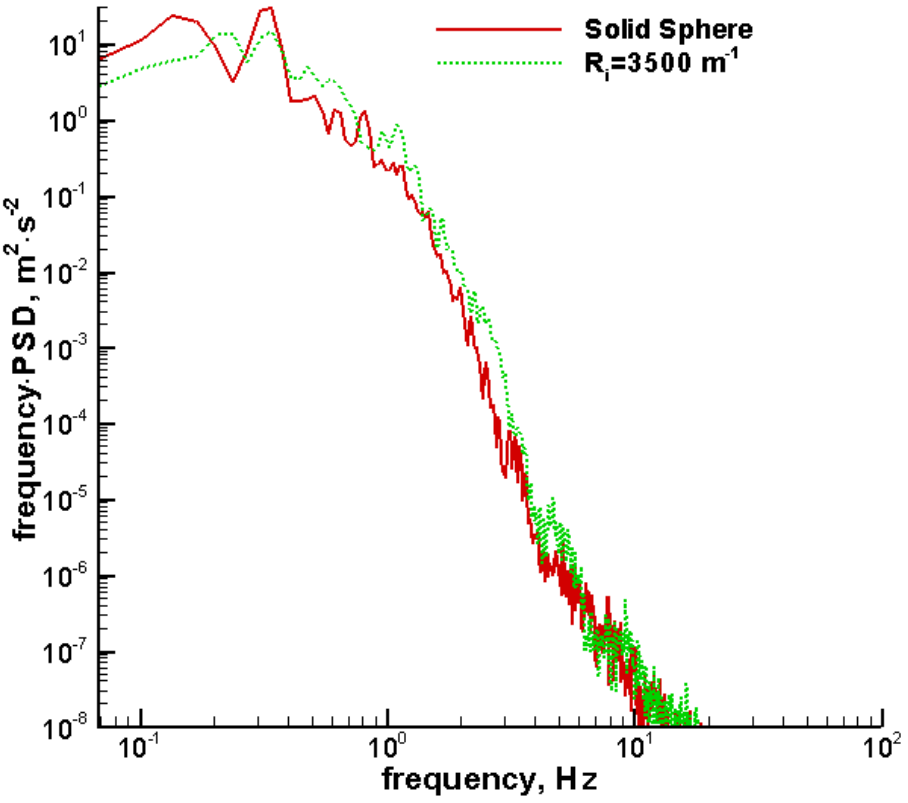

(a) Horizontal-velocity spectra at the inner point

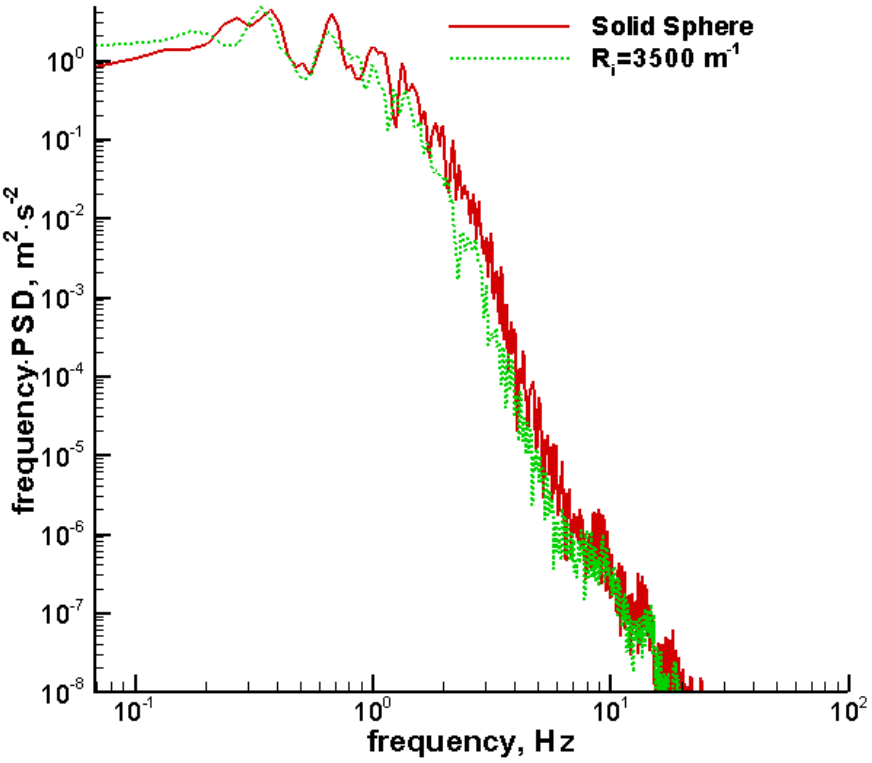

(b) Horizontal-velocity spectra at the downwind point

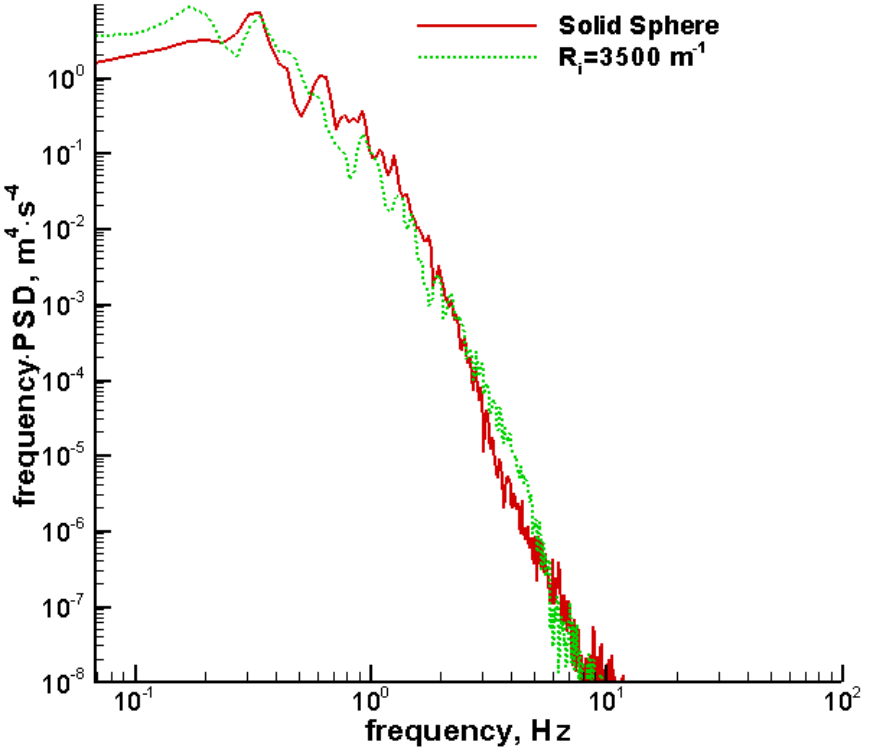

(c) Turbulent kinetic energy spectra at the inner point

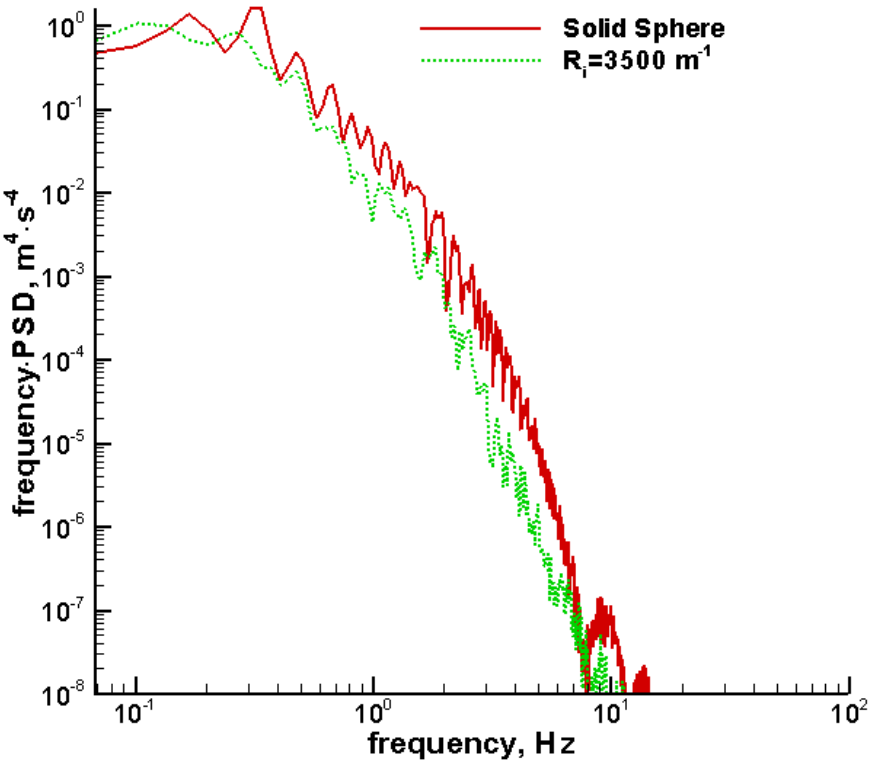

(d) Turbulent kinetic energy spectra at the downwind point

Figure 2.15 Collective spectra, high R_i cases

The cases with different inertial resistances are then compared. The spectral analysis on the horizontal-velocity at the inner point shown in Fig. 2.16(a) shows that f_c decreases with an increase in R_i. Extending the simulation time and taking a larger amount of samples would provide an even smoother resolution at the lower frequencies (Stull, 1988). The spectral analyses on the horizontal-velocity at the downwind point shown in Fig. 2.16(b) shows that f_c increases with an increase in R_i. The spectral analysis on the turbulent kinetic energy at the inner point shows that f_c increases with an increase in R_i, as shown in Fig. 2.16(c). The spectral analysis on the turbulent kinetic energy at the downwind point does not show a discrete correlation between f_c and varying R_i. The spectral analyses on the different R_i do not show a clear trend related to the frequency·PSD curve within the calculated spectral data frequency range.

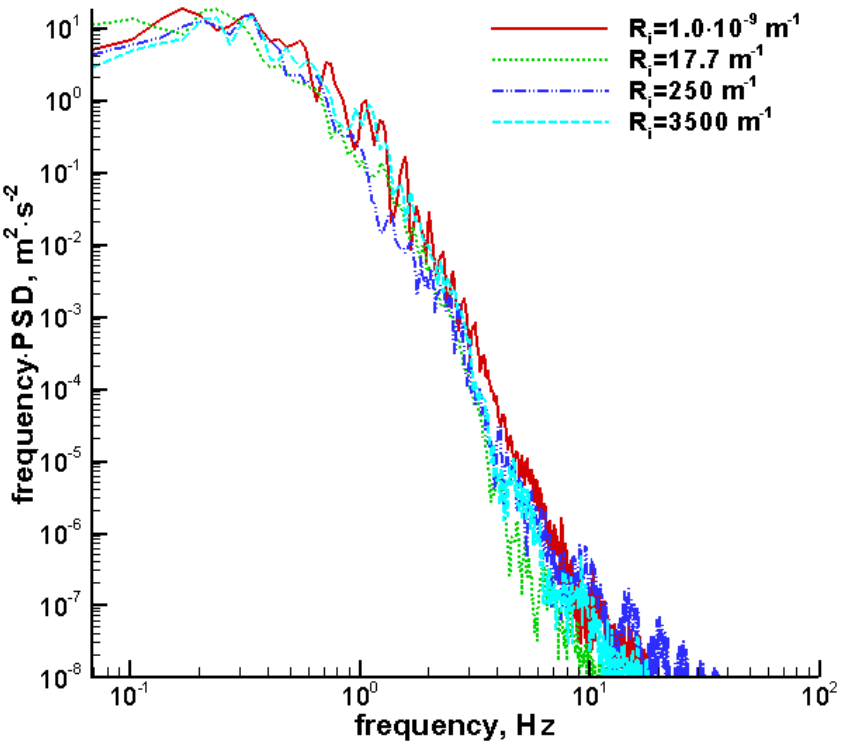

(a) Horizontal-velocity spectra at inner point

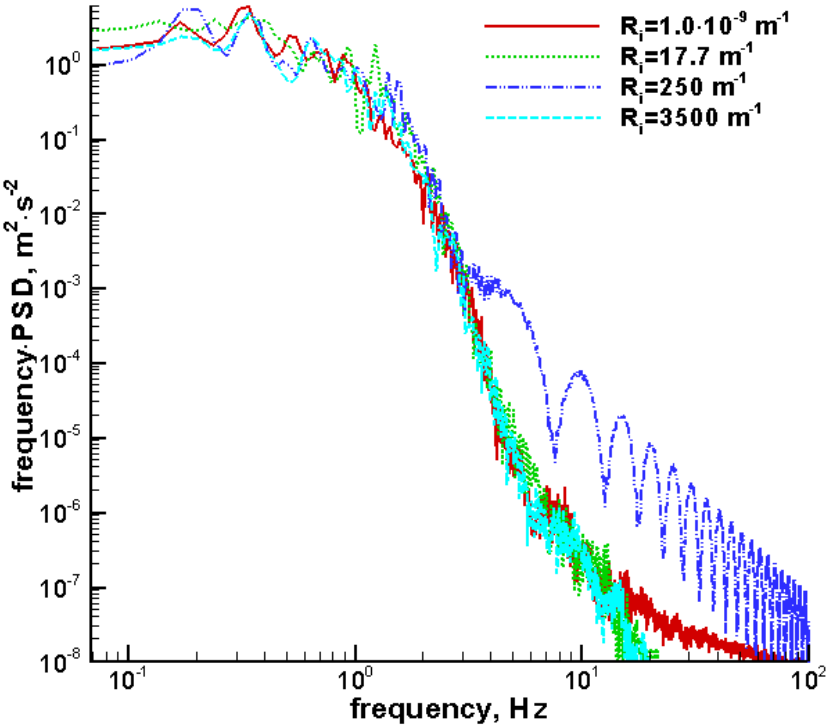

(b) Horizontal-velocity spectra at downwind point

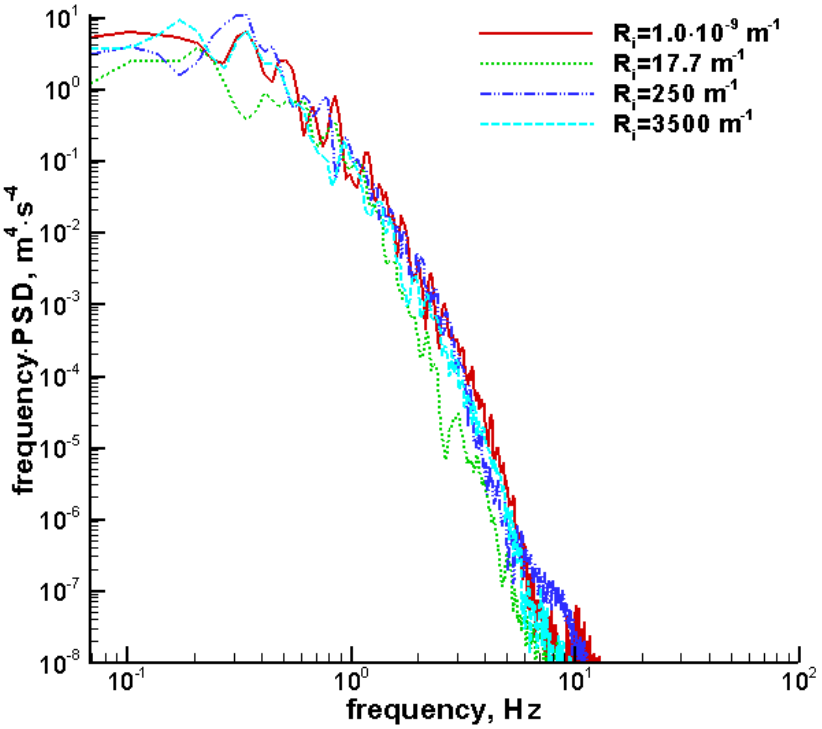

(c) Turbulent kinetic energy spectra at inner point

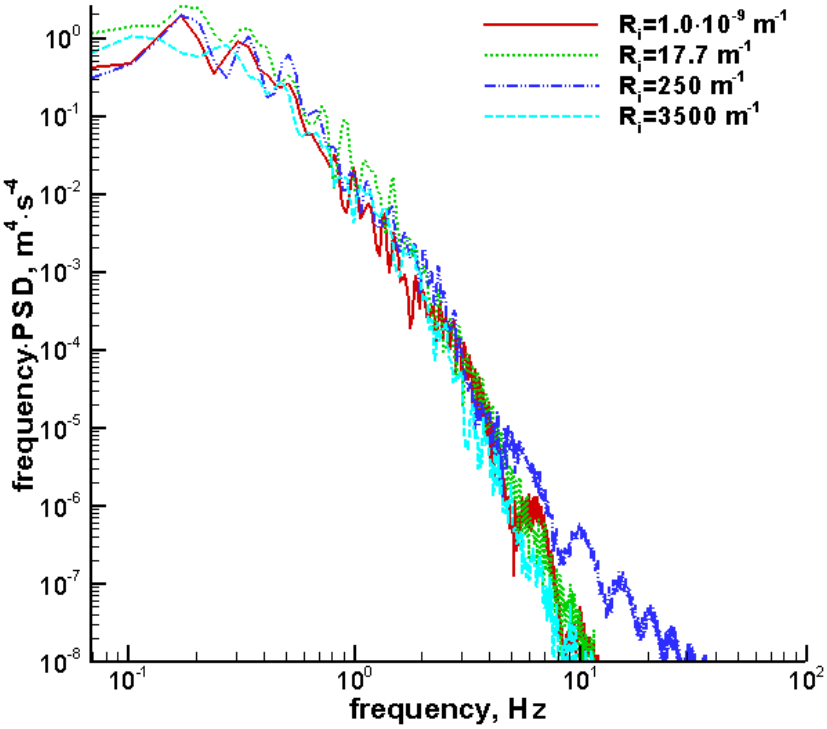

(d) Turbulent kinetic energy spectra at downwind point

Figure 2.16 Collective spectra, different R_i cases

2.4 Summary

The simulation of actual trees has been validated by comparing different CFD simulations to porous media wind tunnel tests. To suggest feasible conditions for the siting of a wind turbine in urban environments, the velocity and turbulence contours of a building and tree are generated. Since the contours show only a snapshot of the flow at an instant in time, spectral analyses are conducted. The spectral calculations show that the Strouhal number and frequency·PSD curve vary with different solid structures obstructing the fluid flow towards a porous medium.

To summarize the differences in the spectral analyses between each of the simulations, a table of Strouhal numbers is created. Table 2.3 shows a summary of the values of the calculated Strouhal numbers for each of the building and tree simulations.

Table 2.3 Summary of Strouhal numbers for different simulations

Building Height (m)	Tree R_i (m^{-1})	Strouhal Number, $St = f_c \cdot w \cdot U_o^{-1}$ (-)			
		Turbulent Kinetic Energy Spectra		Horizontal-Velocity Spectra	
		Inner Point	Downwind Point	Inner Point	Downwind Point
8	250	0.036	0.027	0.081	0.045
11	No Tree	0.045	0.072	0.090	0.72
11	$1 \cdot 10^{-9}$	0.027	0.054	0.099	0.045
11	17.706	0.054	0.090	0.063	0.063
11	250	0.081	0.045	0.054	0.090
11	3500	0.090	0.027	0.063	0.172
11	Solid Tree	0.090	0.045	0.036	0.181
11	250, Moved Downwind	0.045	0.045	0.045	0.127
14	250	0.090	0.172	0.036	0.099

The Strouhal numbers directly correspond to f_c, as shown in Eq. (2.15). The range of Strouhal numbers calculated from the simulations of this investigation are also supported by the tabulated data accumulated by Sarioglu and Yavuz (2002) for rectangular cylinders. In the cases where the Strouhal number is not visibly distinctive in the spectrum plots, the videos of the flow field were analyzed to calculate the time spans between vortex shedding at the inner and downwind points, then used to verify the prominent prevailing frequency and the Strouhal number provided in the FFT calculations. The broad range of frequency peaks in the spectra is related to the broad spectrum of turbulence and levels of vortex shedding in the flow fields.

To generalize the trends, a summary is shown with directional arrows corresponding with shifts in the Strouhal number in Table 2.4(a), as different variables are changed in the simulations. Similarly, Table 2.4(b) shows shifts in the frequency·PSD curve along the horizontal frequency axis.

Table 2.4 Summary of horizontal-axis frequency shift directions for different simulations

Variable	Variable Change	Strouhal Number (St) Frequency Shift			
		Turbulent Kinetic Energy		Horizontal-Velocity	
		Inner Point	Downwind Point	Inner Point	Downwind Point
Building Height	↑	↑	↑	↓	↑
	↓	↓	↓	↑	↓
Tree R_i	↑	↑	no trend	no trend	↑
	↓	↓	no trend	no trend	↓
Tree Moved Downwind	↑	↓	no change	↓	↑
	↓	↑	no change	↑	↓

(a) Summary of Strouhal number frequency shift directions

Variable	Variable Change	Shift in Spectrum Magnitude Curve (frequency·PSD) along Horizontal Frequency Axis			
		Turbulent Kinetic Energy		Horizontal-Velocity	
		Inner Point	Downwind Point	Inner Point	Downwind Point
Building Height	↑	↑	↑	↑	↑
	↓	↓	↓	↓	↓
Tree R_i	↑	no trend	no trend	no trend	↑
	↓	no trend	no trend	no trend	↓
Tree Moved Downwind	↑	↑	↓	↑	↓
	↓	↓	↑	↓	↑

(b) Summary of frequency·PSD curve frequency shift directions

The change in building height directly corresponds to the changes in the Strouhal number and the frequency·PSD curve as demonstrated by Sakamoto and Arie (1983). The simulations generated in this investigation show that changing R_i only shows a general trend where increasing the inertial resistance of a tree directly corresponds to an increase in the Strouhal number and the frequency·PSD curve shift with increasing frequency for the turbulent kinetic energy and horizontal-velocity at the downwind point. Moving the tree further downwind and calculating the Strouhal number and frequency·PSD at the inner and downwind points relative to the tree shows varied results, where the Strouhal number at the inner point varies inversely with the change in tree distance, but the frequency·PSD curve varies directly with the change in tree distance. Also, the Strouhal number at the downwind point varies directly with the increase in tree distance, but the frequency·PSD curve varies inversely with the increase in tree distance.

The turbulence effects between and downwind from buildings and trees show that flow circulation occurs at different rates depending on the height of a building and the wind resistance of a tree. For the optimal siting of a small-scale wind turbine, the trends from this research can be used to determine the feasibility of the wind turbine at a given urban site, and a specific wind turbine model can be chosen based on the suitability of its design given a specific location in an

urban environment. This research aims to serve as a foundation for future applications, such as the statistical analyses for varying municipal and rural landscapes that include trees, towards improving small-scale wind turbine siting in an urban environment.

The turbulence effects between and downwind from buildings and trees show that flow circulation occurs at different rates depending on the height of a building and the wind resistance of a tree. For the optimal siting of a small-scale wind turbine, the trends from this research can be used to determine the feasibility of the wind turbine at a given urban site, and a specific wind turbine model can be chosen based on the suitability of its design given a specific location in an urban environment. This research aims to serve as a foundation for future applications, such as the statistical analyses for varying municipal and rural landscapes that include trees, towards improving small-scale wind turbine siting in an urban environment.

Chapter 3 - Improved Energy Estimations for a Small-Scale Wind Turbine using Numerical Simulations

3.1 Wind Measurements Methodology

In the third chapter, I will discuss the incorporation of the criteria established for simulating buildings and trees to a simulation of an actual site. The parameters for a specific terrain are discussed, and the simulated wind speeds are compared to actual measurements.

3.1.1 Wind Measurements at the Wind Turbine and Meteorological Tower

Wind speed and direction are measured at a wind turbine near a fire station in a suburban location and at a meteorological tower outside of Manhattan, KS. A picture of the wind turbine site is shown in Fig. 3.1, and a picture of the meteorological tower is shown in Fig. 3.2.

Figure 3.1 Picture of the wind turbine near a fire station in Manhattan, KS

Figure 3.2 Picture of the meteorological tower outside of Manhattan, KS

The wind speed measurements at the wind turbine are at elevations of 7.6 m (25 ft), 15.2 m (50 ft), and 18.3 m (60 ft), where two anemometers measure the wind speed at 7.6 m and at 15.2 m, and the wind speed at 18.3 m is calculated based on the rotational speed of the wind turbine rotor. Wind is also measured at a meteorological tower in an open environment outside the city, at three elevations of 20.7 m (68 ft), 25.9 m (85 ft), and 31.1 m (102 ft). At the wind turbine, the rotor tracks the wind speed at thirty-second intervals and the anemometer measurements are tracked at one-minute intervals. At the meteorological tower, the measurements are tracked at thirty-minute intervals. The average wind speeds from the anemometers on the meteorological tower will be used to build the power-law profile for wind speed in simulating the wind turbine site. The measurements at the wind turbine will then be compared to the simulations to evaluate the accuracy of the wind speed calculations.

Data sets recorded for two days with different wind speed and direction were used in building the power-law profile for wind speed. One of the data sets were recorded on Jan. 30, 2011, since the wind direction was west to east at the wind turbine, representing a condition in which the wind was obstructed by a fire station and some trees upwind from the wind turbine. The other data set was recorded on Feb. 6, 2011, since a south to north wind portrayed a condition in which there were no relevant obstructions upwind of the wind turbine. The range of data between a time of 600 hours and 1800 hours is used, since quasi-steady state wind speed and direction is identified in this time frame, without the speed-up and slow-down effects from diurnal atmospheric stratification (Tieleman, 2008).

Statistical calculations, including the average and deviation, are necessary to calculate the vertical profile of the wind speed. The wind speed average at each elevation is given in Eq. (3.1) as,

$$\overline{U} = \frac{1}{N}\sum_{i=1}^{N} U_i \tag{3.1}$$

where U_i is the wind speed at a time interval and N is the number of samples. The deviation of a sample set due to turbulence within the 12-hour sample window is expressed by calculating the turbulence intensity using Eq. (3.2),

$$I = \frac{\sqrt{\frac{1}{N-1}\sum_{i=1}^{N}(U_i - \overline{U})^2}}{\overline{U}} \tag{3.2}$$

By using these statistical calculations for the measurements, the vertical profile for the wind speed and the deviation due to turbulence can be visualized on a graph.

3.1.2 West to East Wind, the Most Obstructed Path

3.1.2.1 Wind Turbine Measurements

The west to east wind incorporates the most obstructions upwind of the wind turbine, including the fire station and some trees. The wind measurements from the wind turbine on Jan. 30, 2011, are given in Fig. 3.3.

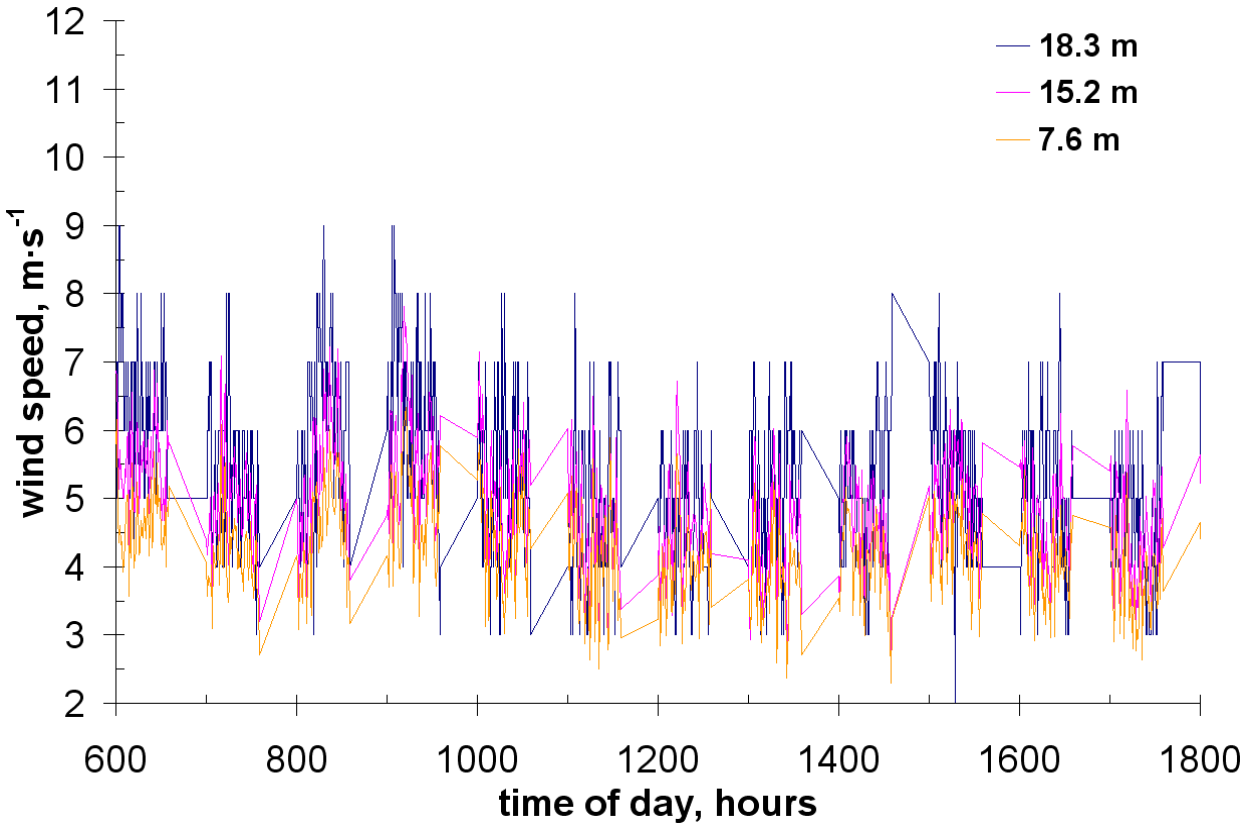

Figure 3.3 The west to east wind speed recorded at the wind turbine on Jan. 30, 2011, at the three elevations

The wind speed averages and deviations measured by the rotor and the anemometers at the wind turbine on Jan. 30, 2011, are given in Table 1. These values will be compared to the simulation of the west to east wind direction.

Table 3.1 Measured averages and deviations at the wind turbine on Jan. 30, 2011

Elevation, m	Average, $m \cdot s^{-1}$	Deviation due to turbulence, $m \cdot s^{-1}$
18.3	5.243	0.668
15.2	4.903	0.885
7.6	4.212	0.709

3.1.2.2 Meteorological Tower Measurements

The wind measurements from the meteorological tower on Jan. 30, 2011, are given in Fig. 3.4.

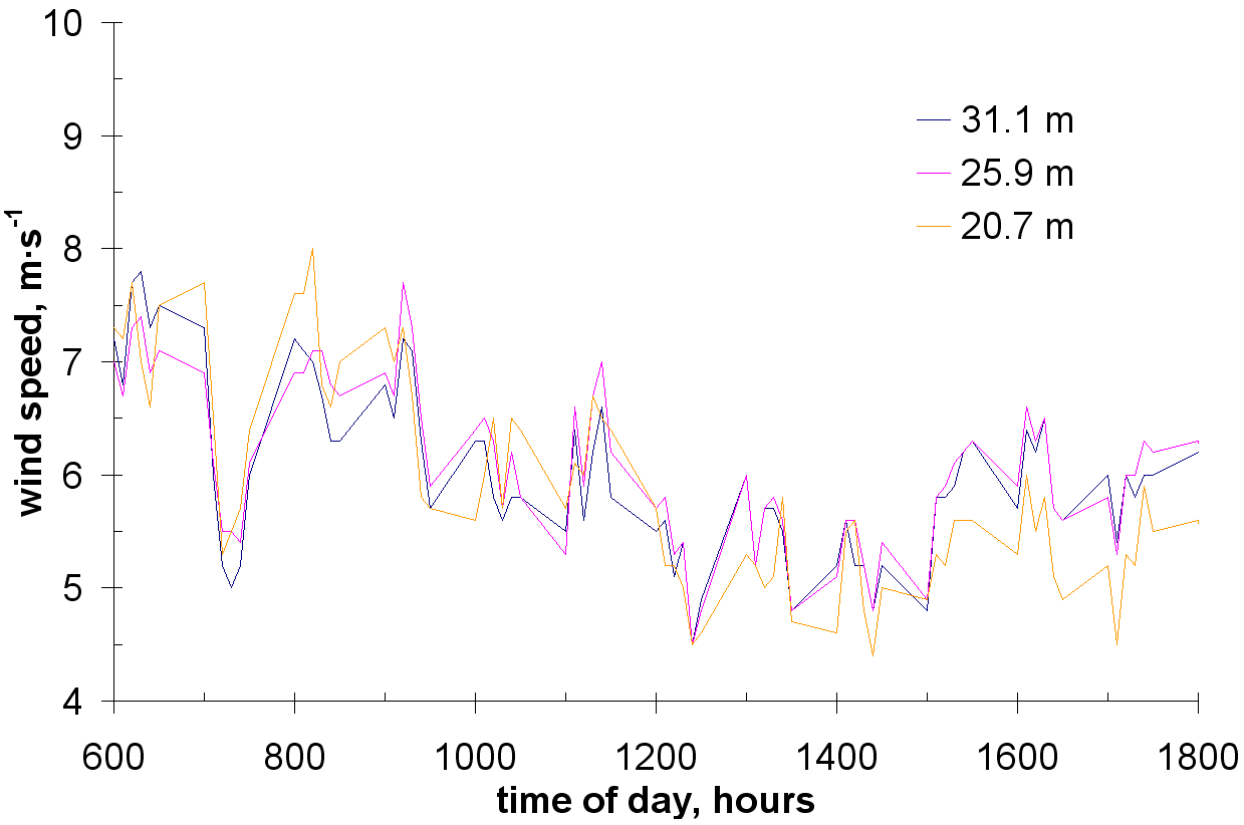

Figure 3.4 West to east wind speeds measured at the meteorological tower on Jan. 30, 2011

Figure 3.4 shows the quasi-steady state nature of the wind speed between a time of 600 hours and 1800 hours. The wind speed averages and deviations for each anemometer at the meteorological tower on Jan. 30, 2011, are given in Table 3.2. The averages will be used towards the generation of the power-law profile for the wind speed by means of a least squares fit.

Table 3.2 Measured averages and deviations at the meteorological tower on Jan. 30, 2011

Elevation, m	Average, $m \cdot s^{-1}$	Deviation due to turbulence, $m \cdot s^{-1}$
31.1	6.001	0.753
25.9	6.093	0.715
20.7	5.910	0.918

3.1.3 South to North Wind, the Least Obstructed Path

3.1.3.1 Wind Turbine Measurements

The south to north wind incorporates the least obstructions upwind of the wind turbine. The wind measurements from the wind turbine on Feb. 6, 2011, are given in Fig. 3.5.

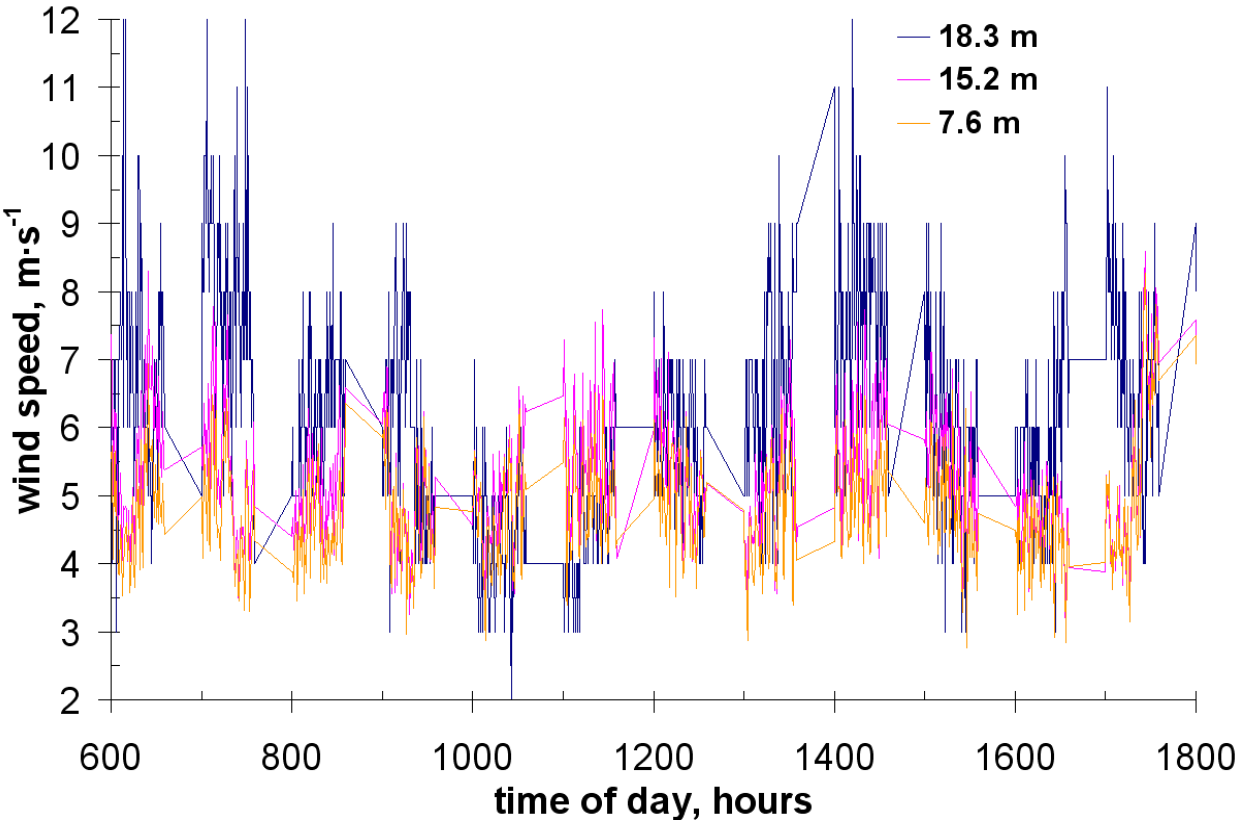

Figure 3.5 The south to north wind speed recorded at the wind turbine on Feb. 6, 2011, for each elevation

The wind speed averages and deviations measured by the rotor and the anemometers at the wind turbine on Feb. 6, 2011, are given in Table 3.3. These values will be compared to the simulation of the south to north wind direction.

Table 3.3 Measured averages and deviations at the wind turbine on Feb. 6, 2011

Elevation, m	Average, $m \cdot s^{-1}$	Deviation due to turbulence,

		$m \cdot s^{-1}$
18.3	6.104	1.232
15.2	5.652	0.996
7.6	4.813	0.843

3.1.3.2 Meteorological Tower Measurements

The wind measurements from the meteorological tower on Feb. 6, 2011, are given in Fig. 3.6.

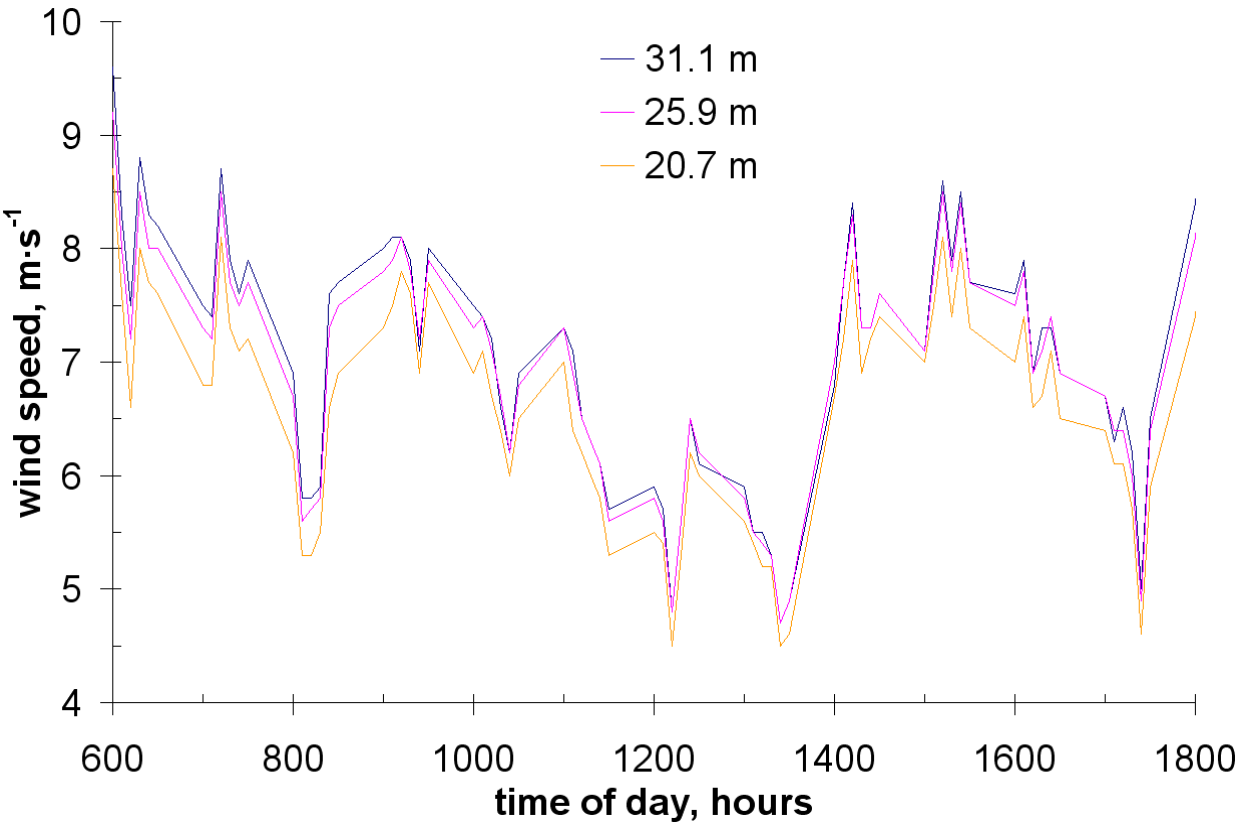

Figure 3.6 South to north wind speeds measured at the meteorological tower on Feb. 6, 2011

Again, the quasi-steady state nature of the wind speed is observed between a time of 600 hours and 1800 hours. The wind speed averages and deviations for each anemometer at the meteorological tower on Feb. 6, 2011, are given in Table 3.4.

Table 3.4 Measured averages and deviations at the meteorological tower on Feb. 6, 2011

Elevation, m	Average, $m \cdot s^{-1}$	Deviation due to turbulence, $m \cdot s^{-1}$
31.1	7.044	1.081
25.9	6.951	1.030
20.7	6.601	0.977

3.2 Numerical Simulation of the Wind Turbine Site

3.2.1 Geometry of the Wind Turbine Site

A CFD model is generated for a wind turbine located near a fire station in a suburban part of Manhattan, KS, to compare simulated wind speeds to measurements taken at this site. The grid mesh is shown in Fig. 3.7, with the north face displayed. There are three points created at elevations of 7.6 m, 15.2 m, and 18.3 m from the ground to represent where the two anemometers and the turbine rotor are.

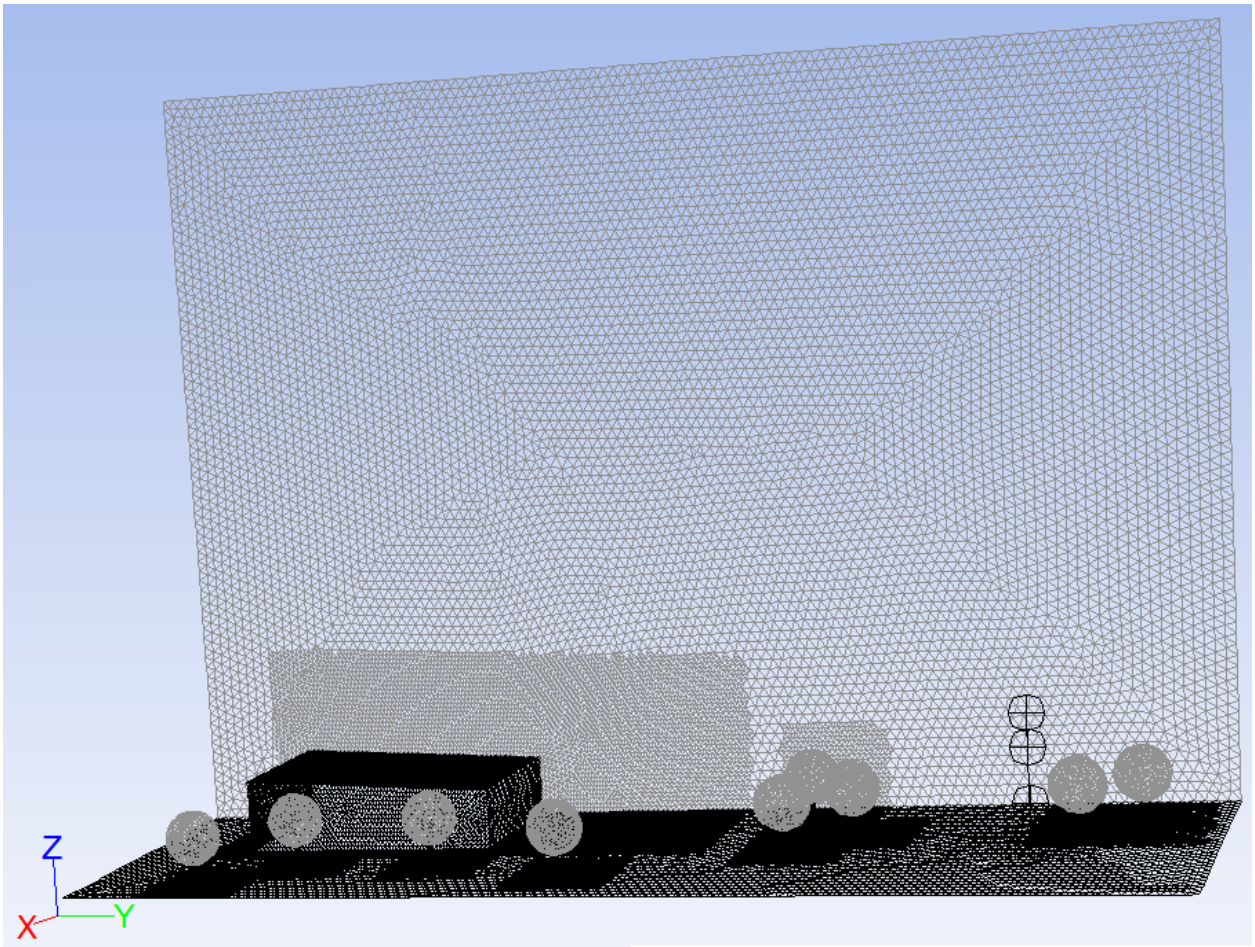

Figure 3.7 Grid mesh of the wind turbine site in Manhattan, KS, showing refinement around the fire station and trees

The computational domain is a rectangular volume with (x, y, z) dimensions of (48 m, 164 m, 118 m), where the positive x direction points south, the positive y direction goes from west to east, and the z direction is the elevation. The origin is located at the (x, y, z) coordinates of (0, 0, 0). An upward grade of three degrees is applied to the ground from west to east according to the elevation measurements taken from Google Earth (2011). The absolute position of the rotor of the wind turbine in the computational domain is raised an additional 7.2 m after applying the grade. The fire station is modeled as a rectangular solid with smooth walls. It has (x, y, z) dimensions of (22 m, 40 m, 12 m) and is located with its northwest corner at the (x, y, z) coordinates of (0, 18 m, 0). Each tree is assumed to have the same dimensions. Their cylindrical trunks are 0.4 m in radius and 3 m in height. Their spherical canopies are 8 m in diameter with

the center of the canopies 7 m from the ground. The (x, y, z) coordinates for the base of each tree are given in Table 3.5.

Table 3.5 (x, y, z) coordinates of the base of each tree in the simulation of the wind turbine

Tree designation	x coordinate, m	y coordinate, m	z coordinate, m
A	40	18	0.8
B	30	30	1.4
C	30	52	2.6
D	36	74	3.6
E	8	104	5.2
F	24	104	5.2
G	16	112	5.6
H	16	144	7.2
I	10	152	7.6

3.2.2 Numerical Modeling

A transient flow model is used, with a first-order, steady implicit solver. The k-epsilon (k-ε), renormalization-group (RNG) turbulence model is adopted, with a non-equilibrium near-wall treatment (Fluent User's Guide, 2006). Launder and Spaulding (1972) recommend the k-ε model for fully turbulent flows with a high Reynolds number. The calculation accuracy of the vortices is improved using the RNG option (Yakhot and Orszag, 2009). The non-equilibrium near-wall treatment also improves the calculations of the three-dimensional vortices in the boundary layer (Kim and Choudhury, 1995). A convergence residual value of $1 \cdot 10^{-3}$ is used for the turbulence parameters as well as the continuity, and a value of $1 \cdot 10^{-5}$ is used for the velocities (Fluent User's Guide, 2006).

3.2.3 Grid Sensitivity

The grid size and shape are critical in the accuracy of the simulation. A grid sensitivity check was conducted for grid sizes of 16%, 13%, 10%, 7%, and 5% of the length of the diameter of the tree canopy. The drag coefficient, wind velocity, and turbulent kinetic energy contours had

an accuracy of around 86% compared to literature (Schlichting, 2000, Gromke and Ruck, 2008) using grid sizes of 16% and 13% of the diameter of the tree canopies. The parameters had accuracies of around 94% with grid sizes of 10% of the diameter of the tree canopies and smaller. The results of the drag coefficient for the grid size of 10% of the diameter of the tree canopies are shown in Fig. 2.1. The cells in the overall domain are thus sized to 10% the diameter of the tree canopies. The mesh is also refined around with the same cell sizes around the fire station, primarily above and downwind from the building. An additional grid sensitivity check will be conducted for the west to east wind simulation in the calculation of the wind speeds.

3.2.4 Boundary Conditions

3.2.4.1 Power-Law Profile for Wind Speed

The power-law profile for wind speed is chosen based on its popular use in wind engineering, directness, and simplicity (Spera, 2009). The wind speed profile is expressed by Eq. (3.3) as,

$$U(z) = U_{ref}\left(\frac{z}{z_{ref}}\right)^{\alpha} \tag{3.3}$$

where U_{ref} is the reference wind speed, z_{ref} is the reference elevation, and α is the power-law exponent (Spera, 2009). The power-law profile for wind speed at different terrains are found in a number of sources. The simulations in this research will use the wind speed measurements taken at the meteorological tower to acquire U_{ref} for z_{ref}=31.1 m. The method of least squares is used to calculate U_{ref} to build the wind speed profile based on the three measurement points at the meteorological tower.

This study will provide a range of exponent values (α) established by different research groups to check for the accuracy of the models to the measurements taken at the wind turbine. Gromke and Ruck (2008) conducted wind tunnel experiments on model trees using α=0.220. Counihan (1975) derived an equation to calculate the exponent, which is shown by Eq. (3.4),

$$\alpha = 0.096\log_{10} z_0 + 0.016(\log_{10} z_0)^2 + 0.24 \tag{3.4}$$

where the surface roughness length z_0 is tabulated by Manwell et al. (2002). For a location with trees and a few buildings, z_0=0.25 m (Manwell et al., 2002). Kaufman (1977) provided an equation based on short averaging times of high-elevation wind, and is shown by Eq. (3.5) as,

$$\alpha = 0.55 U_{ref}^{-0.77} \tag{3.5}$$

Spera and Richards (1979) provided another method in calculating the exponent for the use in simulating the atmospheric conditions for large wind turbines. Their resulting form of the exponent is given in Eq. (3.6) as,

$$\alpha = \left(\frac{z_0}{10}\right)^{0.2} \left(1 - 0.55 \log_{10} U_{ref}\right) \tag{3.6}$$

where z_0=0.40 m for the outskirts of a suburban area based on tabulated surface roughness lengths by Spera (2009). A summary of the calculations for U_{ref} and α is given in Table 3.6, using a least squares fit to the meteorological data for both Jan. 30, 2011, and Feb. 6, 2011.

Table 3.6 Values used in the power-law profile for wind speed based on the meteorological tower measurements

	Jan. 30, 2011 (obstructed wind flow)		Feb. 6, 2011 (unobstructed wind flow)	
Reference	U_{ref}	α	U_{ref}	α
Gromke and Ruck (2008)	6.263	0.220	7.164	0.220
Counihan (1975)	6.224	0.188	7.120	0.188
Kaufman (1977)	6.163	0.136	7.032	0.123
Spera and Richards (1979)	6.350	0.293	7.242	0.277

Along with the measurements, the wind speed profiles using each reference are generated and shown in Fig. 3.8(a) and Fig. 3.8(b) for Jan. 30, 2011, and Feb. 6, 2011, respectively. This study will use the Counihan (1975) expression for the inlet condition of the simulations, based on its extensive support from other research (Baric et al., 2010, Spera, 2009, Kozmar, 2008, Manwell et al., 2002) and based on the reasonable fit with the measurements. The deviations of

the fit for the wind measurements on Jan. 30, 2011, are given in Table 3.1 and Table 3.2 for the wind turbine and the meteorological tower, respectively. The deviations of the fit for the wind measurements on Feb. 6, 2011, are given in Table 3.3 and Table 3.4 for the wind turbine and the meteorological tower, respectively.

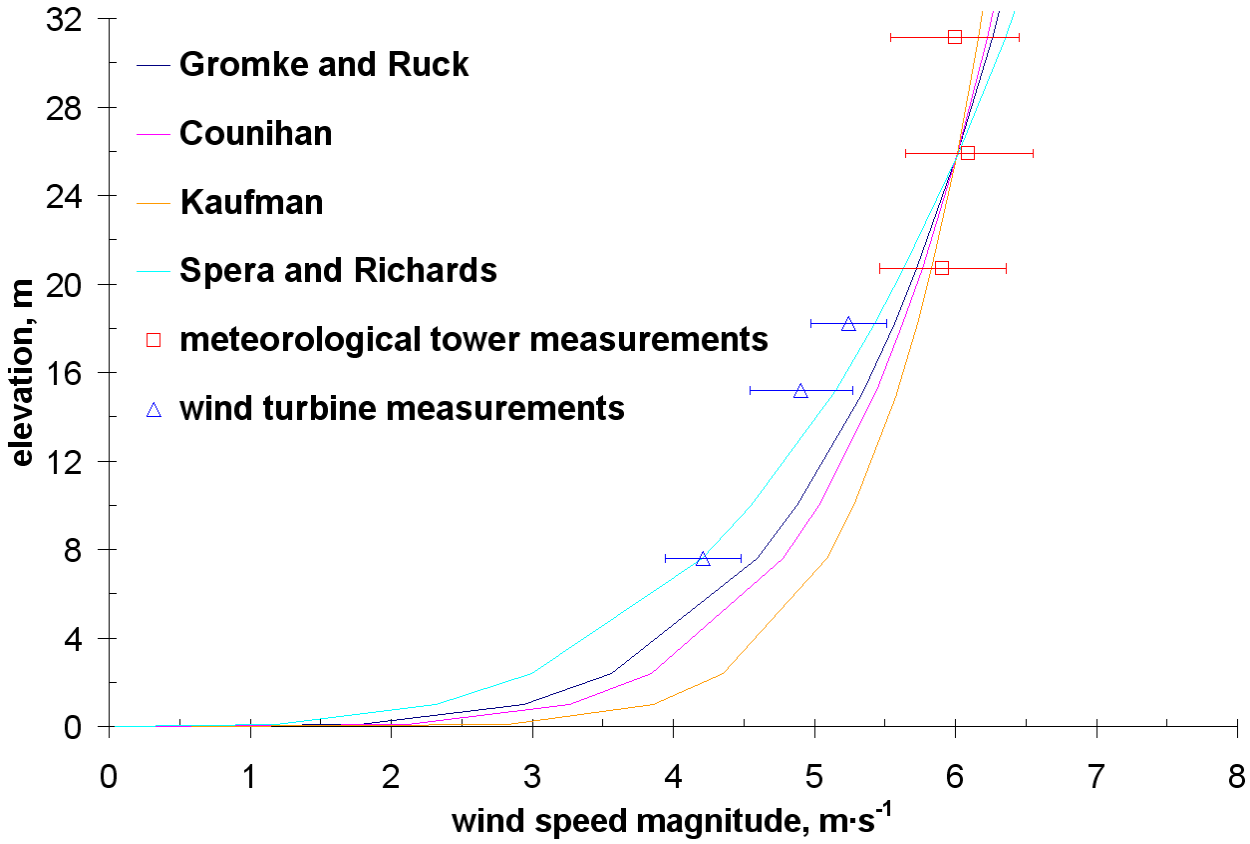

(a) Wind speed profiles using the wind measurements from Jan. 30, 2011

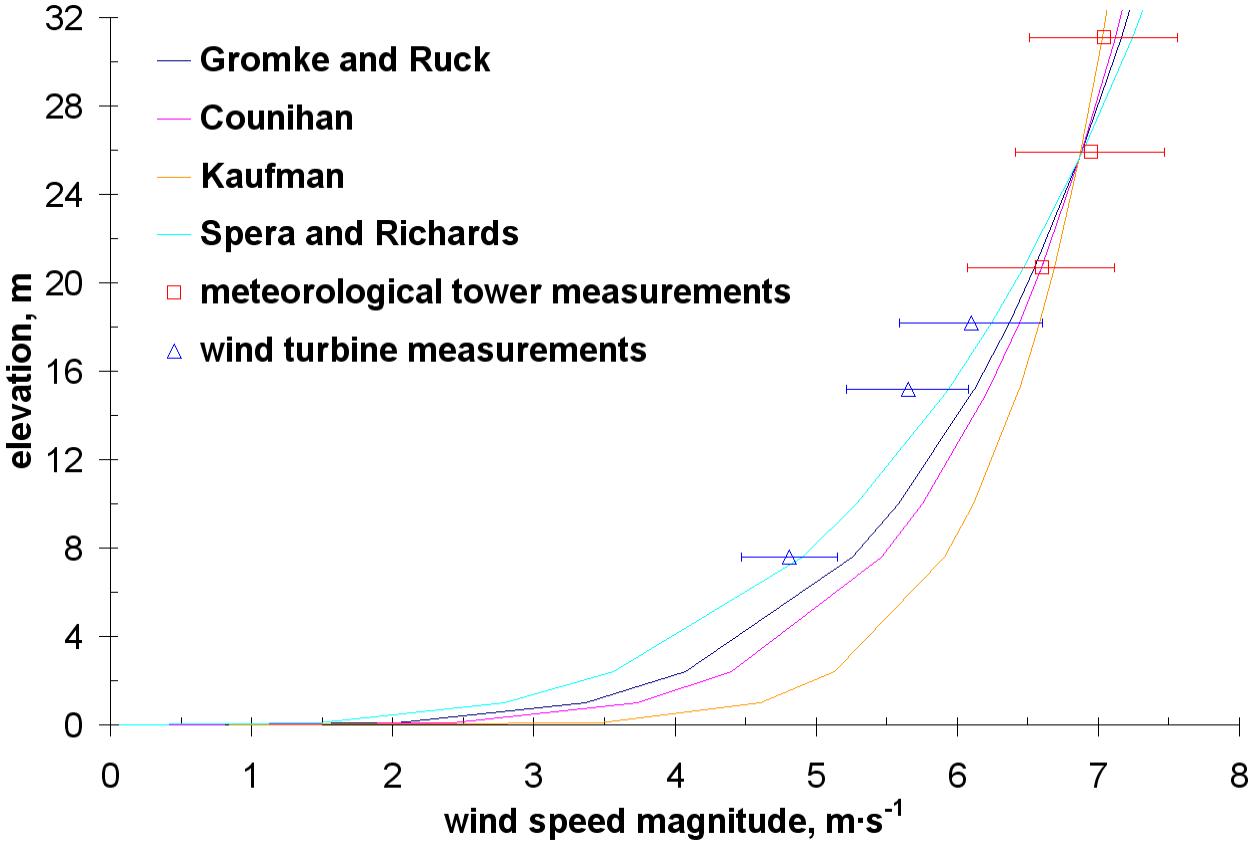

(b) Wind speed profiles using the wind measurements from Feb. 6, 2011

Figure 3.8 Power-law profile for horizontal wind velocity based on different references, showing the wind measurements between the time of 600 hours and 1800 hours for (a) Jan. 30, 2011 and for (b) Feb. 6, 2011

3.2.4.2 Power-Law Profile for Turbulence Intensity

The power-law profile for turbulence intensity is also a common choice in wind engineering. The turbulence intensity profile is expressed by Eq. (3.7) as,

$$I(z) = I_{ref}\left(\frac{z}{z_{ref}}\right)^{-\beta} \tag{3.7}$$

where I_{ref} is the reference turbulence intensity at the reference elevation, and β is the power-law exponent for turbulence intensity (Zhou and Kareem, 2002).

There has been an abundant amount of research in correlating turbulence intensity characteristics to different terrains (Kozmar, 2011, Bashor and Kareem, 2009, Tieleman, 2003,

Zhou and Kareem, 2002). The American Society of Civil Engineers (ASCE) generated the ASCE 7-98 standard, the National Research Council of Canada (NRCC) developed the National Building Code of Canada (NBCC) specification, and the European Committee for Standardization developed the Eurocode (Bashor and Kareem, 2009, Zhou and Kareem, 2002). For the simulations in this study, the turbulence intensity profile will be based on a suburban terrain exposure type with scattered obstructions (Zhou and Kareem, 2002). Table 3.7 shows the values of I_{ref} and β at z_{ref}=10 m for the suburban exposure.

Table 3.7 Values used in the power-law profile for turbulence intensity based on different references

Reference	I_{ref}, %	β
ASCE 7-98	20.0	0.17
NBCC	20.0	0.14
Eurocode	19.0	0.16

The turbulence intensity profiles using each reference as well as the turbulence intensity calculated from the wind measurements are shown in Fig. 3.9 for Jan. 30, 2011, and Feb. 6, 2011. The turbulence intensity in the wind measurements is calculated by taking the deviation due to the turbulence in the wind speed at the corresponding elevation and dividing it by the average wind speed at the corresponding elevation. This study will use the ASCE 7-98 expression, based on its extensive support from other research (Baric et al., 2010, Bashor and Kareem, 2009, Kozmar, 2008, Zhou and Kareem, 2002) and based on the reasonable fit with the measurements. The broad scatter among the measurements is typical, since there are many variables that affect the profile, including diurnal stratification, daily weather, and obstructions at a site (Kozmar, 2011, Tieleman, 2008, Tamura et al., 2007, Manwell et al., 2002).

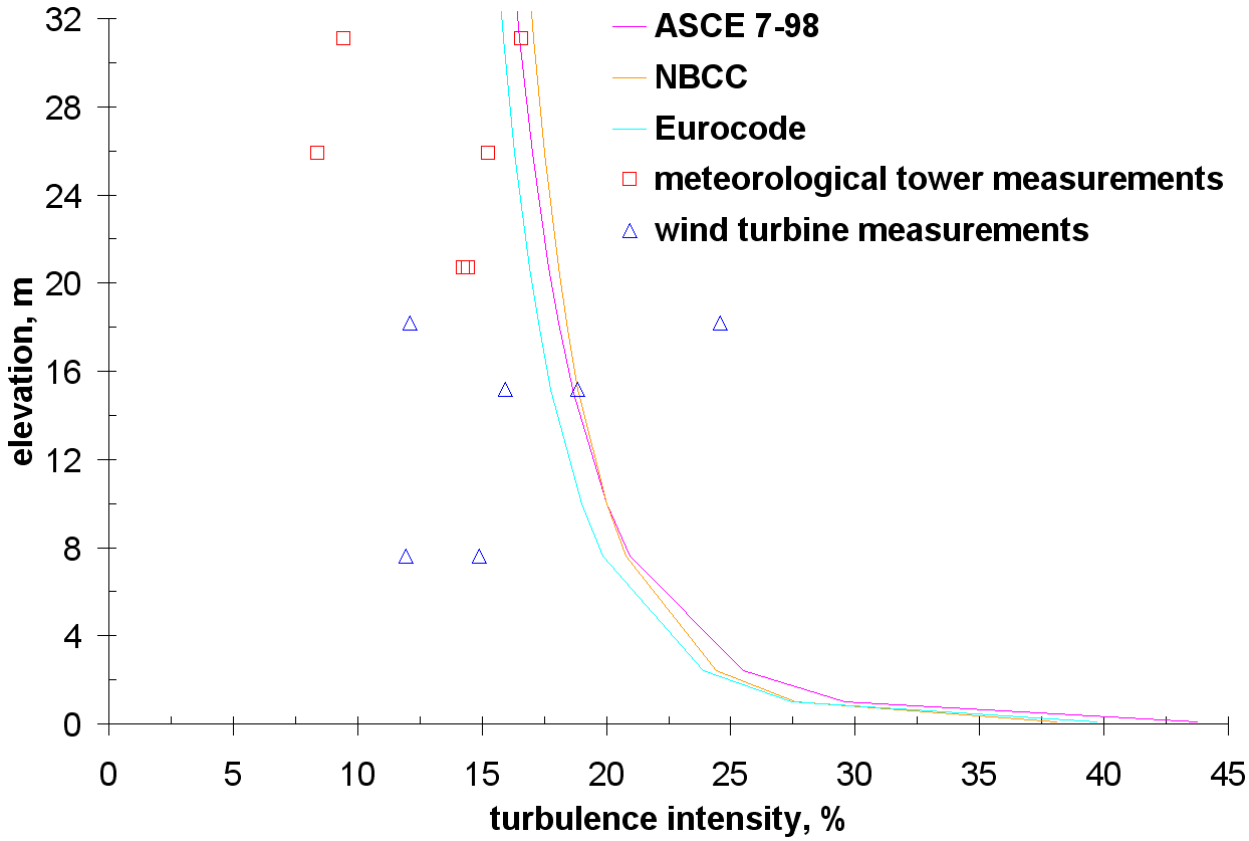

Figure 3.9 Power-law profile for turbulence intensity based on different references, showing the calculated turbulence intensity values using the wind measurements between a time of 600 hours and 1800 hours for Jan. 30, 2011, and Feb. 6, 2011

3.2.4.3 Top and Bottom Boundary Conditions

After modeling the velocity boundary condition using power-law profiles in user-defined functions, modeling the top boundary condition for atmospheric flow has been addressed in this study. The top boundary condition is implemented with a user-defined function, specifying a windward velocity with a value designated by the power-law profile for wind speed, with the gradients in the lateral (x) and vertical (z) directions set to zero (Rakai and Kristof, 2010, Zhang, 2009). The top boundary condition is chosen to be about four times higher than the elevation of the rotor to prevent losses in the inlet conditions (Hargreaves and Wright, 2007, Chang, 2006).

The bottom boundary condition is implemented with a surface roughness. The surface roughness height for the bottom boundary condition is set to 0.008 m in the wall boundary

condition options of the software (Fluent User's Guide, 2006) assuming the ground to be lawn grass (Manwell et al., 2002).

3.2.4.4 Trees

The trees are assumed to have identical properties. The tree canopies are set as laminar porous zones to calculate the internal substrate flow without turbulence, since the flow speed is substantially reduced inside the canopies in the cases studied here. The viscous resistance (R_v) and the form drag, or inertial resistance (R_i), values of the tree canopies are set based on evaluating the added Darcy-Forchheimer source term (S_i) in the i-direction for the turbulent kinetic energy and momentum equations (Sanz, 2003). The source term is modeled using Eq. (2.14). The viscous resistance is set to zero because it is negligible as compared to the inertial resistance due to the leaf fluttering properties of a tree (Endalew et al., 2009). The tree canopies are modeled with an inertial resistance of 18.0 m^{-1}, assuming the wind resistance properties of sisal fiber or wood wool trees modeled by Gromke and Ruck (2008).

3.3 Results of the Comparison of the Simulations to the Wind Measurements

3.3.1 West to East Wind Direction

3.3.1.1 Comparison of the Power-Law Profile for Wind Speed

The simulated wind speeds at the anemometer and rotor positions compare closely to the measurements. Figure 3.10 shows where the averages and deviations of the measurements and simulated wind speeds lie with respect to the profiles. The deviations of the fit for the simulation on Jan. 30, 2011, are shown in Table 3.8.

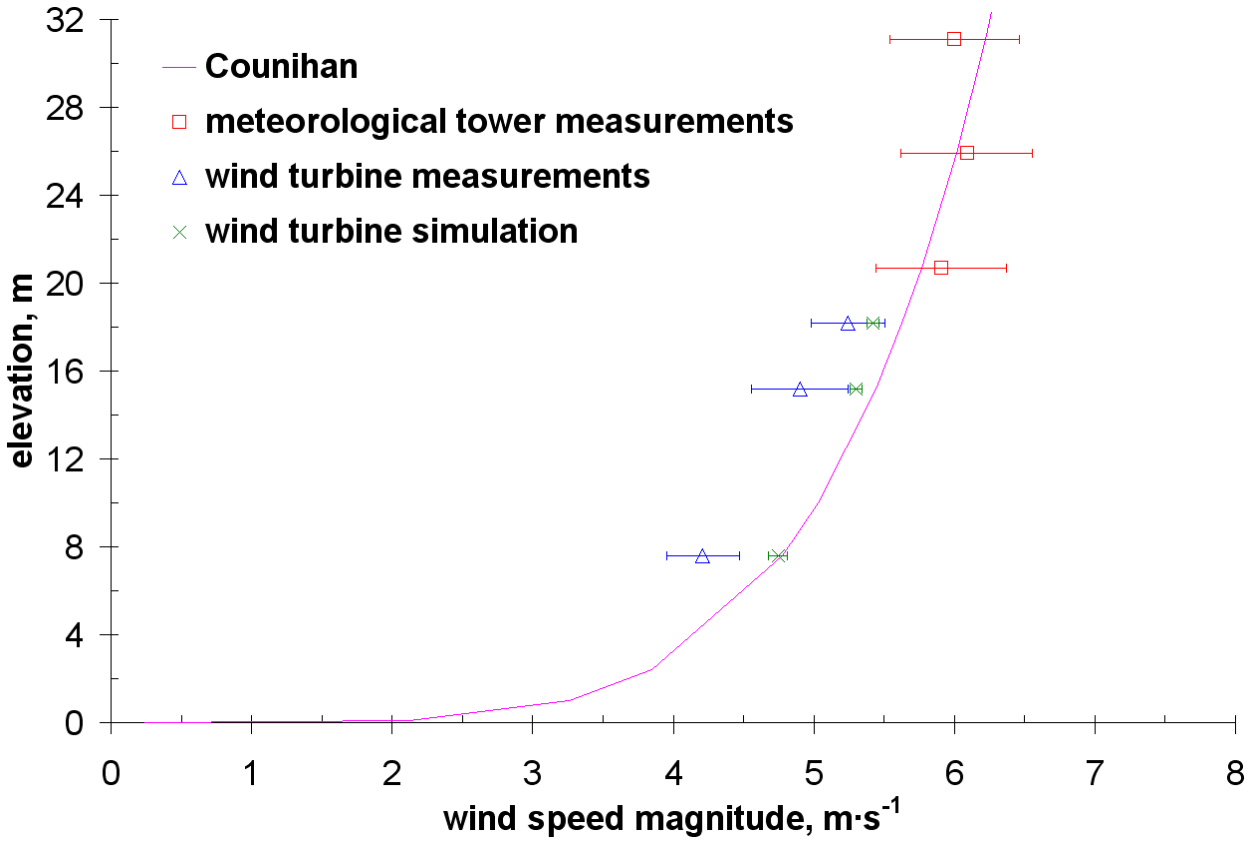

Figure 3.10 Power-law profile for wind speed in the west to east direction based on Counihan (1975), showing the average and deviation of the wind measurements and the simulation results between the time of 600 hours and 1800 hours from Jan. 30, 2011

The wind speed reduction due to the obstructions on the ground is observed in Fig. 3.10 where the simulated wind speeds are generally lower than the incoming wind speed profile. The simulated wind speeds deviate from the curvature of the incoming wind speed profile, with most of the wind speed reduction occurring at the two locations with elevations of the tree canopies. The turbulence from the obstructions is visualized by these differences. To visualize the flow field, the contour plots for the velocity magnitude and the turbulent kinetic energy in a plane going through the wind turbine are shown in Fig. 3.11 and Fig. 3.12, respectively.

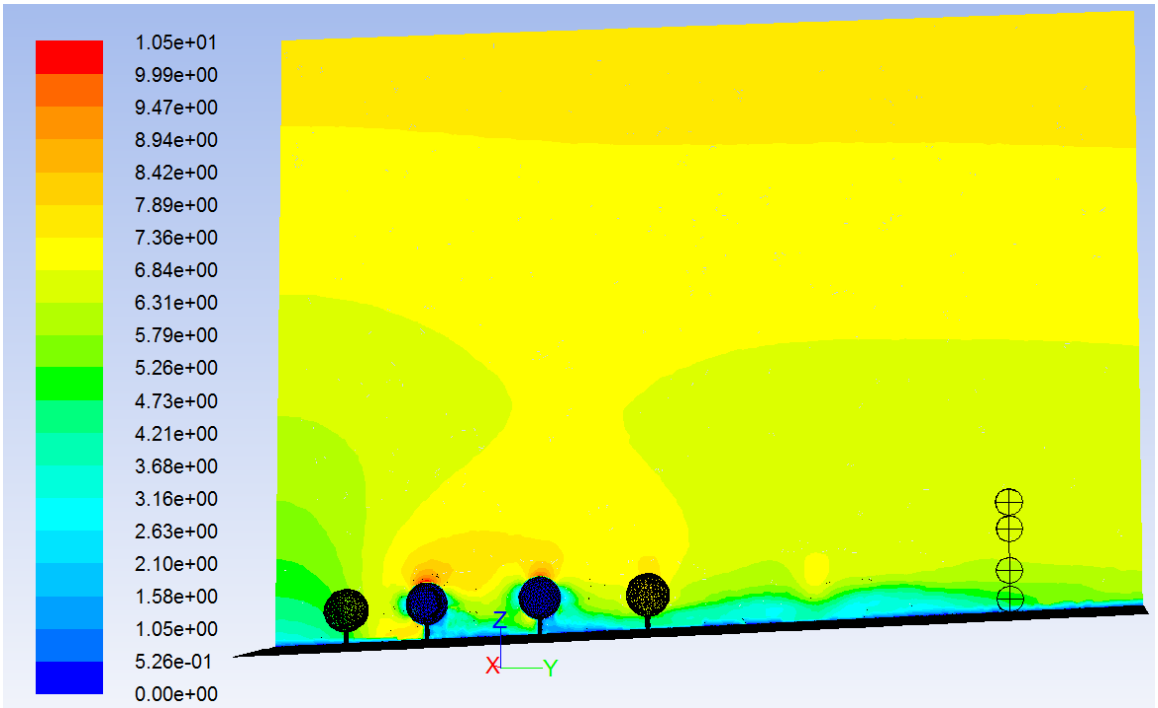

Figure 3.11 West to east horizontal velocity contour plot on a plane running through the wind turbine

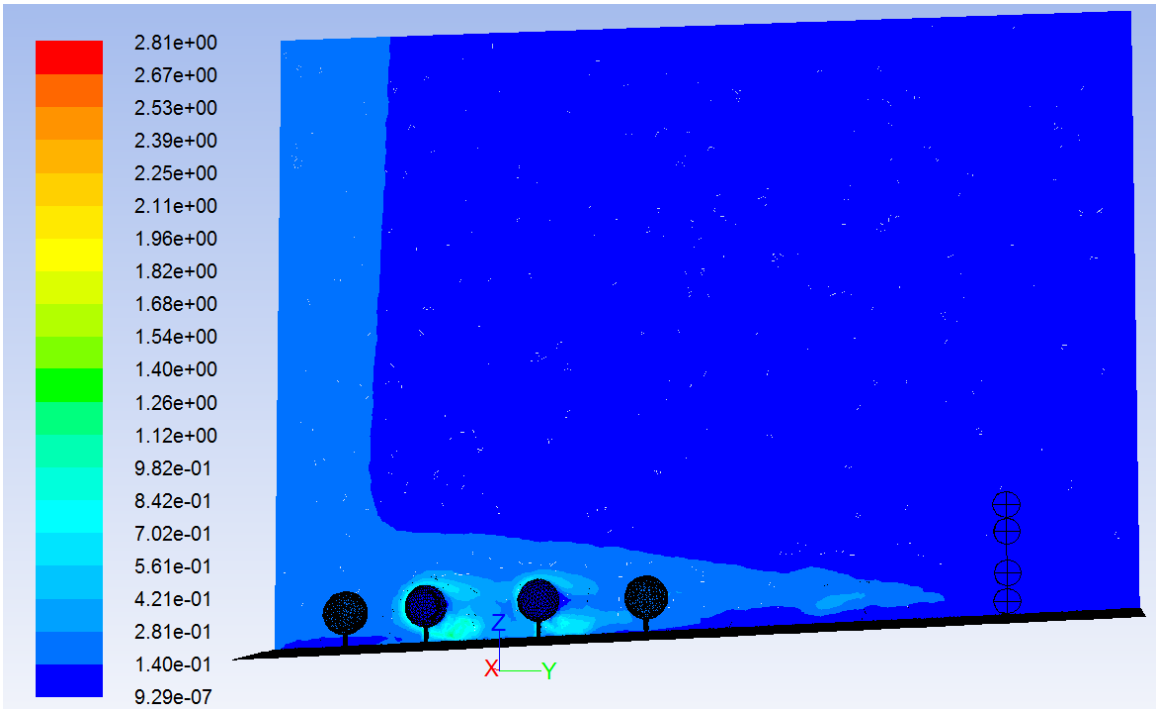

Figure 3.12 West to east turbulent kinetic energy contour plot on a plane running through the wind turbine

The horizontal velocity contour for Jan. 30, 2011, shows the incoming power-law profile for the wind speed on the left side. The trees cause a distortion in the profile of the wind speed, especially above the trees. Downwind from trees, there are notable fluctuations in the wind speed along the ground, especially on the ground up to an elevation equal to the height of the trees. The fluctuations occur even up to the location of the wind turbine, about six tree lengths downwind from the last tree.

The turbulent kinetic energy contour for Jan. 30, 2011, shows the incoming power-law profile for the turbulence intensity in the wind speed. Most of the turbulence in the wind is concentrated around the tree canopies, mostly between the trees, and even up to five tree lengths downwind from the last tree. These contours show that small-scale wind turbines should be located away from trees not only in close proximities, but also at notable distances to avoid the effects of turbulence in the wind caused by obstructions on the ground.

3.3.1.2 Grid Resolution Effects on the Simulated Wind Speed

A grid resolution check is conducted for the west to east wind simulation using three different grid sizes. Based on a cell size that is 5% of the diameter of a tree canopy, the grid size is 3,309,818 cells. Two lower grid resolutions are simulated. Grids with cell sizes of 5.6% and 6.3% of the diameter of the tree canopy are generated, resulting in grid sizes of 2,482,780 and 2,127,755, respectively. Table 3.8 shows that the 3,309,818 grid size is sufficient in the accuracy of the simulation since the lower grid resolutions do not show substantial discrepancies in the calculation of the wind speed averages and deviations. The larger cell sizes of the lower grid resolutions cause the calculations of the wind speed at the middle and lower anemometers to be slightly miscalculated. The wind speed is over-predicted at the middle anemometer because the enlarged cells average the wind speed with a larger cell face, incorporating more of the higher flow field. The wind speed is under-predicted at the lower anemometer, since the enlarged cells incorporate the slower wind speed on the ground in the cell calculations.

Table 3.8 Simulated west to east wind speed averages and deviations using different grid resolutions

Number of cells	3,309,818		2,482,780		2,127,755	
Wind speed calculation, $m \cdot s^{-1}$	Average	Deviation due to turbulence	Average	Deviation due to turbulence	Average	Deviation due to turbulence
Rotor, 18.3 m	5.422	0.139	5.457	0.050	5.668	0.047
Anemometer, 15.2 m	5.300	0.143	5.291	0.059	5.382	0.058
Anemometer, 7.6 m	4.745	0.258	4.803	0.187	5.011	0.165

3.3.2 South to North Wind Direction

In the south to north wind direction, the wind speed should be and is relatively faster without any obstructions to the wind. Figure 3.13 shows this characteristic in the Counihan (1975) wind speed profile for Feb. 6, 2011, where the measurements and the simulated wind speeds are all generally higher in value than for Jan. 30, 2011. The measurements and simulated wind speeds for Feb. 6, 2011, are shown in Fig. 3.13. The deviations of the fit for the simulation on Feb. 6, 2011, are shown in Table 3.9. The small deviation in the wind speed for the simulation of Feb. 6, 2011, is due to the open flow between the inlet and the data point locations.

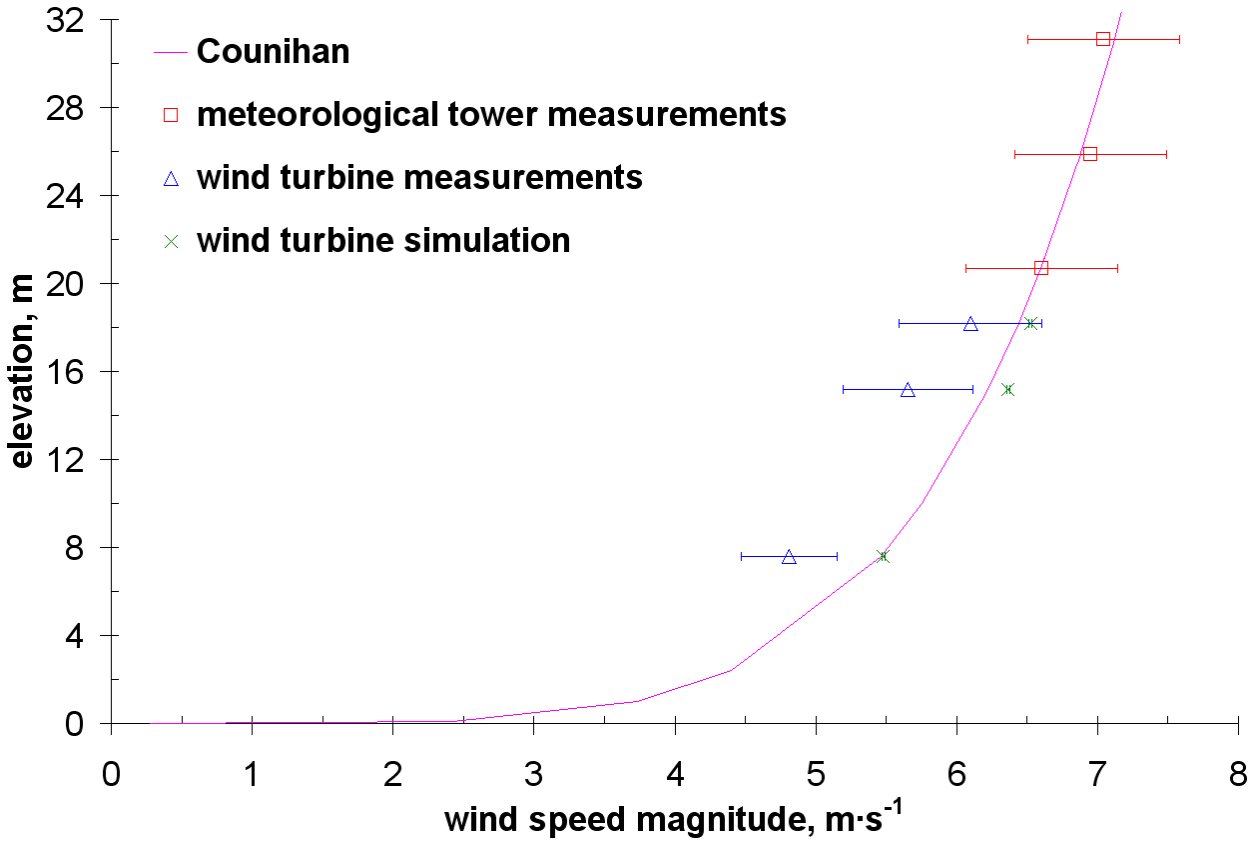

Figure 3.13 Power-law profile for wind speed in the south to north direction based on different references, showing the average and deviation of the wind measurements and the simulation results between the time of 600 hours and 1800 hours from Feb. 6, 2011

The wind speed averages of the measurements and the simulation again lie closely within the range of the incoming Counihan (1975) profile, since there are no immediate obstructions to the wind with respect to the location of the wind turbine. Sporadic wind gusts may contribute to the lower average wind speed at the 15.2 m elevation measurement (Tieleman, 2008). To visualize the flow field, the contour plots for the velocity magnitude and the turbulent kinetic energy in a plane going through the wind turbine are shown in Fig. 3.14 and Fig. 3.15, respectively. Table 3.9 shows the values for the averages and deviations at each anemometer location in the simulation for the south to north wind case.

The horizontal velocity contour for Feb. 6, 2011, shows the incoming power-law profile for the wind speed on the right side. Without any significant trees obstructing this wind direction, the wind speed profile is carried out through the computational domain. The tree located

downwind in this case is negligible regarding its effects on the wind measurements on the wind turbine.

The turbulent kinetic energy contour for Feb. 6, 2011, shows the incoming power-law profile for the turbulence intensity in the wind speed. Again, without any significant obstructions in this wind direction, the profile is maintained throughout the computational domain.

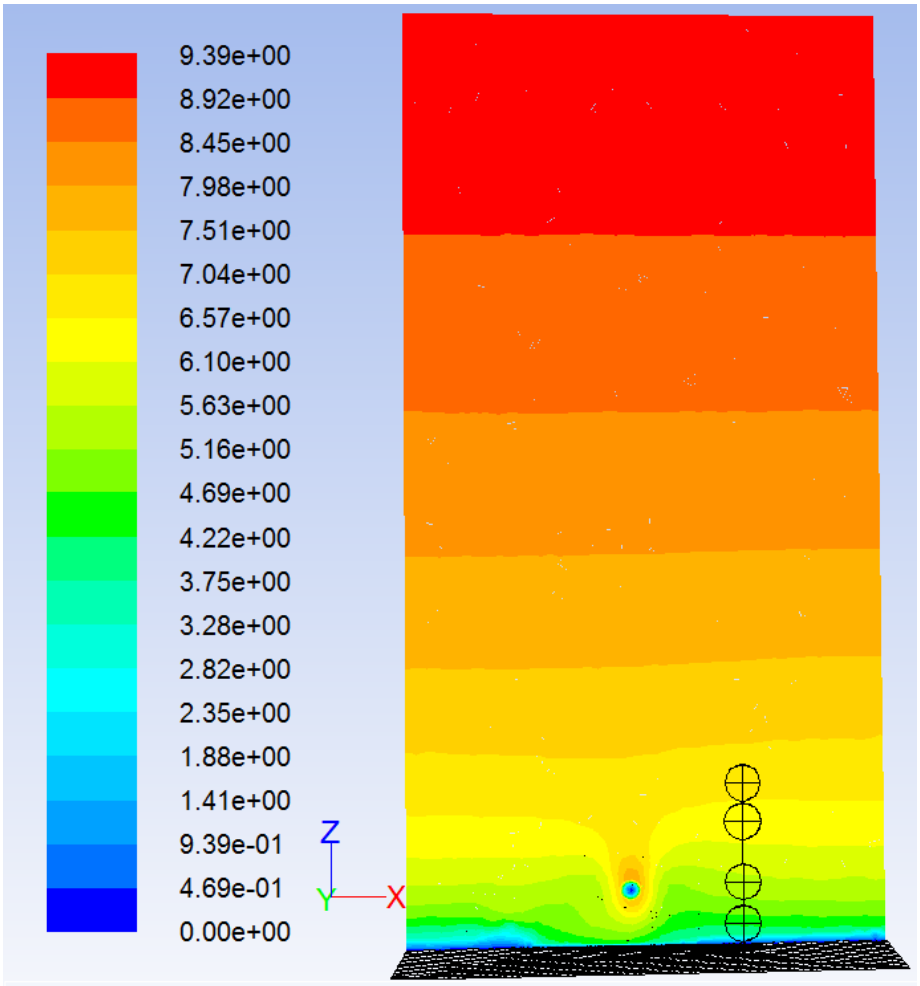

Figure 3.14 South to north horizontal velocity contour plot on a plane running through the wind turbine

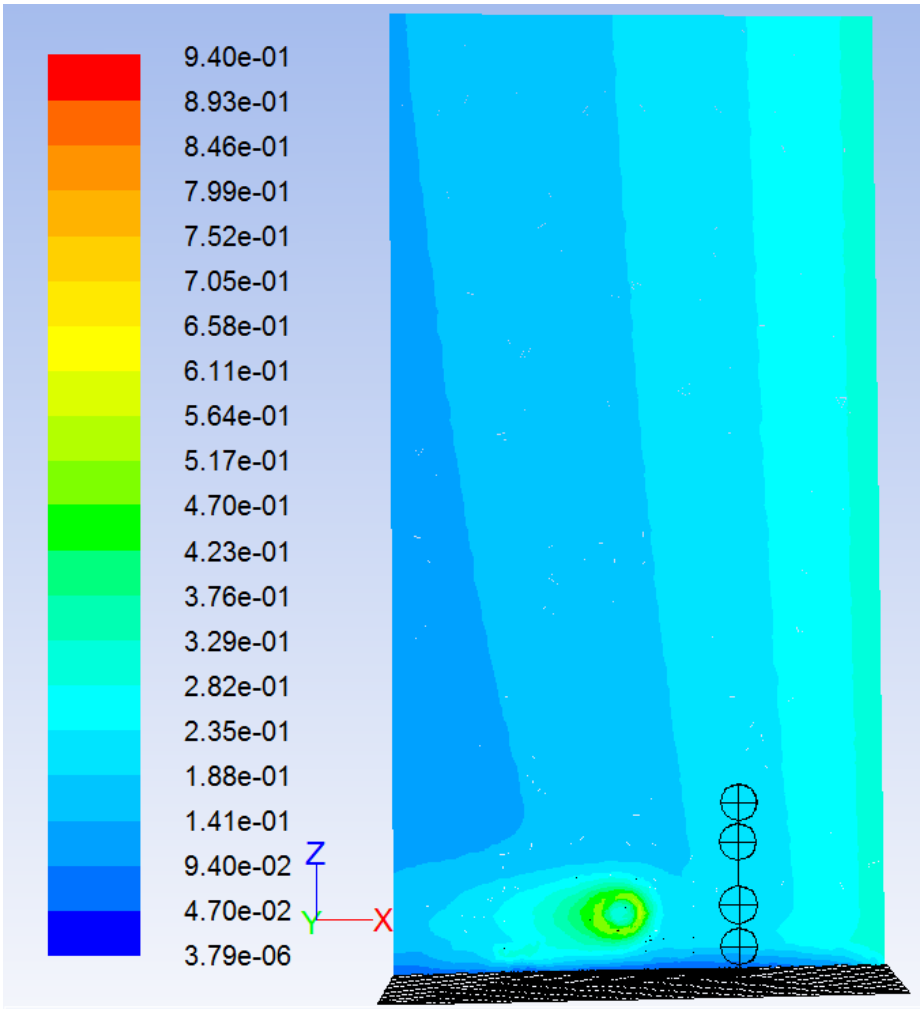

Figure 3.15 South to north turbulent kinetic energy contour plot on a plane running through the wind turbine

Table 3.9 Simulated south to north wind speed averages and deviations using the grid resolution with 3,309,818 cells

Wind speed calculation, $m \cdot s^{-1}$	Average	Deviation due to turbulence
Rotor, 18.3 m	6.524	0.001
Anemometer, 15.2 m	6.366	0.001
Anemometer, 7.6 m	5.480	0.003

3.4 Summary

Improvements in predicting low-elevation wind speeds in a specific location can be accomplished using CFD. This study shows how recently studied power-law profiles for wind speed and turbulence intensity can be used in a simulation of a local environment, in combination with key boundary conditions, to improve the estimations quickly, and more accurately than current methods. For example, using a high-elevation wind map for Kansas (Schuster, 2009), the wind speed at a 50 m elevation in Manhattan, KS, is approximately 6.5 $m \cdot s^{-1}$. Using the exponent from Counihan (1975), the wind speed is 5.4 $m \cdot s^{-1}$ at an elevation of 18.3 m. From the power curve of the wind turbine model used at the site (Calley and Kruse, 2011), the wind map estimates a power output of 300 W. For the Jan. 30, 2011, case, the measured output is 280 W and the simulated output is 320 W. The wind map estimate matches well for the Jan. 30, 2011, case. However, for the Feb. 6, 2011, case, the measured output is 500 W and the simulated output is 570 W. Using the wind map, the estimate is still 300 W. A clear and significant difference is seen in the capability of using CFD to estimate day-to-day power production versus using a high-elevation wind map.

With the key CFD settings presented in this research, the energy output can be calculated more accurately, even day to day, if the general wind speed and direction at some time in the afternoon is known. These CFD settings are listed as the following:

• A power-law profile for the incoming wind speed and turbulence intensity is sufficient, as long as the profile suits the terrain.

• A grid resolution where the cell size is at least 5% or smaller than the diameter of a tree canopy is recommended.

• The top boundary should be modeled using a user-defined function where the velocity in the direction of the wind is established, and the lateral and vertical gradients are set to zero.

• The trees are included in the simulation, and are modeled properly with the appropriate wind resistance characteristics.

The use of CFD avoids the excessive costs and uncertainty in predicting the potential and actual energy at a location. The savings in cost and time, as well as the reduction in uncertainty of estimation accuracies, will not only benefit commercial investors, but also customers in under-developed countries in which a single wind turbine may provide enough electricity for a single day's use. These reasons support the necessity of accurate CFD modeling of low-elevation

atmospheric conditions towards improving the estimation of attainable energy at a potential small-scale wind turbine site.

Chapter 4 - Using System Identification to Estimate Wind Turbine Power Production based on Anemometer Measurements

In the fourth chapter, I will discuss how system identification can be used to correlate anemometer wind speeds to the power output of a wind turbine. The transfer functions generated by different models are compared, and a general model is selected to compare its modeled power output to actual power output measurements from the wind turbine.

4.1 System Identification Models

To correlate the anemometer wind speed to the measurements from the wind turbine, system identification is implemented. This process is possible if the input and output signals are known. In this study, the input signal is the anemometer wind speed and the output signal is the wind turbine rotational speed. Typically, there are five steps in identifying a simulated output. These steps are to take measurements for the input and output signals, select a model, adjust and assess the model, and evaluate the results of the model (Lopez-Cruz et al., 2007). To limit the amount of variables to adjust, the conclusion given by Lopez-Cruz et al. (2007) is assumed, where 77% of the time history for both signals is used for the estimation of the model, and 23% of the time history is used for the validation. A range of parameters conducted in this study will be kept under an order of ten, sufficiently covering the results from previous research in this topic (Kanellos et al., 2011).

4.1.1 Measurements

The wind speed and rotational speed measurements are analyzed for three random days showing quasi-steady state wind behavior. The selected days are Jan. 30, 2011, Feb. 5, 2011, and Feb. 6, 2011. Each measurement is taken at one minute intervals. The range of data that is analyzed is between a time of 600 hours and 1800 hours to avoid diurnal effects from stratification (Tieleman, 2008). The anemometer is attached to the tower of the wind turbine, where the elevation of the anemometer is 15.2 m, and the elevation of the rotor of the wind turbine is 18.3 m. The time history of the anemometer wind speed and the wind turbine rotational speed is shown in Fig. 4.1(a), Fig. 4.1(b), and Fig. 4.1(c), for Jan. 30, 2011, Feb. 5, 2011, and Feb. 6, 2011, respectively.

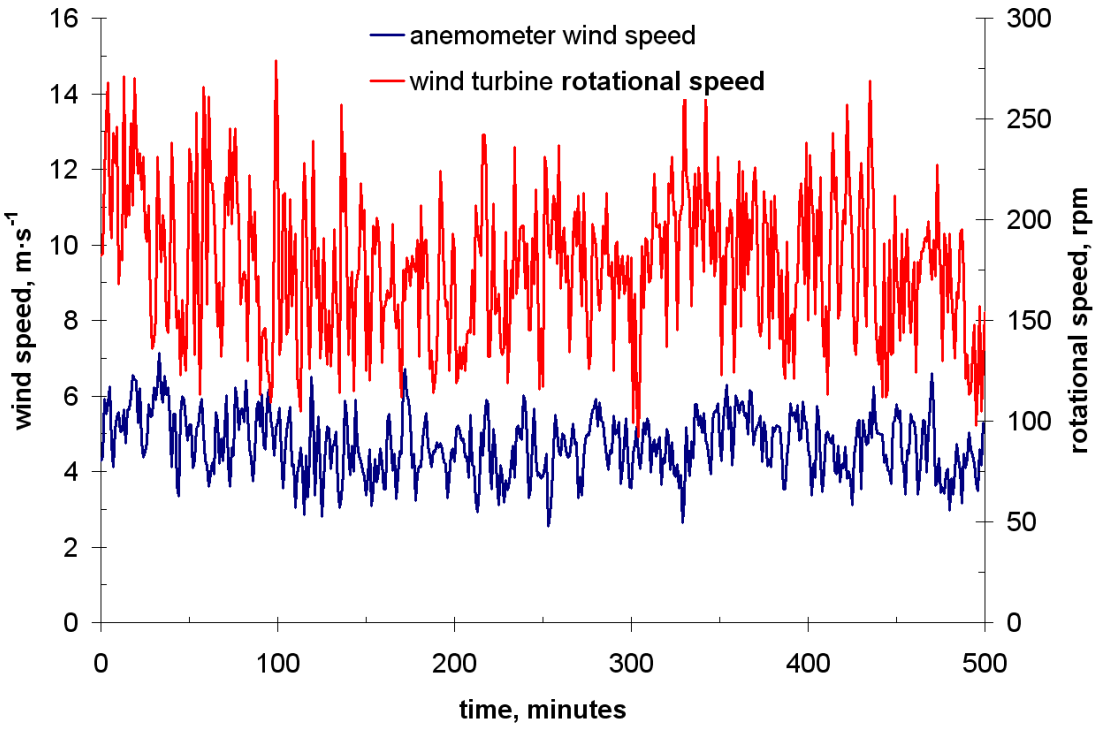

(a) Time history of measurements on Jan. 30, 2011

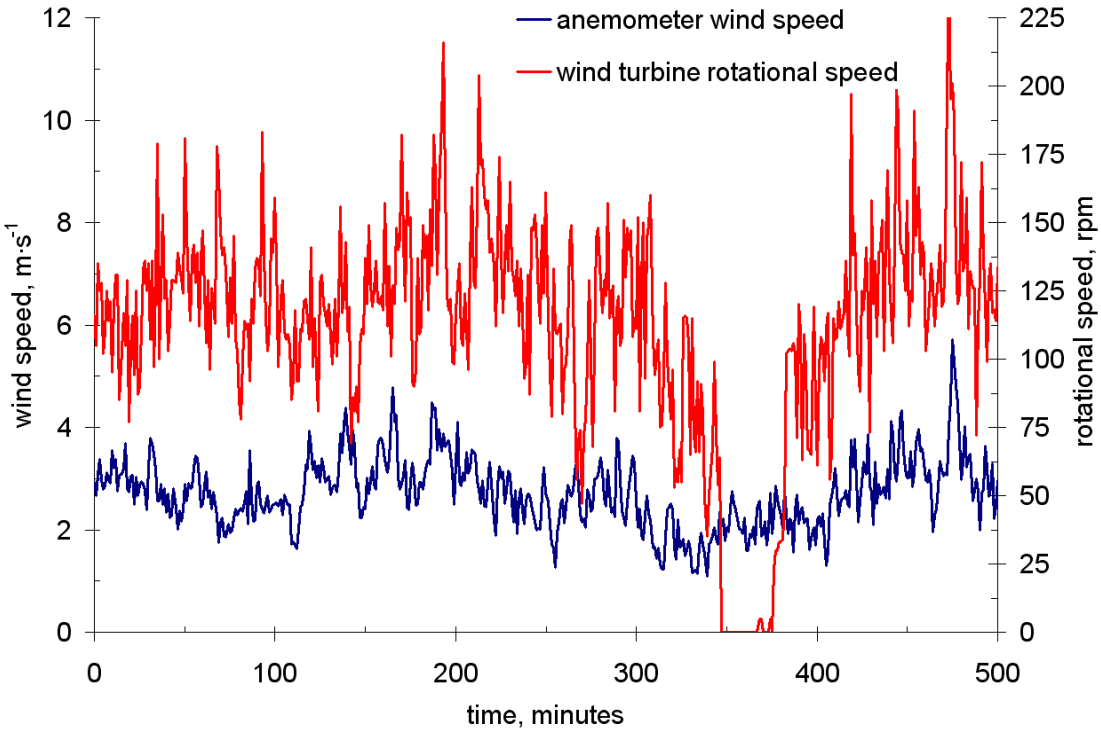

(b) Time history of measurements on Feb. 5, 2011

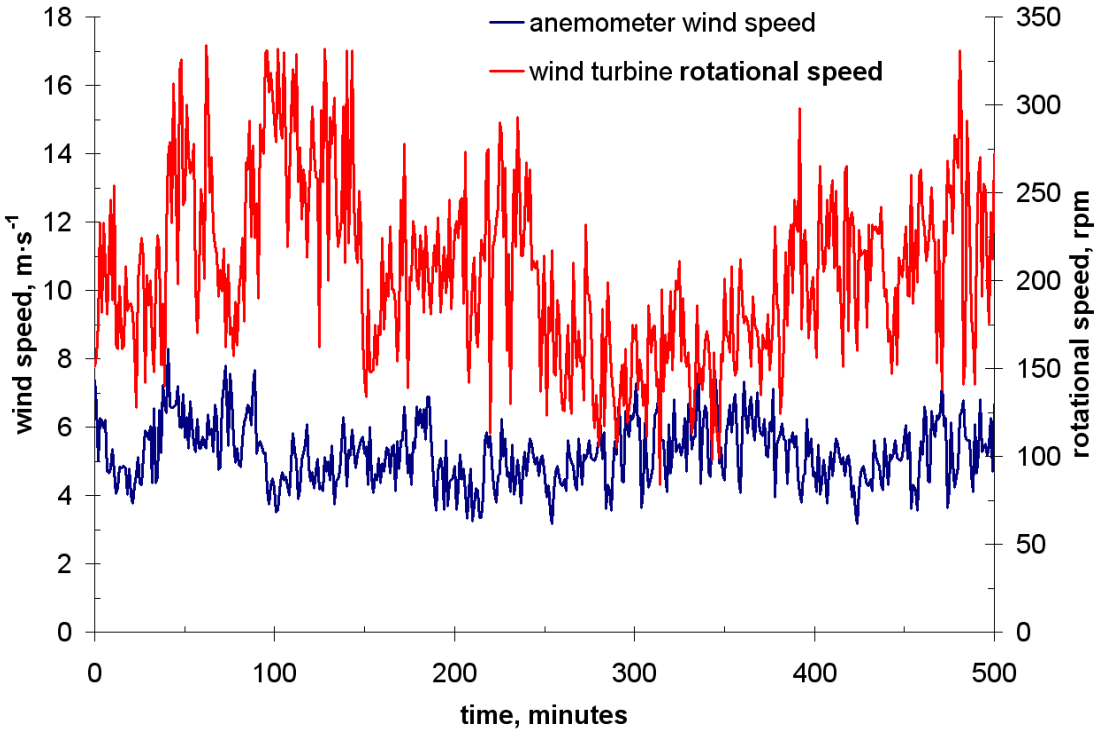

(c) Time history of measurements on Feb. 6, 2011

Figure 4.1 Time history of the anemometer wind speed and wind turbine rotational speed between a time of 600 hours and 1800 hours for three different days

The Fast Fourier Transforms for each of these signals is shown in Fig. 4.2 to find the prominent prevailing frequency, or peak, for each analyzed day. Based on the plots, a distinct peak is not observed. To further find a relationship between the signals, system identification is implemented.

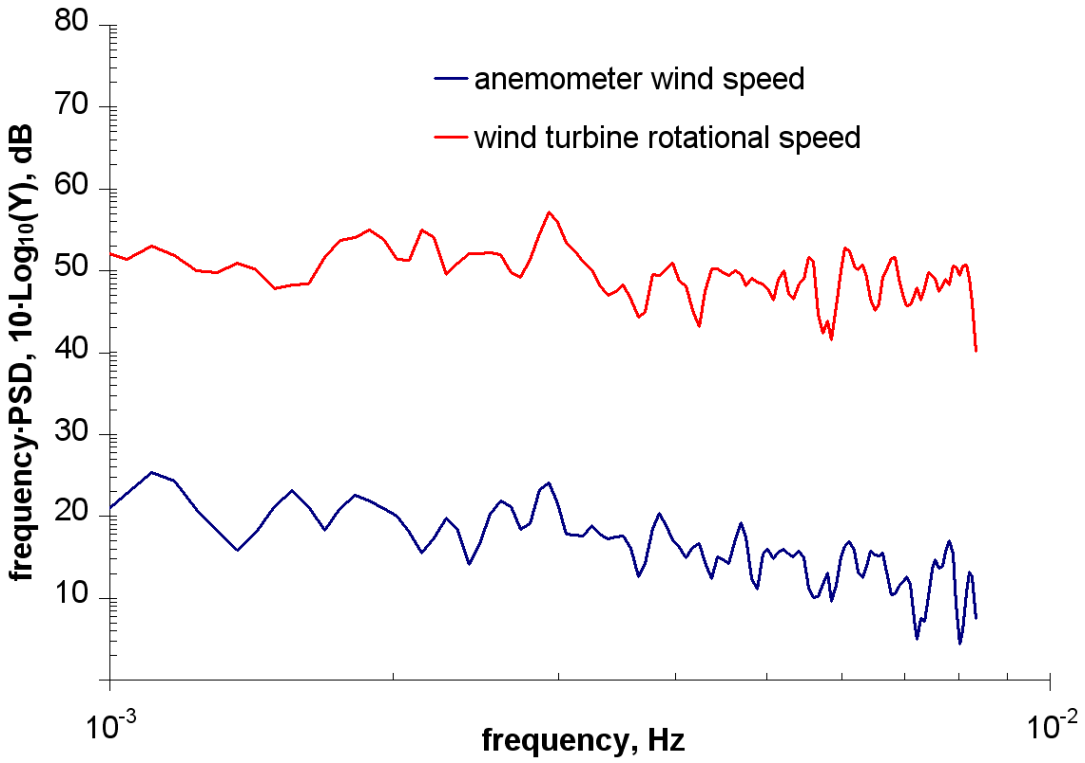

(a) Fast Fourier Transform results for Jan. 30, 2011

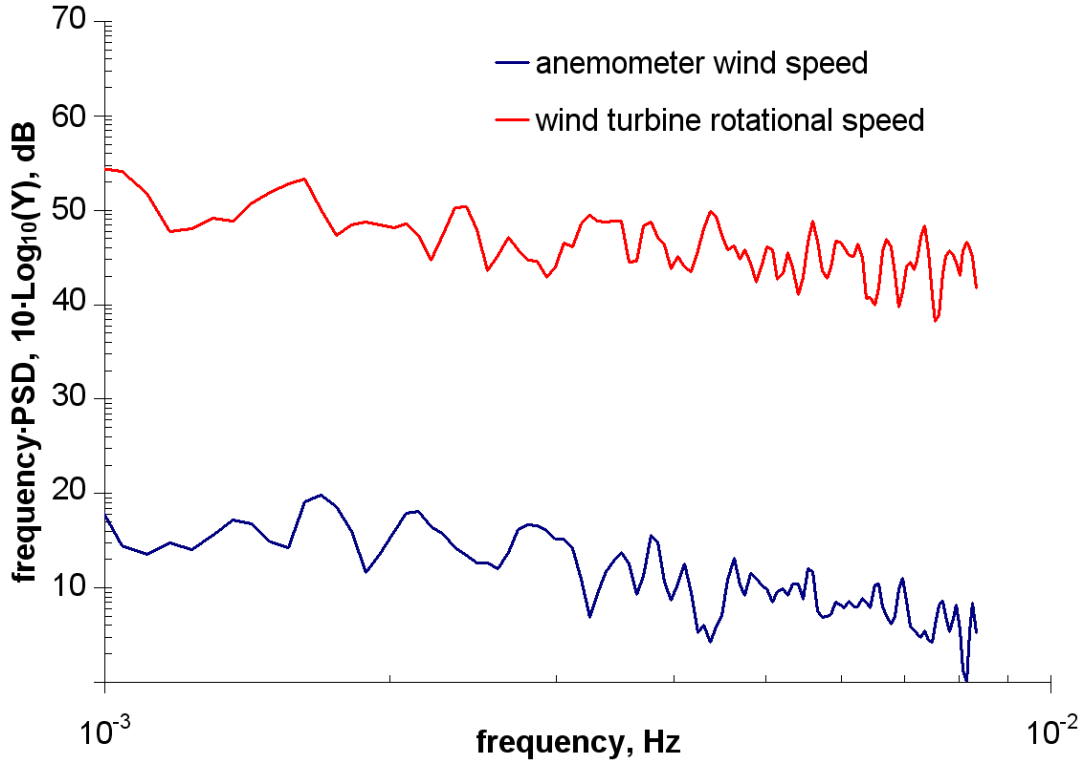

(b) Fast Fourier Transform results for Feb. 6, 2011

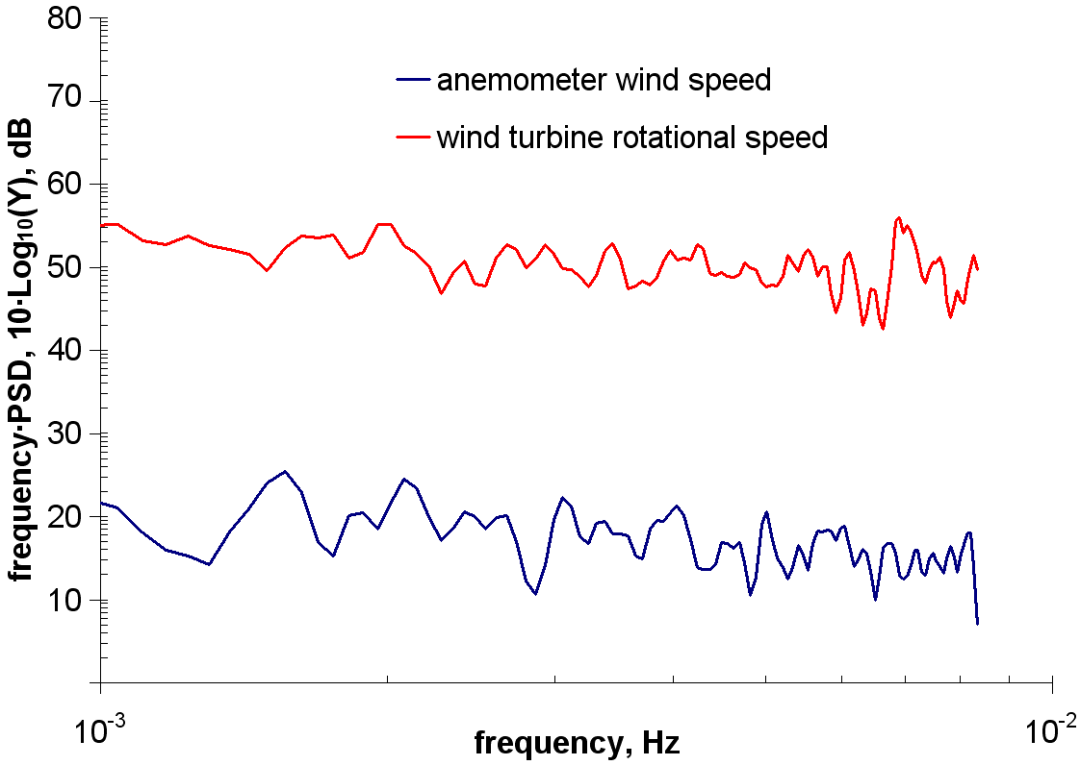

(c) Fast Fourier Transform results for Feb. 6, 2011

Figure 4.2 Fast Fourier Transform results using the anemometer wind speed and the wind turbine rotational speed for three different days

4.1.2 Model Selection

A finite number of dynamic poles, zeros, delays, and disturbance model poles are chosen by trial and error to find a model that provides a simulated output with the best fit compared to the actual output of the wind turbine (Barbounis and Theocharis, 2007). In Matlab, the function that is used is, "IDENT." The most common system identification models are discussed in the following sections.

4.1.2.1 ARX Model

The auto regression model with exogenous input variables (ARX) is implemented as a linear and dynamic model (Ljung, 1999). The model is given in Eq. (4.1) as,

$$y(t) + a_1 y(t-1) + \ldots + a_{n_a} y(t-n_a) = b_1 u(t-n_k) + b_2 u(t-n_k-1) + \ldots + b_{n_b} u(t-n_k-n_b+1) + e(t) \quad (4.1)$$

where y(t) is the output signal at time t, u(t) is the input signal, a and b are coefficients, n_a is the number of dynamic poles, n_b is the number of zeros plus 1, n_k is the input delay, or the number of time steps before the input affects the output, and e(t) is the white-noise disturbance associated with the output (Ljung, 1999). The model orders of n_a, n_b, and n_k are manually specified between a value of 1 to 10 in search of the best fit output simulated by the transfer function. This range is selected to cover the range of values concluded by Kanellos et al. (2011) to establish a comparable simulated output versus the measured output. Manually specifying the values based on trial and error (Barbounis and Theocharis, 2007) is significantly based on the individuality of the tested wind turbine model in this study. The three chosen models will be identified and implemented in the following sections, then summarized.

4.1.2.2 ARMAX Model

The ARMAX model is an extension of the ARX model with a moving average. It includes an extra polynomial to model the additive disturbance, to make it more flexible than the base ARX model (Ljung, 1999). This model is given in Eq. (4.2) as,

$$y(t) + a_1 y(t-1) + \ldots + a_{n_a} y(t-n_a) = b_1 u(t-n_k) + b_2 u(t-n_k-1) + \ldots + b_{n_b} u(t-n_k-n_b+1) + e(t) + c_1 e(t-1) + \ldots + c_{n_c} e(t-n_c) \quad (4.2)$$

where c is a coefficient and n_c is the number of poles for the disturbance model (Ljung, 1999). In this study, the values for n_a, n_b, and n_k from the ARX model will also be used for the ARMAX model. This model will include the optimal value for n_c between a range of 1 to 10 to compare to the ARX model.

4.1.2.3 OE Model

The last model used in this study is the output error (OE) model. This model is given in Eq. (4.3) as,

$$y(t) = \frac{b_1 + b_2 q^{-1} + \ldots + b_{n_b} q^{-n_b+1}}{1 + f_1 q^{-1} + \ldots + f_{n_f} q^{-n_f}} u(t-n_k) + e(t) \quad (4.3)$$

where q is a root, f is a coefficient, and n_f is the number of poles for the shown polynomial in the OE model (Ljung, 1999). With this model introduced, the next step is applying the models and

adjusting them to fit the actual wind turbine measurements. The model that displays the best fit will then be provided.

4.1.3 Model Adjustment and Results

4.1.3.1 ARX Model

The ARX model is modeled first. The number of dynamic poles, zeros, and delays are specified manually to obtain a simulated output that best fits the actual wind turbine rotational speed. The values are iterated within a range of 1 to 10 to sufficiently cover the maximum order of three of the parameters concluded by Kanellos et al. (2011). The ARX model is generated for each of the analyzed days. From iterating the values of the poles, zeros, and delays, a general model between each day is found to have one dynamic pole, one zero, and four delays. Using these values the resulting transfer functions for each day are shown in Table 4.1. In addition to the similarity in the values for the number of dynamic poles, zeros, and delays that optimize the match between the measured rotational speed and the modeled rotational speed of the wind turbine, the transfer function coefficients also are similar in value as observed in Table 4.1. Figure 4.3 shows the ARX model result for the wind turbine rotational speed for each day. To assess the accuracy of the ARX model and attempt to improve the estimation of the sharp peaks that are not captured, the ARMAX and OE models are implemented for comparison.

Table 4.1 ARX model parameters and transfer functions for three different days

Day of analysis	Dynamic poles	Zeros	Delays	Transfer function
Jan. 30, 2011	1	1	4	$\frac{2.5080}{s^4 - 0.9312s^3}$
Feb. 5, 2011	1	1	4	$\frac{8.0170}{s^4 - 0.8000s^3}$
Feb. 6, 2011	1	1	4	$\frac{8.0350}{s^4 - 0.7820s^3}$

4.1.3.2 ARMAX Model

The ARMAX model incorporates the number of poles, zeros, and delays from the ARX transfer functions, with the addition of the number of poles for the disturbance model (n_c). The value of n_c is iterated between 1 and 10 to find the best fit. The ARMAX model shows a similarity in that one additional pole for the disturbance model for each of the analyzed days does not present a significant difference versus higher values for the parameter. Even though increasing this parameter is assumed to improve the estimation of the sharp peaks, the result shows that there is not an improvement. The inconsistent level of the peaks may contribute to the difficulty in selecting a unique value of poles for the disturbance model (Ljung, 1999). With the values of the parameters decided, the transfer functions for the ARMAX model are shown in Table 4.2. Figure 4.3 shows the ARMAX model result for the wind turbine rotational speed for each day.

Table 4.2 ARMAX model parameters and transfer functions for three different days

Day of analysis	Dynamic poles	Zeros	Disturbance model poles	Delays	Transfer function
Jan. 30, 2011	1	1	1	4	$\frac{4.8540}{s^4 - 0.8608s^3}$
Feb. 5, 2011	1	1	1	4	$\frac{2.3610}{s^4 - 0.9374s^3}$
Feb. 6, 2011	1	1	1	4	$\frac{1.0160}{s^4 - 0.9722s^3}$

Even though the ARMAX model accounts for the disturbance model with an additional polynomial, the ARMAX model for each day does not show a distinct improvement compared to the ARX model. To keep the transfer function as simple as possible while maintaining a similar level of accuracy (Lopez-Cruz et al., 2011), the ARX model is preferred in this study versus the ARMAX model in correlating the anemometer wind speed to the wind turbine rotational speed.

4.1.3.3 OE Model

The values of the number of poles, zeros, and delays for the last model included in this study are iterated in a similar fashion as the ARX and ARMAX models. After iterating the values for the parameters, there is a similarity in that a suitable fit incorporates one dynamic pole

and one zero as in the ARX and ARMAX models. The difference in the OE model is that the best fit with this model includes six delays instead of four as in the other models. The resulting transfer functions for the three different days using the OE model are shown in Table 4.3. Figure 4.3 shows the OE model result for the wind turbine rotational speed for each day.

Table 4.3 OE model parameters and transfer functions for three different days

Day of analysis	Dynamic poles	Zeros	Delays	Transfer function
Jan. 30, 2011	1	1	6	$\frac{8.2410}{s^6 - 0.7772s^5}$
Feb. 5, 2011	1	1	6	$\frac{2.0680}{s^6 - 0.9511s^5}$
Feb. 6, 2011	1	1	6	$\frac{0.1101}{s^6 - 0.9961s^5}$

The OE model shows that the gain (numerator value) varies significantly from day to day to fit the transfer function in minimizing the output error. This is anticipated since the fluctuation of the rotational speed varies at a high degree from day to day. By observing the modeled rotational speed using the OE model, the OE model does not improve upon the accuracy of estimating the rotational speed enough to support the need in adding two delays to the transfer function versus the ARX model, unnecessarily complicating the transfer function (Lopez-Cruz et al., 2007). This leads to the conclusion that the ARX model is the model of choice to implement system identification in correlating the anemometer wind speed to the wind turbine rotational speed in this study.

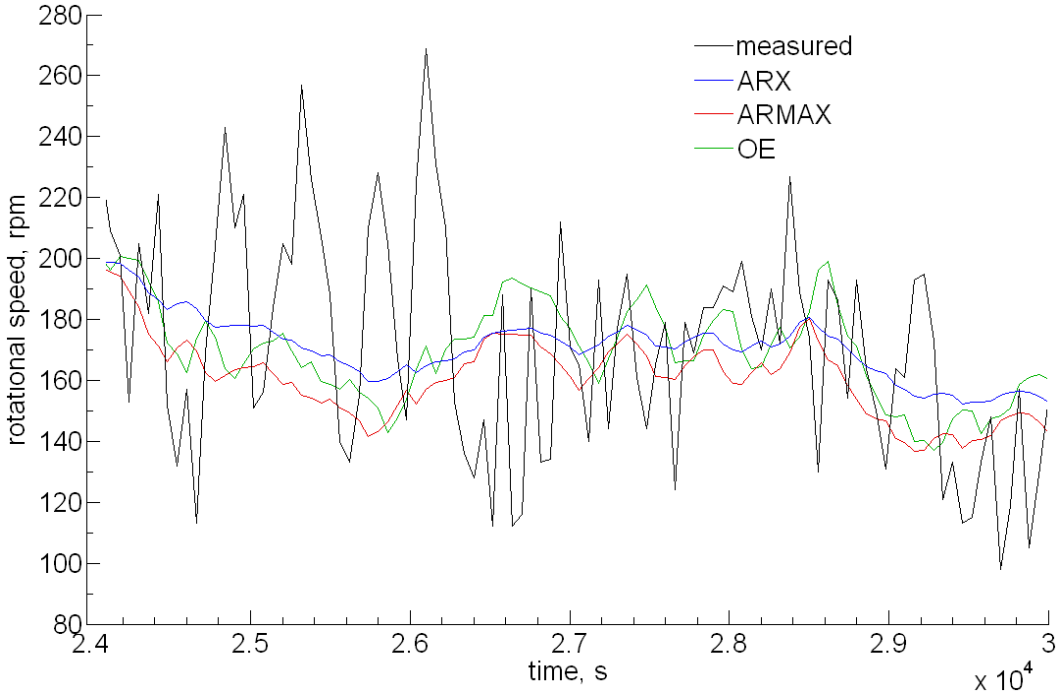

(a) Modeled and actual rotational speed for Jan. 30, 2011

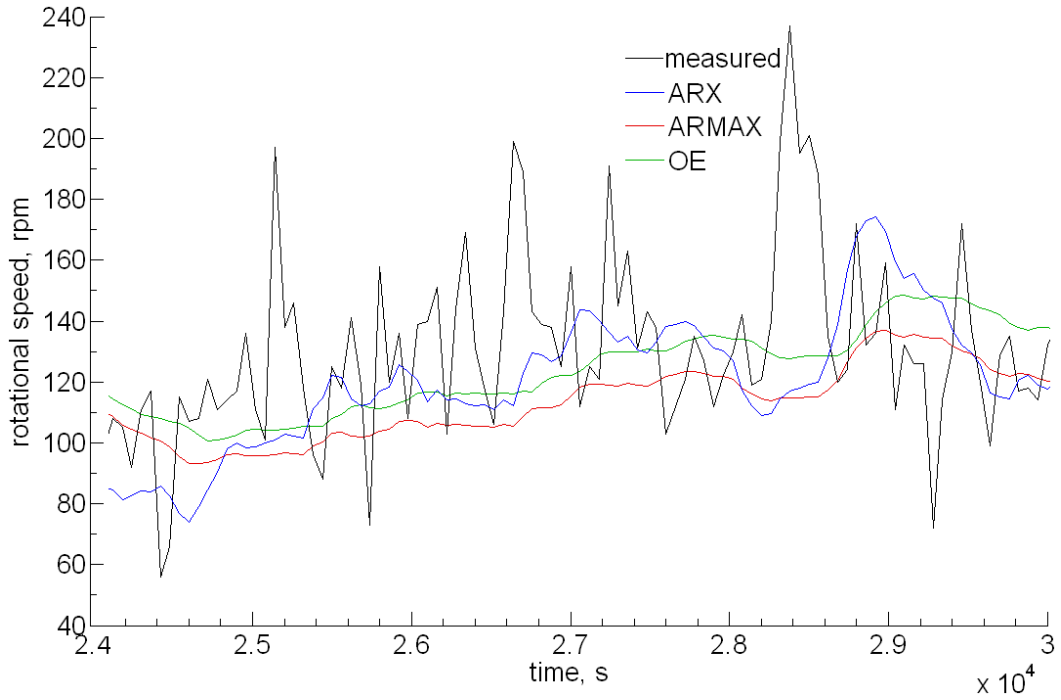

(b) Modeled and actual rotational speed for Feb. 5, 2011

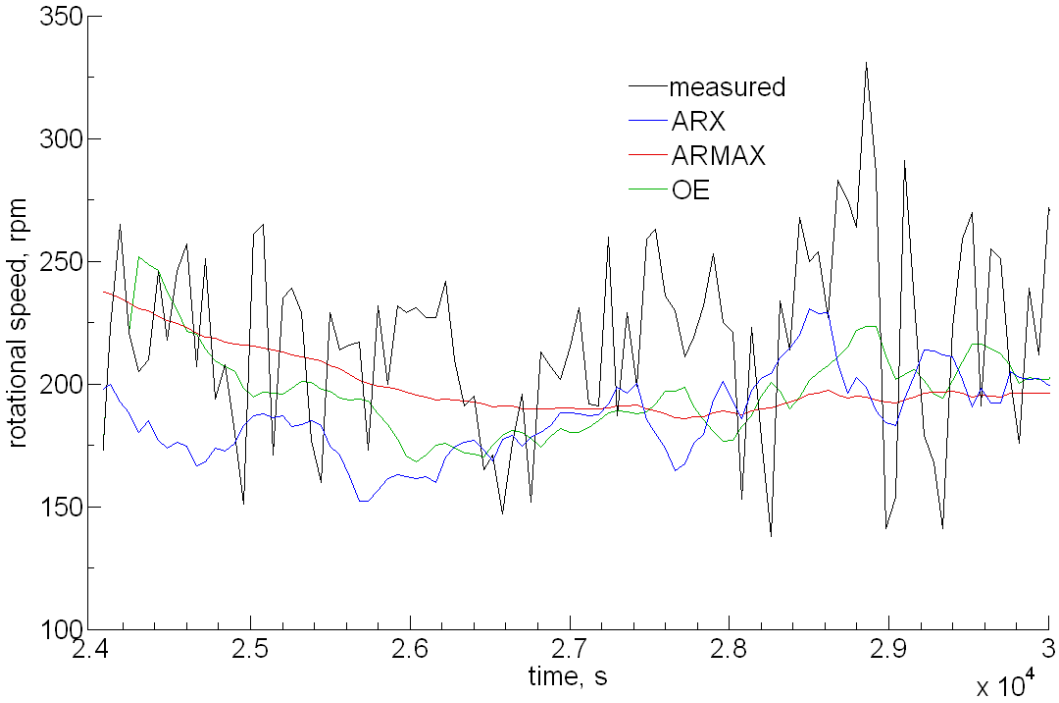

(c) Modeled and actual rotational speed for Feb. 6, 2011

Figure 4.3 Plots of the modeled and measured rotational speed using the different models for three different days

4.1.4 Results of the Power Output

The sought result is the assessment of the measured power output of the wind turbine compared to the power output that is estimated by the rotational speeds generated by the transfer function model. First, the transfer model will be generalized by averaging the coefficients of the selected model. Second, the transfer function will be used to calculate a modeled wind speed and power output. The last step is then comparing the modeled power output to the measured power output of the wind turbine.

Combining the system identification results, a general transfer function linking the input anemometer wind speed to the output wind turbine rotational speed is generated. The inspection of the plots and the comparison of the degree of accuracy from the model outputs shows that the ARX model is the optimal selection. To generalize the transfer function of the ARX model, the coefficients from each day of analysis are averaged. The resulting transfer function is given in Eq. (4.4) as,

$$H(s) = \frac{6.1867}{s^4 - 0.8377s^3} \tag{4.4}$$

where s is the pole in a discrete time domain. The transfer function is represented in the discrete time domain by applying the inverse Laplace transform ("ILAPLACE(F)" in Matlab), giving Eq. (4.5) as,

$$F(t) = -3.6927t^2 - 8.8162t + 21.0486e^{0.4189t}\sinh(0.4189t) \tag{4.5}$$

Using Eq. (4.5), the modeled rotational speed of the wind turbine can be used to calculate its wind speed. The wind speed of the wind turbine in $m \cdot s^{-1}$ is given in Eq. (4.6) as,

$$V_{turb} = \frac{rpm \cdot D_{turb}}{60 \cdot tip\ speed\ ratio} \tag{4.6}$$

where the diameter of the wind turbine is 3.7 m, the tip speed ratio is 2.16, and the power efficiency is 65.2%. The tip speed ratio and power efficiency are both calculated using the measurements from the wind turbine. The tip speed ratio is calculated using the wind turbine measurements for rotational speed and wind speed, and using Eq. (4.6). As a note, the tip speed ratio calculation may depend on the general wind speed of the days that are under analysis. The days under analysis in this study have wind speeds between 5 $m \cdot s^{-1}$ to 7 $m \cdot s^{-1}$ at an elevation of 18.3 m. The power efficiency is calculated using the power output measured by the wind turbine and comparing it to the "ideal" power output that is calculated using the measured wind speed of the wind turbine and Eq. (4.7). The modeled wind speed of the wind turbine is then used to calculate the modeled wind turbine power output using Eq. (4.7),

$$P = \frac{1}{2}\rho A_{turb} V_{turb}^{\ 3} \tag{4.7}$$

where the air density ρ=1.225 $kg \cdot m^{-3}$ and wind turbine area A_{turb}=10.7521 m^2. The modeled power output is then compared to the measured power output of the wind turbine. Figure 4.4 shows the power output comparison for each analyzed day.

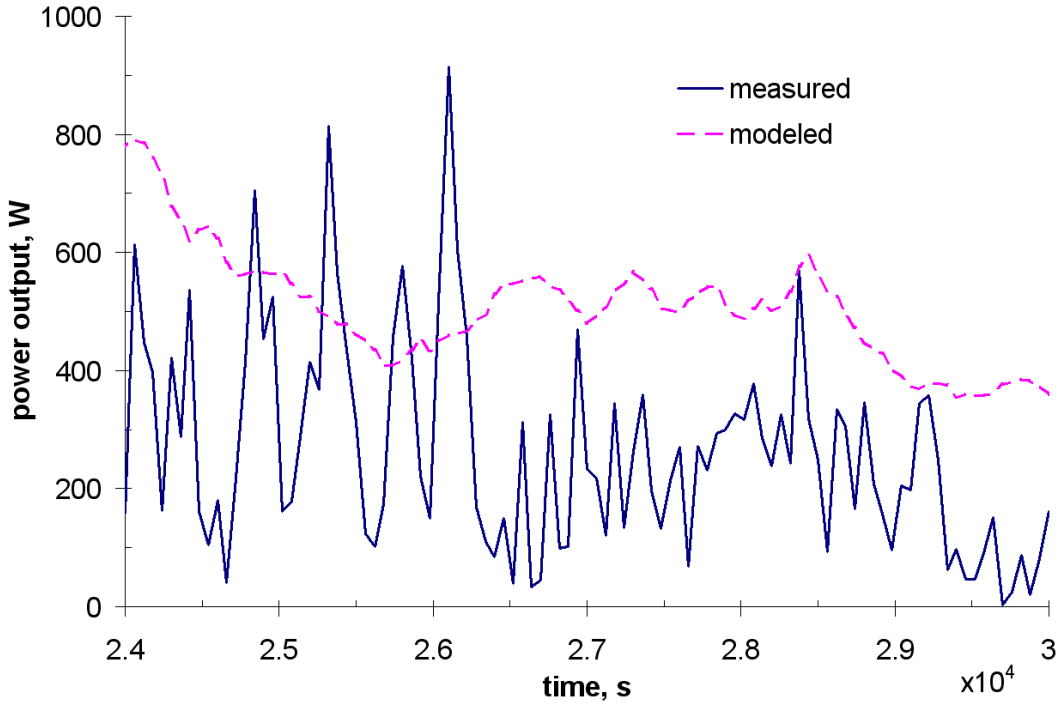

(a) Power output comparison for Jan. 30, 2011

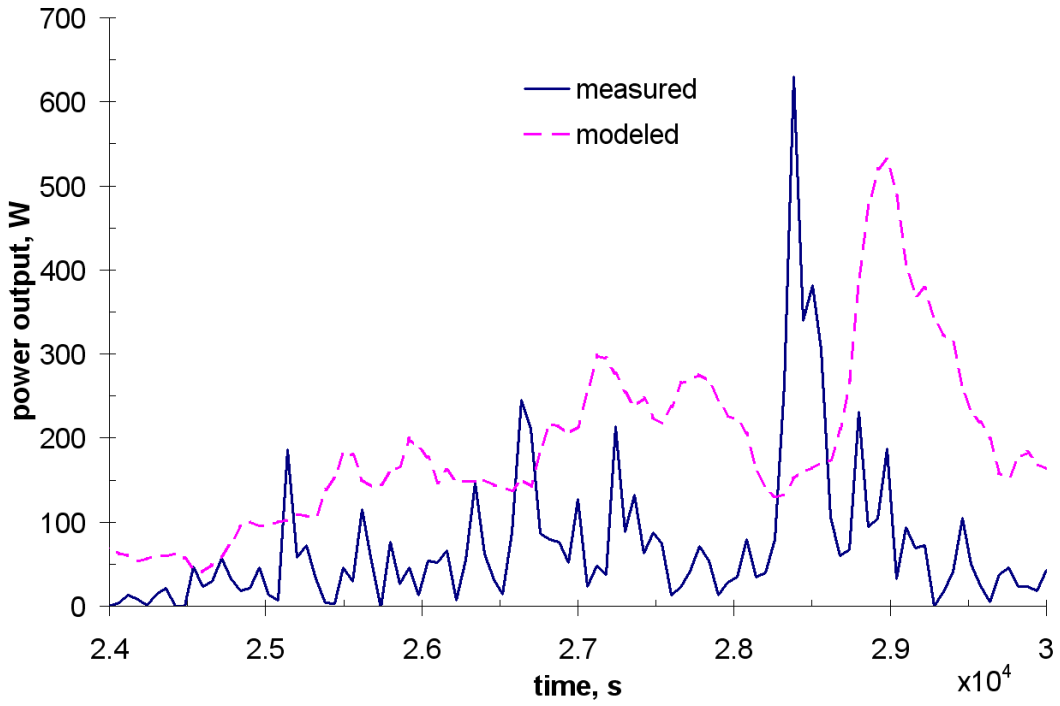

(b) Power output comparison for Feb. 6, 2011

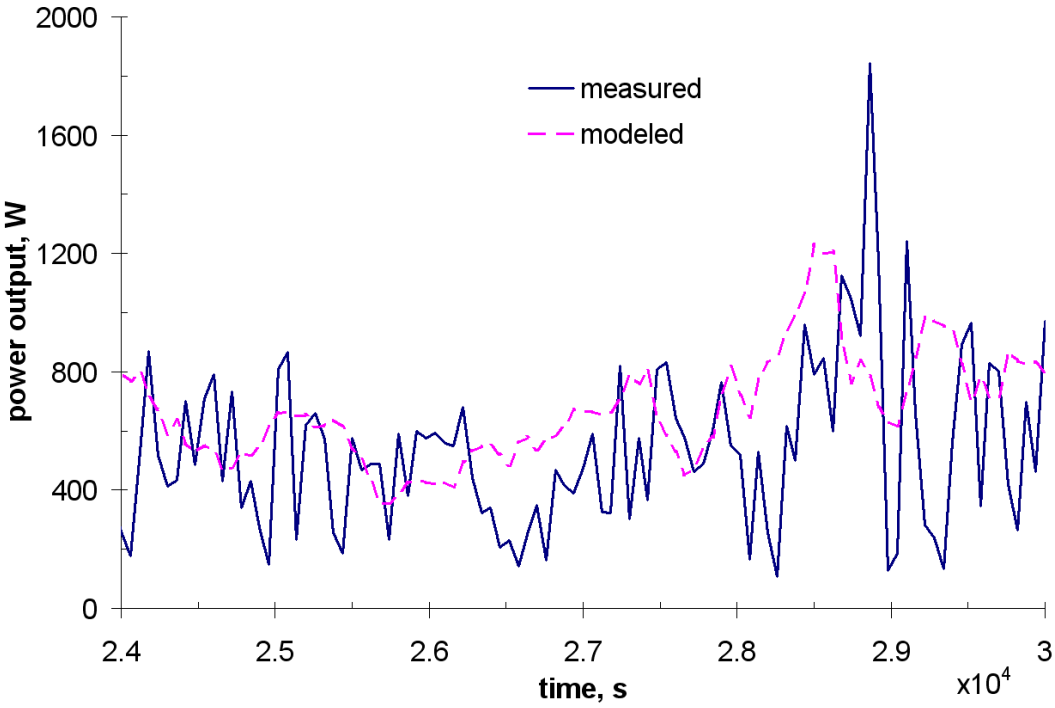

(c) Power output comparison for Feb. 6, 2011

Figure 4.4 Modeled and measured power output comparison for different days

When the power outputs are compared, it is seen that the transfer function model reasonably estimates the power output that is actually obtained by the wind turbine. The range of match is similar to previous work in using the ARX model to predict an estimated model by staying within the 95% confidence interval for the residual calculations (Erdogan and Gulal, 2009). The confidence interval is automatically applied in the calculation of the residuals during the selection of the ARX model parameters. To summarize the results, the percentage accuracy, modeled, and measured power output averages are given in Table 4.4. The percentage accuracies are based on the calculation of the root mean squared error of the data points between the measured and modeled power outputs (Ljung, 1999).

Table 4.4 Percentage accuracy, modeled, and measured power output averages for different days

	Jan. 30, 2011	Feb. 5, 2011	Feb. 6, 2011
Percentage accuracy, % curve fit	56.0	42.2	83.3
Modeled power output average, W	511	179	712
Measured power output average, W	282	69	572

The results in Table 4.4 show that the transfer function slightly overestimates the power output average for each day. The percentage accuracies are also inconsistent using a simple ARX model. This can be improved by increasing the complexity of the transfer function, and using a larger range of days to estimate the general transfer function structure (Lopez-Cruz et al., 2007). It may be necessary to adjust the transfer function if there are any changes to the system, such as the daily changes in the weather, and mechanical degradation of the wind turbine (Uchida-Frausto et al., 2003). However, for the purpose of generating a reasonable and simple transfer function structure, the results from the chosen ARX model will be further supported and discussed.

To put the results in perspective, the values listed in Table 4.4 are compared to a traditional method in estimating the power output of a wind turbine using a high-elevation wind map. The average annual wind speed in Manhattan, KS, is 5.4 $m \cdot s^{-1}$ (Schuster, 2009) at an elevation of 18.3 m using the Counihan (1975) exponent. For the wind turbine used in this study, the power output projected from the power curve is 300 W (Calley and Kruse, 2011). The results summarized in Table 4.4 show that using a high-elevation wind map estimation clearly does not suit each day, showing a significant inaccuracy in estimating the power output for Feb. 6, 2011. By comparing only three different days, it is observed that the use of the transfer function generated by the ARX model vastly improves the estimation of the power output, with just the wind speeds measured by an anemometer. Depending on the application related to the wind turbine, this improvement in predicting the power output on a day-to-day basis may be vital. The

results presented in this study improve the traditional method in estimating energy output from a high-elevation wind map, validating an accurate means of correlating wind speeds measured by an anemometer to the power output of a wind turbine.

4.2 Summary

By implementing system identification, the power production of a wind turbine can be estimated better than using a high-elevation wind map. The cost savings in using a single anemometer to estimate the power production of a wind turbine is a promising aspect in adopting system identification. Estimations based on high-elevation wind maps can be inaccurate in predicting day-to-day power outputs. Even a low-order ARX model can accurately estimate the power output of a wind turbine with percentage accuracies of 83%, and higher-order models can be investigated based on the needs of the user. Day-to-day predictions are also achievable using system identification, another factor that wind map estimations lack. Auto regression models are quick and can be simple based on the structure of the selected transfer function. The results presented in this study considerably improve the traditional method in estimating energy output from a high-elevation wind map and validate a means of correlating anemometer wind speeds to the power output of a wind turbine.

Chapter 5 - Conclusions and Future Work

In the fifth chapter, I will conclude the research objectives. The goals are reiterated and the results are recapped.

The three goals in this research have been addressed through numerical simulation and by the analysis of the measurements from the wind turbine and the anemometers. First, changes in building heights and in the wind resistance in trees show that there are trends in the Strouhal number, where the value generally increases at a location downwind with an increase in building height as well as an increase in the inertial resistance of a tree. Given the general contour of an urban environment, an optimal location in siting a wind turbine can be found if it were necessary to install a wind turbine within the area.

Second, with the parameters for a simple layout of a building and tree recognized, a simulation of a Manhattan, KS, wind turbine site showed accurate results between the wind speeds generated by the model and measured by the wind turbine and anemometers. Simulating an environment in this way provides much better estimates of the power production from a wind turbine based on the terrain, rather than relying on an estimation based on a high-elevation wind map. For example, a wind map shows that Manhattan, KS, has an annual average wind speed of 5.4 $m \cdot s^{-1}$ at an elevation of 18.3 m. For the wind turbine from this study, this correlates to 300 W of power production. Although this study shows that the wind map estimate matches well for the Jan. 30, 2011, case, the wind map estimate does not match with a day that is only a week later. This is shown in the Feb. 6, 2011, case, where the measured and simulated power outputs are 500 W and 570 W, respectively, but the wind map estimate is still 300 W. Using CFD, the day-to-day differences in the wind speed are achievable. Some items to keep in mind when simulating the winds at a site are:

• If a power-law profile for the incoming wind speed and turbulence intensity is used, check that the terrain properties are incorporated.

• Use a grid resolution where the cell size is at least 5% or smaller than the diameter of a tree canopy.

• Use a user-defined function for the top boundary where the velocity in the direction of the wind is established, and the lateral and vertical gradients are set to zero.

• Use appropriate wind resistance characteristics for the trees.

With these items incorporated into a numerical model, excessive costs and uncertainty in predicting power production can be avoided with the aid of CFD.

The third goal is addressed with the identification of a transfer function relating anemometer wind speeds to the power output of a wind turbine. By implementing system identification, there can be a significant cost savings in using a single anemometer to estimate the power production of a wind turbine. Estimations based on high-elevation wind maps can be as inaccurate by as much as 88%. However, even a low-order ARX model can accurately estimate the power output of a wind turbine, with percentage accuracies of 83%, and higher-order models can be investigated based on the needs of the user. Day-to-day predictions are also achievable using system identification, another factor that wind map estimations do not have. The results presented in this study considerably improve the traditional method in estimating energy output from a high-elevation wind map and validate a means of correlating anemometer wind speeds to the power output of a wind turbine.

With all three goals addressed, the feasibility of small-scale wind turbines in different low-elevation environments is assessed. Numerical simulation and system identification are strong tools that can improve upon the traditional methods in estimating power production for a wind turbine. In accomplishing these tasks, the performance of a small-scale wind turbine can be significantly optimized.

References

Archer, C. L., and Jacobson, M. Z.. "Spatial and Temporal Distributions of U.S. Winds and Wind Power at 80 m Derived from Measurements," Journal of Geophysical Research-Atmospheres, Vol. 108(D9), No. 1-20, 2003.

Barbounis, T. G., and Theocharis, J. B., "Locally Recurrent Neural Networks for Wind Speed Prediction using Spatial Correlation," Information Sciences, Vol. 177, No. 24, Dec. 2007, pp. 5775-5797.

Baric, E., Dzijan, I., and Kozmar, H., "Numerical Simulation of Wind Characteristics in the Wake of a Rectangular Building Submitted to Realistic Boundary Layer Conditions," Transactions of FAMENA, Vol. 34, No. 3, 2010, pp. 1-10.

Bashor, R., and Kareem, A., "Comparative Study of Major International Standards," The Seventh Asia-Pacific Conference on Wind Engineering, Nov. 8-12, 2009, Taipei, Taiwan.

Calley, D., and Kruse, A., "Product Spec Sheet (pdf)." Skystream Info. 2011. Southwest Windpower. 18 Mar. 2011. <http://www.skystreamenergy.com/index-main.php>

Cebeci, T., and Bradshaw, P., "Momentum Transfer in Boundary Layers," Hemisphere Publishing Corp., Washington, D. C., 1977.

Chan, T. L., Dong, G., Leung, C. C., Cheung, C. S., and Hung, W., "Validation of a Two-Dimensional Pollutant Dispersion Model in an Isolated Street Canyon," Atmospheric Environment, Vol. 36, No. 5, 2002, pp. 861-872.

Counihan, J., "Atmospheric Adiabatic Boundary Layers-Review and Analysis of Data from Period 1880-1972," Atmospheric Environment, Vol. 9, No. 2, 1975, pp. 871-905.

Da Silva, A., Sinfort, C., Tinet, C., Pierrat, D., and Huberson, S., "A Lagrangian Model for Spray Behaviour Within Vine Canopies," Aerosol Science, Vol. 37, No. 5, 2006, pp. 658-674.

Elizondo, J., Martinez, J., and Probst, O., "Experimental Study of a Small Wind Turbine for Low- and Medium-Wind Regimes," International Journal of Energy Research, Vol. 33, No. 3, 2009, pp. 309-326.

Elmore, A., and Gallagher, R., "Using Regional Climate Center Data to Predict Small Wind Turbine Performance," Practice Periodical of Hazardous, Toxic, and Radioactive Waste Management, Vol. 13, No. 1, Jan. 2009, pp. 14-19.

Endalew, A., Hertog, M., Delele, M., Baetens, K., Persoons, T., Baelmans, M., Ramon, H., Nicolai, B., and Verboven, P., "CFD Modelling and Wind Tunnel Validation of Airflow through Plant Canopies using 3D Canopy Architecture," International Journal of Heat and Fluid Flow, Vol. 30, No. 2, Apr. 2009, pp. 356-368.

Erdogan, H., and Gulal, E., "Identification of Dynamic Systems using Multiple Input-Single Output (MISO) Models," Nonlinear Analysis-Real World Applications, Vol. 10, No. 2, 2009, pp. 1183-1196.

Fluent Inc. 6.3 User's Guide, 2006.

Google Earth, Manhattan, KS, 2011.

Grant, P. F., and Nickling, W. G., "Direct Field Measurement of Wind Drag on Vegetation for Application to Windbreak Design and Modelling," Land Degredation and Development, Vol. 9, No. 1, 1998, pp. 57-66.

Gromke, C., and Ruck, B., "Aerodynamic Modelling of Trees for Wind Tunnel Studies," Forestry, Vol. 81, No. 3, 2008, pp. 243-258.
Hailes, D. "Executive Summary." Briefings and reports. 2009. Encraft. 2 Mar. 2011. <http://www.warwickwindtrials.org.uk/2.html>
Hargreaves, D., and Wright, N., "On the use of the k-epsilon Model in Commercial CFD Software to Model the Neutral Atmospheric Boundary Layer," Journal of Wind Engineering and Industrial Aerodynamics, Vol. 95, No. 5, 2007, pp. 355-369.
Heath, M. A., Watson, S. J., and Walshe, J. D., "Estimating the Potential Yield of Small Building-Mounted Wind Turbines," Wind Energy, Vol. 10, No. 3, 2007, pp. 271-281.
Huang, R. F., Lin, B. H., and Yen, S. C., "Time-Averaged Topological Flow Patterns and their Influence on Vortex Shedding of a Square Cylinder in Crossflow at Incidence," Journal of Fluids and Structures, Vol. 26, No. 3, Apr. 2010, pp. 406-429.
Kanellos, F. D., Tsekouras, G. J., and Hatziargyriou, N. D., "Wind Parks Equivalent ARX Models for the Simulation of Power Systems with Large Wind Power Penetration, using System-Identification Theory," Electric Power Systems Research, Vol. 81, No. 2, 2011, pp. 707-715.
Katul, G. G., Mahrt, L., Poggi, D., and Sanz, C., "One- and Two-Equation Models for Canopy Turbulence," Boundary Layer Meteorology, Vol. 113, No. 1, 2004, pp. 81-109.
Kaufman, J. W., "Terrestrial Environment (Climatic) Criteria Guidelines for Use in Aerospace Vehicle Department," NASA TM X-78118, NASA Marshall Space Flight Center, Huntsville, Alabama, 1977.
Kim, S. E., and Choudhury, D., "A Near-Wall Treatment Using Wall Functions Sensitized to Pressure Gradient," ASME Fluids Engineering Division (FED), Separated and Complex Flows, Vol. 217, No. 1, 1995, pp. 273-279.
Kozmar, H., "Influence of Spacing between Buildings on Wind Characteristics above Rural and Suburban Areas," Wind and Structures, Vol. 11, No. 5, 2008, pp. 413-426.
Kozmar, H., "Wind-Tunnel Simulations of the Suburban ABL and Comparison with International Standards," Wind and Structures, Vol. 14, No. 1, 2011, pp. 15-34.
Laadhari, F., Skandaji, L., and Morel, R., "Turbulence Reduction in a Boundary Layer by a Local Spanwise Oscillating Surface," Physics of Fluids, Vol. 6, No. 10, 1994, pp. 3218-3220.
Launder, B. E., and Spaulding, D. B., "Lectures in Mathematical Models of Turbulence," Academic Press, London, 1972.
Ljung, L., "System Identification: Theory for the User, 2nd Edition," Prentice Hall, New Jersey, USA, 1999, pp. 609.
Lopez-Cruz, I. L., Rojano-Aguilar, A., Ojeda-Bustamante, W., and Salazar-Moreno, R., "ARX Models for Predicting Greenhouse Air Temperature: A Methodology," Agrociencia, Vol. 41, No. 2, Feb.-Mar. 2007, pp. 181-192.
Manwell, J. F., McGowan, J. G., and Rogers, A. L., Wind Energy Explained, John Wiley & Sons Ltd., West Sussex, England, 2002, pp. 44-45.
Nordmeyer, K. "Wind Energy Manual, Wind and Wind Power." Renewable Energy, Wind. 2006. Iowa Energy Center. 2 Mar. 2011. <http://www.energy.iastate.edu/Renewable/wind/wem/windpower.htm>
Patankar, S. V., "Numerical Heat Transfer and Fluid Flow," Hemisphere Publishing Corp., Washington, D. C., 1980.
Pope, S. B., "Turbulent Flows," Cambridge University Press, New York, 2000.

Rakai, A., and Kristof, G., "CFD Simulation of Flow over a Mock Urban Setting," 5th OpenFOAM Workshop, Chalmers, Gothenburg, Sweden, Jun. 21-24, 2010.
Sakamoto, H., and Arie, M., "Vortex Shedding from a Rectangular Prism and a Circular Cylinder Placed Vertically in a Turbulent Boundary Layer," Journal of Fluid Mechanics, Vol. 126, 1983, pp. 147-165.
Santiago, J. L., and Martin, F., "Modelling the Air Flow in Symmetric and Asymmetric Street Canyons," International Journal of Environment and Pollution, Vol. 25, No. 1-4, 2005, pp. 145-154.
Sanz, C., "A Note on k-ε Modelling of Vegetation Canopy Air-Flows," Boundary Layer Meteorology, Vol. 108, No. 1, 2003, pp. 191-197.
Sarioglu, M., and Yavuz, T., "Subcritical Flow Around Bluff Bodies," AIAA Journal, Vol. 40, No. 7, 2002, pp. 1257-1268.
Schlichting, H., "Boundary Layer Theory, 8th Edition," McGraw-Hill, New York, 2000.
Schuster, H. J. "KCC Maps." Kansas Wind Maps. 15 May 2009. Kansas Corporation Commission. 25 Oct. 2010. <http://www.kcc.state.ks.us/maps/Kansas_SPD50m_22Sept08.pdf>
Sheinman, Y., and Rosen, A., "A Dynamic Model of the Influence of Turbulence on the Power Output of a Wind Turbine," Journal of Wind Engineering and Industrial Aerodynamics, Vol. 39, No. 1-3, 1992, pp. 329-341.
Spera, D. A., and Richards, T. R., "Modified Power Law Equations for Vertical Wind Profiles," NASA TM-79275, DOE/NASA/1059-79/4, NASA Lewis Research Center, Cleveland, Ohio, 1979.
Spera, D. A. "Wind Turbine Technology: Fundamental Concepts of Wind Turbine Engineering," Second Ed., ASME Press, New York, NY, 2009.
Stull, R. B., "An Introduction to Boundary Layer Meteorology," Klumer Academic, Dordrecht, Netherlands, 1988.
Tamura, Y., Iwatani, Y., Hibi, K., Suda, K., Nakamura, O., Maruyama, T., and Ishibashi, R., "Profiles of Mean Wind Speeds and Vertical Turbulence Intensities Measured at Seashore and Two Inland Sites using Doppler Sodars," Journal of Wind Engineering and Industrial Aerodynamics, Vol. 95, No. 6, 2007, pp. 411-427.
Tieleman, H. W., "Wind Tunnel Simulation of Wind Loading on Low-Rise Structures: a Review," Journal of Wind Engineering and Industrial Aerodynamics, Vol. 91, No. 12-15, 2003, pp. 1627-1649.
Tieleman, H. W., "Strong Wind Observations in the Atmospheric Surface Layer," Journal of Wind Engineering and Industrial Aerodynamics, Vol. 96, No. 1, 2008, pp. 41-77.
Uchida-Frausto, H., Pieters, J. G., and Deltour, J. M., "Modeling Greenhouse Temperature by means of Auto Regressive Models," Biosystems Engineering, Vol. 84, No. 2, 2003, pp. 147-157.
Versteeg, H. K., and Malalasekera, W., "An Introduction to Computational Fluid Dynamics. The Finite Volume Method," Longman Group Ltd., New York, 1995.
Wu, R. M., Lin, M. H., Lin, H. Y., and Hsu, R. Y., "3D Simulations of Hydrodynamic Drag Forces on Two Porous Spheres Moving Along Their Centerline," Journal of Colloid and Interface Science, Vol. 301, No. 1, 2006, pp. 227-235.
Xu, Y., "Flow/Acoustic Interactions in Porous Media under a Turbulent Wind Environment," Ph.D. dissertation, Department of Mechanical and Nuclear Engineering, Kansas State

University, Appendix A Spectral Analysis using a Hamming Window, 2010, pp. 184-189.
Yakhot, V., and Orszag, S. A., "Renormalization-Group Analysis of Turbulence," Physical Review Letters, Vol. 57, No. 14, 1986, pp. 1722-1724.
Yoon, D. H., Yang, K. S., and Choi, C. B., "Flow past a Square Cylinder with an Angle of Incidence," Physics of Fluids, Vol. 22, No. 4, Apr. 2010.
Zhang, X., "CFD Simulation of Neutral ABL Flows," Riso-R-1688(EN), Riso National Laboratory for Sustainable Energy, Technical University of Denmark, Roskilde, Denmark, Apr. 2009.
Zhou, Y., and Kareem, A., "Definition of Wind Profiles in ASCE 7," Journal of Structural Engineering, Vol. 128, No. 8, Aug. 2002, pp. 1082-1086.